FEDERAL UNIVERSITY OF CEARÁ

CENTER OF SCIENCE

DEPARTMENT OF PHYSICS

POST-GRADUATION PROGRAM IN PHYSICS

DOCTORAL DEGREE IN PHYSICS

FRANCISCO ETAN BATISTA DE SOUSA

ELECTRONIC, TRANSPORT AND OPTICAL PROPERTIES IN MULTILAYER PHOSPHORENE

FORTALEZA

2023

FRANCISCO ETAN BATISTA DE SOUSA

ELECTRONIC, TRANSPORT AND OPTICAL PROPERTIES IN MULTILAYER PHOSPHORENE

Thesis submitted to the Post-Graduation Program in Physics of the Center of Science of the Federal University of Ceará, as a partial requirement for obtaining the title of Doctor in Physics. Concentration Area: Physics

Advisor: Prof. Dr. Jeanlex Soares de Sousa

Co-advisor: Prof. Dr. Diego Rabelo da Costa

FORTALEZA

2023

Dados Internacionais de Catalogação na Publicação
Universidade Federal do Ceará
Sistema de Bibliotecas
Gerada automaticamente pelo módulo Catalog, mediante os dados fornecidos pelo(a) autor(a)

S696e Sousa, Francisco Etan Batista.
Electronic, transport and optical properties in multilayer phosphorene / Francisco Etan Batista Sousa. – 2023.
146 f. : il. color.

Tese (doutorado) – Universidade Federal do Ceará, Centro de Ciências, Programa de Pós-Graduação em Física , Fortaleza, 2023.
Orientação: Prof. Dr. Jeanlex Soares de Sousa.
Coorientação: Prof. Dr. Diego Rabelo da Costa.

1. Phosphorene. 2. vacancy defect. 3. band unfolding. 4. anisotropic transport. 5. dielectric function. I. Título.

CDD 530

FRANCISCO ETAN BATISTA DE SOUSA

ELECTRONIC, TRANSPORT AND OPTICAL PROPERTIES IN MULTILAYER PHOSPHORENE

Thesis submitted to the Post-Graduation Program in Physics of the Center of Science of the Federal University of Ceará, as a partial requirement for obtaining the title of Doctor in Physics. Concentration Area: Physics

Approved on: 14/07/2023

EXAMINATION BOARD

Prof. Dr. Jeanlex Soares de Sousa (Advisor)
Federal University of Ceará (UFC)

Prof. Dr. Diego Rabelo da Costa (Co-advisor)
Federal University of Ceará (UFC)

Prof. Dr. João Milton Pereira Junior
Federal University of Ceará (UFC)

Prof. Dr. Teldo Anderson da Silva Pereira
Federal University of Mato Grosso (UFMT)

Prof. Dr. Francisco Ronan Viana Araújo
Federal Institute of Piauí (IFPI)

Aos meus filhos, Miguel e Chloe. À minha amada esposa, Luciana. À minha querida mãe, Jurandir. Ao meu pai, José. Às minhas queridas irmãs e suas famílias.

ACKNOWLEDGEMENTS

Vivemos várias vidas dentro de uma vida só. Os ciclos se abrem e se fecham com o passar do tempo e cada encerramento é uma porta de entrada para um novo que se inicia. Está se fechando um dos mais importantes ciclos na minha vida ao mesmo tempo que se inicia uma nova etapa de desafios e espectativas. Durante o doutorado, vivi várias fases, algumas difíceis, e tenho muito a agradecer por ter chegado até aqui.

Agradeço aos professores Jeanlex e Diego Rabelo pela orientação, ensinamentos, paciência e liberdade durante os últimos anos. Agradeço ao amigo e colega de turma professor Ronan, pelos incentivos e parcerias, além de muitas boas conversas e trocas de conhecimento. Agradeço a todos os professores do departamento de física da Universidade Federal do Ceará que contribuíram enormemente para meu desenvolvimento desde a graduação. Entre estes, devo destacar os professores Antônio Gomes, Andrey Chaves, Murilo Pereira, André Auto, Eduardo Bedê, Roberto Maluf, José Alves e Paschoal. Agradeço aos professores Milton e Teldo Anderson por aceitarem o convite para participar da banca desta Tese e por seus incentivos e sugestões. Ao professor Gil de Aquino que, junto com o professor Jeanlex, me proporcionou uma bolsa de IC no início da graduação que fez toda a diferença em meu desenvolvimento acadêmico e por todo o seu esforço em prol do crescimento do GTMC (Grupo de Teoria da Matéria Condensada).

Agradeço aos amigos do GTMC: Luan, Johnatan, Duarte, Ravena, Ícaro, Levi, Victor, Lucas, Gabriel e Maurisan pelo acolhimento e bons momentos que passamos juntos. Um agradecimento especial ao Duarte, que me ajudou em um momento difícil durante a transição do mestrado para o doutorado. Aos amigos da turma do mestrado, Ronan, Thiago, Johnatan, Leylane, Gilvan e Nelcione pela troca de conhecimento e pelas agradáveis conversas. Aos meus amigos da graduação pelos bons momentos juntos.

Um agradecimento especial a minha esposa pela paciência e por todo apoio dado em todo este ciclo. A minha mãe e minhas irmãs Irandi, Erandi e Andrea, que me deram condição de me tornar uma pessoa capaz de lutar pelos meus objetivos e chegar até aqui.

Agradeço ao CNPq (Conselho Nacional de Desenvolvimento Científico e Tecnológico) pelo apoio financeiro. Por fim, a todas as pessoas que contribuíram de alguma forma neste ciclo, direta ou indiretamente, encerrando-o ou me preparando para o próximo, deixo aqui os meus sinceros agradecimentos.

“The highest education is that which does not merely give us information but makes our life in harmony with all existence.”

(Rabindranath Tagore)

ABSTRACT

We theoretically investigate multilayer phosphorene's electronic, transport, and optical properties by numeric and semianalytical methods. First, by combining the tight-binding model and the band unfolding technique, we explore the effects of atomic vacancies on the band structure of multilayer phosphorene. Results for mono-, di-, and tri-vacancies are analyzed by keeping or not the sublattice and/or the sublayer symmetries. A detailed description of the used theoretical framework is illustrated for defect-free structures of a monolayer, bilayer, and trilayer phosphorene with Bernal stacking, which allows us to identify that the stability of the effective unfolded band is dependent on the size of the N-layer phosphorene supercell, revealing as an appropriated supercell with a size of 6×6 unit cells. In the presence of vacancies, one emerges in the band structure an almost n-fold degenerate quasi-flat state in a system with n vacancies when the sublattice symmetry or/and the inversion symmetry are broken. Within this combined approach, we also investigate the defect effects due to randomly distributed vacancies in phosphorene nanoribbons with zigzag and armchair edges. Second, we theoretically investigate the effect of a perpendicularly applied electric field and the influence of edge types (armchair and zigzag) on the conductance and collimation of charge carriers dynamics in monolayer-bilayer, monolayer-bilayer-monolayer, and bilayer-monolayer-bilayer phosphorene junctions. By using the Landauer-Büttiker formalism and the tight-binding model, we explore the probability current density and the conductance in relation to the system parameters, such as Fermi energy, electric field magnitude, and domain wall length. Our results show (i) that such physical properties exhibit a strong dependence on the crystallographic orientation of the electronic propagating mode and the interface type due to the high anisotropy on the N-layer phosphorene energy bands, effective masses, and group velocities along the x and y directions, (ii) current modulations and (iii) a pronounced dependence on the collimation of the electron beams at the interface in the investigated multilayer phosphorene junctions, obtained by applying an electric field that breaks the inversion symmetry and causes a bandgap tuning, opening (closing) the gap for monolayer (bilayer) phosphorene. All results are explained in the context of the band structure mismatch/alignment between the portions of the multilayer phosphorene junction. Finally, optic transitions in multilayer phosphorene close to the Fermi level are explored via a semianalytical approach. For that, we use a continuum approximation for multilayer phosphorene, derived from a fifteen hopping parameters tight-binding model, and consider the first-order light-matter interaction. This approach allows us, in a simple way, to calculate the momentum matrix elements

associated with polarized light in *x* and *y* directions, and then to obtain the total two-dimensional dielectric function of multilayer phosphorene extracted from Fermi's golden rule. The transition peaks in the total two-dimensional dielectric function are analyzed in view of the multilayer phosphorene band structure by taking different numbers of phosphorene layers.

Keywords: Phosphorene; vacancy defect; band unfolding; anisotropic transport; dielectric function.

RESUMO

Investigamos teoricamente as propriedades eletrônicas, de transporte e ópticas de multicamadas de fosforeno usando métodos numéricos e semianalíticos. Primeiramente, combinando o modelo tight-binding e a técnica de desdobramento de bandas, exploramos os efeitos das vacâncias atômicas na estrutura de bandas de multicamadas de fosforeno. Resultados para mono, di e tri-vacâncias são analisados mantendo ou não as simetrias das sub-redes e/ou subcamadas. Uma descrição detalhada da estrutura teórica utilizada é ilustrada para estruturas sem vacâncias de uma, duas e três camadas de fosforeno com empilhamento Bernal, o que nos permite identificar que a estabilidade da banda desdobrada efetiva depende do tamanho da supercélula do fosforeno com N camadas, revelando como adequada uma supercélula com tamanho de 6×6 células unitárias. Na presença de vacância, emerge na estrutura de bandas um estado quase n-dobradamente degenerado em um sistema com n vacâncias quando a simetria da sub-rede e/ou a simetria de inversão são quebradas. Dentro dessa abordagem combinada, também investigamos os efeitos das vacâncias devido a sua distribuição aleatória em nanofitas de fosforeno com bordas zigzag e armchair. Em segundo lugar, investigamos teoricamente o efeito de um campo elétrico aplicado perpendicularmente e a influência dos tipos de bordas (armchair e zigzag) na condutância e colimação da dinâmica de portadores de carga em junções de fosforeno de monocamada-bicamada, monocamada-bicamada-monocamada e bicamada-monocamada-bicamada. Utilizando o formalismo de Landauer-Büttiker e o modelo tight-binding, exploramos a densidade de corrente de probabilidade e a condutância em relação aos parâmetros do sistema, como energia de Fermi, magnitude do campo elétrico e comprimento da parede de domínio. Nossos resultados mostram que (i) tais propriedades físicas exibem uma forte dependência na orientação cristalográfica do modo eletrônico propagante e do tipo de interface devido à alta anisotropia nas bandas de energia, massas efetivas e velocidades de grupo do fosforeno com N camadas ao longo das direções x e y, (ii) modulações de corrente e (iii) uma dependência pronunciada na colimação dos feixes de elétrons na interface nas junções de multicamadas de fosforeno investigadas, obtidas aplicando um campo elétrico que quebra a simetria de inversão e causa um ajuste nas bandas próximas ao nível de Fermi, abrindo (fechando) o gap para monocamada (bicamada) de fosforeno. Todos os resultados são explicados no contexto da descontinuidade/alinhamento da estrutura de bandas do fosforeno com multicamadas entre as porções da junção. Finalmente, exploramos transições ópticas em multicamadas de fosforeno próximas ao nível de Fermi por meio de uma abordagem semianalítica. Para isso, usamos uma aproximação para o contínuo para multicamadas de fos-

foreno, derivada do modelo tight-binding com quinze parâmetros de hoppings, e consideramos a interação luz-matéria de primeira ordem. Essa abordagem nos permite, de forma simples, calcular os elementos da matriz de momento associados à luz polarizada nas direções x e y e, em seguida, obter a função dielétrica bidimensional total para multicamadas de fosforeno extraída da regra de ouro de Fermi. Os picos de transição na função dielétrica bidimensional total são analisados em relação à estrutura de bandas do fosforeno com multicamadas, levando em consideração diferentes números de camadas de fosforeno.

Palavras-chave: Fosforeno; defeitos de vacância; desdobramento de bandas; transporte anisotrópico; função dielétrica.

LIST OF FIGURES

LIST OF TABLES

LIST OF ABBREVIATIONS AND ACRONYMS

2D	Two-dimensional
ARPES	Angle-Resolved Photoemission Spectroscopy
BMB	bilayer-monolayer-bilayer
BP	Black phosphorus
BPNR-FET	Black Phosphorus Nanoribbons-Field Effect Transistor
BU	Band unfolding
CVD	Chemical Vapor Deposition
DFT	Density Functional Theory
DOS	Density of state
DV	Divacancy
DV1	Divacancy of type I
DV2	Divacancy of type II
EELS	Electron Energy Loss Spectroscopy
FET	Field-Effect Transitor
h-BN	Hexagonal Boron Nitride
HS-AFM	High-speed Atomic Force Microscopy
LCAO	Linear Combination of Atomic Orbital
LED	Light Emitter Diode
LPE	Liquid-Phase Exfoliation
MB	monolayer-bilayer
MBM	monolayer-bilayer-monolayer
ME	Mechanical Exfoliation
MV	Monovacancy
P	Phosphorus
PBZ	Primitive Brillouin Zone
PE	Plasma Etching
PL	Photoluminescence
PNR	Phosphorene nanoribbons
SBZ	Supercell Brillouin Zone
scPNR	Phosphorene nanoribbons-supercell
SEM	Scanning Electron Microscopy

STM	Scanning Tunneling Microscopy
STS	Scanning Tunneling Spectroscopy
TEM	Transmission Electron Microscopy
TMDs	Transition Metal Dichalcogenides
TV	Trivacancy
TV1	Trivacancy of type I
TV2	Trivacancy of type II
TV3	Trivacancy of type III

LIST OF SYMBOLS

4-MBD	4-methoxybenzene-diazonium
4-NBD	4-nitrobenzene-diazonium
Al_2O_3	Aluminium oxide
AlO_x	Aluminium oxide
$Ca(Ca_5F(PO_4)_3)$	Apatite, a mineral phosphate rock
CHP	N-cyclohexyl-2-pyrrolidone
DMF	Dimethylformamide
DMSO	Dimethyl Sulfoxide
h-BN	Hexagonal Boron Nitride
H_4O_{10}	Phosphorus pentoxide
HPO	Hydrogen phosphate
MoS_2	Molybdenum disulfide
Ne	Neon
NMP	N-methyl-2-pyrrolidone
P	Phosphorus
P_4	White phosphorus
PMMA	Polymethyl Methacrylate
Rb	Rubidium
Si	Silicon
SiO_2	Silicon oxide
SiO_2	Silicon oxide
O_2	Oxygen

CONTENTS

1 INTRODUCTION

The new era of electronic devices, driven by the technological need for component miniaturization, is being marked by the search for new materials capable of meeting the demands of evolution within dimensional boundaries and the laws imposed by nature. Since the early 20th century, with the invention and implementation of the transistor, the field of electronic devices has been heading toward the miniaturization of components. With progress in research, especially in nanotechnologies, the dimensional limits imposed by nature are being reached, and today the goal is not just the dimensional aspect, but also determining which material(s) have better potential to assume the primary role in the production and widespread application.

Silicon (Si) (Baker, 2018) still reigns supreme in the electronics industry, but it is believed that it will be replaced in this role shortly (Service, 2009). New two-dimensional (2D) materials such as the family of Transitions Metal Dichalcogenides (TMDs), graphene, and phosphorene have emerged in recent years as strong candidates to take over this position. Among the new 2D materials capable of replacing Si , phosphorene stands out with some advantages over the others. Phosphorene is a natural semiconductor with a gap ranging from ≈ 0.33 eV (*Bulk*) to 1.8 eV (*monolayer*) and high electronic mobility (Tran *et al.*, 2014; Li *et al.*, 2014; Liu; Neal, 2014; Castellanos-Gomez, 2015; Chaves *et al.*, 2021; Das *et al.*, 2014; Kim *et al.*, 2015; Dolui; Quek, 2015a), while TMDs have relatively low electronic mobility, which limits their applicability in nanotechnology (Xia; Wang; Jia, 2014). On the other hand, graphene does not have an energy gap under ambient conditions and exhibits Dirac electronic dispersion (Geim, 2009; Avouris; Xia, 2012).

Phosphorene is a layer of black phosphorus (BP), an allotrope of phosphorus produced synthetically under high temperatures and pressures. The recent discovery of phosphorene exfoliation (Li *et al.*, 2014; Castellanos-Gomez *et al.*, 2014) and the experimental and theoretical confirmation of some of its properties have put it in the spotlight in worldwide research for new 2D materials. Among these valuable properties are the electronic transition between valence and conduction bands through a direct bandgap, high electronic mobility, and significant optical absorption power (Rodin; Carvalho; Neto, 2014; Liu; Neal, 2014). Its characteristics make it suitable for a wide range of applications, such as electronic, optoelectronics, and spintronics devices, among others (Akhtar *et al.*, 2017). Several theoretical models support and provide predictions about its main properties. Theses range from first principles methods (Tran *et al.*, 2014; Jing; Park, 2014; Fei; Yang, 2014; Wei; Peng, 2014; Qin *et al.*, 2015; Shriber *et al.*,

2018) to semiempirical methods, such as tight-binding (Takao; Asahina; Morita, 1981; Rudenko; Katsnelson, 2014a; Rudenko; Yuan; Katsnelson, 2015; Sousa *et al.*, 2017b; Lino *et al.*, 2017; Melo *et al.*, 2018; Jr; Katsnelson, 2015; Sousa *et al.*, 2016; Sousa *et al.*, 2017a; Cunha *et al.*, 2019). Theoretical research is usually based on simplifications of ideal systems. However, when applying these theories, it is necessary to take into account situations close to reality, to obtain relevant results within an acceptable regime, since the extraction of two-dimensional type materials in a controlled environment provides samples that are far from representing an ideal theoretical system. After the extraction process, the samples present diversified structures, with defects such as vacancy and superposition of layers of nanoribbons generating regions of junctions. When we experimentally analyze the electronic properties of these structures, what we observe are significant changes in them, highlighting the need to incorporate real-world approximations in ideal theoretical models.

In this regard, we theoretically study two types of structures in this Thesis. The first one, which has received considerable attention in ongoing research, involves analyzing atom vacancy defects in a phosphorene supercell. Defects of this nature are often observed after the exfoliation process of phosphorene and can cause significant changes in its properties (Li *et al.*, 2015; Zhang; Wu; Yang, 2016; Lei *et al.*, 2017b; Lei *et al.*, 2017a; Kistanov *et al.*, 2016; Smotlacha; Pincak, 2018; Sun *et al.*, 2018; Arra; Babar; Kabir, 2019; Li; Peeters, 2018; Kiraly *et al.*, 2017; Harsh *et al.*, 2022; Huang *et al.*, 2022; He *et al.*, 2019; Zhan *et al.*, 2019; Li *et al.*, 2022; Aghajanian; Mostofi; Lischner, 2022; Fang *et al.*, 2022; Rijal *et al.*, 2021; Rezaei *et al.*, 2021; Gupta; Periasamy; Narayanan, 2021; Yao *et al.*, 2020; Pei *et al.*, 2020; Kundu; Naik; Jain, 2020; Wang *et al.*, 2015; Kripalani *et al.*, 2019; Shah *et al.*, 2019; Cai *et al.*, 2019; Amini *et al.*, 2019a; Amini *et al.*, 2019b; Riffle *et al.*, 2018; Cai *et al.*, 2016; Gaberle *et al.*, 2018; Hu *et al.*, 2015; Farooq *et al.*, 2015; Dai *et al.*, 2017), giving us a new possibility to control them. Investigations on phosphorene nanoribbons show that the behavior of its electronic properties can undergo changes depending on the position (Smotlacha; Pincak, 2018; Sun *et al.*, 2018) and type of vacancy (Li; Peeters, 2018). For this analysis, we used the Band unfolding technique. Investigating crystalline structures using the Band unfolding model enables us to conduct a more realistic analysis of its electronic properties. Recent works conducted with this technique have demonstrated how the properties of crystals can be altered when a non-ideal crystal lattice is proposed (Zang; Wang, 2011; Medeiros *et al.*, 2014; Cui *et al.*, 2015; Maspero *et al.*, 2016; Nishi *et al.*, 2017; Babar *et al.*, 2018). The foundations of Band unfolding theory are well-defined in

the literature (Boykin; G., 2005; Boykin *et al.*, 2007; Ku *et al.*, 2010; Popescu; Zunger, 2010; Popescu; Zunger, 2012; Allen *et al.*, 2013; Diretzis *et al.*, 2014; Huang *et al.*, 2014; Boykin *et al.*, 2016; Medeiros *et al.*, 2015). The analysis using the Band unfolding is based on the construction of a supercell, through which we can explore the effects caused by vacancies on its electronic properties. This work proposes the analysis of the band structure of monolayer, bilayer, and trilayer phosphorene with vacancy defects using the Band unfolding method.

In the second one, we analyze the electronic transport in interface regions of junctions between monolayer and bilayer phosphorene nanoribbons. Samples of few-layer two-dimensional materials extracted from their bulk versions often contain patches with different numbers of layers in the same region of the sample. The possibility of finding new physical properties related to interfaces between areas with a distinct number of layers has led in the last two decades to several studies on electronic (Wang *et al.*, 2016; Lane *et al.*, 2018; Jaskólski *et al.*, 2018) and transport (Ju *et al.*, 2015; Abdullah *et al.*, 2017; Jamaati; Namiranian, 2017; Abdullah *et al.*, 2018) properties. In most cases, as in graphene monolayer and bilayer junctions, the two portions have qualitatively different band structures, so that new effects, not observed in each portion separately, can arise. Recent work addressing graphene monolayer and bilayer junctions showed that the transport properties are strongly affected by the geometry of the interfaces (Chico *et al.*, 2012; Nakanishi *et al.*, 2010; Mirzakhani *et al.*, 2017; Mirzakhani *et al.*, 2018). Following the example of few-layer graphene-based planar junctions(Chu *et al.*, 2017), a natural research direction is to investigate similar physical systems composed of other 2D materials, in particular, anisotropic semiconductors since such materials are expected to exhibit physical properties significantly different from those found in typical semiconductors due to the highly anisotropic band structure. In this sense, the existence of both monolayer and bilayer portions in exfoliated phosphorene samples motivated us to investigate the transport properties of hybrid phosphorene junctions, which consist of monolayer phosphorene portions coupled to bilayer phosphorene portions, formed by one or two interfaces, such as monolayer-bilayer (MB), monolayer-bilayer-monolayer (MBM), and bilayer-monolayer-bilayer (BMB). Therefore, we study how the conductances and trajectories of electron beams are affected due to the presence of phosphorene junctions with armchair or zigzag interfaces subjected to an electric field perpendicular to the propagation direction along the z-direction.

This Thesis is organized into four parts: In the first part, we divide it into four chapters. The first chapter, in addition to this motivational introduction, the first section provides

a historical review that covers the black phosphorus allotrope from its discovery to its main applications and prospects. Additionally, in the second section, a survey is conducted on the main types of crystal defects, with an emphasis on vacancy defects. The tight-binding model is presented in the second chapter, and the Band unfolding techniques and the Landauer-Büttiker formalism are presented in chapters three and four, respectively. In the second part, we have only one chapter where we present the results of our investigation on the effects of vacancies on the band structure in phosphorene multilayers. In the third part, also with only one chapter, we present the results of how the conductances and trajectories of electron beams are affected due to the presence of phosphorene junctions with armchair or zigzag interfaces subjected to an electric field perpendicular to the propagation direction. Lastly, in the fourth and final part, we present the final considerations with our main conclusions and perspectives.

1.1 Black phosphorus: from discovery to application

The element Phosphorus (P) is part of Group 15 of the periodic table, being among the elements that have 5 electrons in their outermost shell ([Ne] $3s^2$ $3p^3$). It is found in significant proportions in nature and is the 12th most abundant element in the lithosphere. The element P and its allotropes have enormous importance in various areas of scientific knowledge, ranging from essential functions in living organisms (Ashley *et al.*, 2011), to the production of explosives (Nitschke, 2011), and fertilizers (De-Bashan; Bashan, 2004), to important applications in optoelectronic devices (Xia; Wang; Jia, 2014). Its discovery was made by Hennig Brandt in 1669 when he obtained the first samples of white phosphorus from human urine (Emsley; Huxtable, 2000). Due to its glow in the dark and its high combustion power when in contact with oxygen, it inherited the name derived from Greek mythology given to the planet Venus, *phosphorus* (*phos*=light, *phorus*=bearer), which in Latin was known as the "morning star". Today, the main sources of phosphorus are mineral phosphate rocks, with the most common one being *apatite* ($Ca_5F(PO_4)_3$) (Ashley *et al.*, 2011).

Among the wide variety of phosphorus allotropes, the most common ones are white phosphorus (P_4) and red phosphorus. P_4 is highly reactive when exposed to oxygen, resulting in the formation of compounds such as HPO and P_4O_{10} through combustion (Nitschke, 2011; Thomas; Pierzynski, 2005). Its crystalline structure at ambient conditions is body-centered cubic, taking on a second hexagonal form at temperatures around $\approx$ -78^{0}C (Averbuch-Pouchot; Durif, 1996). Red phosphorus can be obtained by subjecting white phosphorus to high temperatures

(252-277^{0}C) in a sealed system. Red phosphorus, when subjected to melting, transitions into its amorphous form, which, in turn, can exhibit variations such as violet phosphorus (or Hittorf's phosphorus). These P allotropes are widely used for military purposes and in the commercial manufacturing of household matches. If white phosphorus is subjected to high temperatures and pressures, a less common and more stable P allotrope under ambient conditions is formed: BP (Ahuja, 2003). Despite the study of this allotrope dating back to the early 20th century, the notability of BP as a new type of 2D material emerged in 2014 when a single layer was extracted from a bulk material to fabricate a Field Effect Transistor (FET). Some properties of BP bulk were already well-known, such as its band structure, which had been studied theoretically and experimentally. However, obtaining it in the form of a 2D material opens up a new range of opportunities in terms of its optical and electronic transport properties and characteristics, making it, like graphene, a prominent player in the current landscape of scientific and technological innovation.

1.1.1 Synthesis and preservation

BP is not a little-known material in science; on the contrary, its incidental discovery dates back to the early 20th century when Bridgman (1914) subjected white phosphorus to high pressures and temperatures, resulting in the formation of two new forms of P allotropes. One of them was a reversible form of white phosphorus, referred to as white phosphorus II, under certain conditions. The other was an irreversible form that he named BP . Bridgman's method involved subjecting white phosphorus to a pressure of 1300 MPa and a temperature of 200^{0}C in a steel cylinder under kerosene. After mechanical agitation and separation, two distinct forms were identified. The first had the appearance of crystalline sugar, although it did not exhibit crystalline characteristics under a microscope. The other had a fibrous aspect with a metallic luster, resembling graphite (Bridgman, 1914; Maciá, 2005).

In 1953 Bridgman's method was refined by Keyes (1953), who reproduced the experiment and highlighted the violent transition of one material to another and the volume variation of the samples, resulting in a significant increase in density (from 1.823 g/cm^3 to 2.691 g/cm^3). In addition, measurements of properties such as energy gap (0.33 eV), resistivity (1.5 ohm·cm), and electron mobility (220 cm^2/V.s) and hole mobility (350 cm^2/V.s) were conducted at room temperature. The high anisotropy of the BP crystal was also observed, indicating that it possessed similar characteristics to other 2D materials. Shortly before Keyes' refinement, BP

had been obtained at room temperature by Bridgman at pressures above 8,000 MPa (Bridgman, 1948). Single crystals of BP were first obtained in 1981 by applying pressures of 3,800 MPa and temperatures above 270^0C to molten red phosphorus (Shirotani, 1982).

Another method for obtaining BP was prepared using the bismuth flux method. Purified white phosphorus was dissolved in liquid bismuth and heated to approximately 300-400^0C, maintaining this temperature for 20 hours. Crystals with dimensions of $5\times0.1\times0.07$ mm^3 were obtained using this technique (Baba *et al.*, 1989). Another approach to obtain BP was explored by Lange *et al*. in 2007, starting from red phosphorus at low pressure and a temperature of 873 K (Lange *et al.*, 2007). By adding small amounts of tin iodide, tin, and gold, and allowing a duration of 5-10 days, this process, which was later improved, obtained individual crystals of BP with good quality (Nilges *et al.*, 2008; Köpf *et al.*, 2014; Aldave *et al.*, 2016) (Figure 1).

In 2014, BP emerged as a viable candidate for a new 2D material, similar to graphene, with potential applications in electronic devices due to its intriguing properties. The production of this material in a few-layer form and its characteristic of having a direct band gap was first explored in the context of a FET transistor (Li *et al.*, 2014). Since then, black phosphorus has gained significant attention within the scientific community, becoming the subject of numerous theoretical and experimental studies (Carvalho *et al.*, 2016a; Akhtar *et al.*, 2017; Castellanos-Gomez *et al.*, 2014; Liu; Neal, 2014; Castellanos-Gomez, 2015; Dolui; Quek, 2015a; Das *et al.*, 2014; Kim *et al.*, 2015; Chaves *et al.*, 2021; Tran *et al.*, 2014; Jing; Park, 2014; Fei; Yang, 2014; Wei; Peng, 2014; Qin *et al.*, 2015; Shriber *et al.*, 2018; Takao; Asahina; Morita, 1981; Rudenko; Katsnelson, 2014a; Rudenko; Yuan; Katsnelson, 2015; Sousa *et al.*, 2017b; Lino *et al.*, 2017; Melo *et al.*, 2018; Jr; Katsnelson, 2015; Sousa *et al.*, 2016; Sousa *et al.*, 2017a; Cunha *et al.*, 2019). The methods for producing few-layer BP have rapidly improved, and it is now possible to obtain a single layer of the material with high quality. The main methods of obtaining BP are: Mechanical Exfoliation (ME) (Liu; Neal, 2014), Plasma Etching (PE) (Lu *et al.*, 2014), Chemical Vapor Deposition (CVD) (Smith *et al.*, 2016), and Liquid-Phase Exfoliation (LPE) (Brent *et al.*, 2014a). ME refers to the tape-based exfoliation method widely used in the process of exfoliating layers of graphene (Novoselov *et al.*, 2005) and MoS_2 (Molybdenum disulfide) (Li *et al.*, 2012). The PE technique enables the precise obtainment of single layers of phosphorene. The process described by Wood *et al*., as shown in Figure 2 (b) involves O_2 (Oxygen) plasma treatment followed by Al_2O_3 (Aluminium oxide) passivation. In addition to enabling layer-by-layer exfoliation, the method provides the capability to design defects in the

Figure 1 – (a) Allotropes of P derived from white phosphorus: red phosphorus (above 280^0C), violet phosphorus (1-2 weeks, above 550^0C), and black phosphorus (under high pressures). (b) Obtaining black phosphorus from red phosphorus with S_nI_4 at high temperatures ($500\text{-}600^0$C).

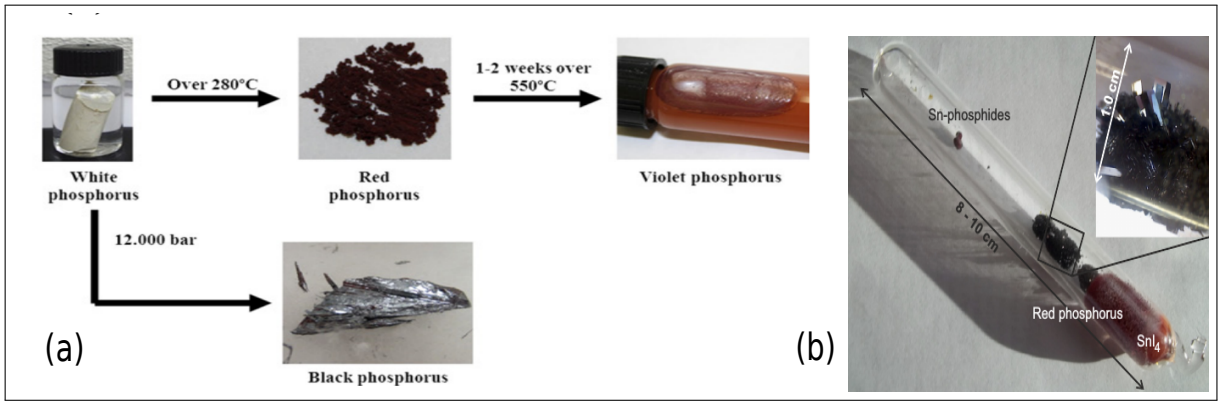

Source: Figure adapted from references (Aldave *et al.*, 2016; Köpf *et al.*, 2014).

material (Wood *et al.*, 2014; Pei *et al.*, 2016).

The CVD exfoliation technique provides a controlled method for producing high-quality 2D materials, and its advantages make it an important tool for the exploration of 2D materials. The process involves gas-phase reactions of the precursor materials on the surface of substrates, resulting in the formation of solid products. Characteristics such as the number of layers and crystal size can be controlled by tuning parameters such as temperature, pressure, and sample quantity (Smith *et al.*, 2016; Cai *et al.*, 2018).

LPE stands out from other methods as it is capable of producing 2D materials on a large scale (Carvalho *et al.*, 2016a). This technique involves ultrasonic exfoliation of phosphorene immersed in appropriate solvents such as dimethylformamide (DMF), dimethyl sulfoxide (DMSO) (Yasaei *et al.*, 2015a), N-methyl-2-pyrrolidone (NMP) (Kang *et al.*, 2015; Brent *et al.*, 2014b), and N-cyclohexyl-2-pyrrolidone (CHP) (Sotor *et al.*, 2015). The LPE procedure allows for the exfoliation of isolated layers of phosphorene with high quality (Hanlon *et al.*, 2015). One of the challenges in the industrial application of PH in electronic components is its stability. A secure and large-scale production program is still one of the bottlenecks in its production (Wang; Lan, 2016). Despite being the most stable allotrope, phosphorene can still react with the surrounding environment and undergo degradation. When exposed to air under ambient conditions (temperature $24\text{-}27^0$C, relative humidity 40-45%), roughness and bubble-like structures appear on its surface within a few hours, rendering it hydrophilic and increasing its volume. Oxidation is accelerated with the reduction of layers and when processes involve light and water (Favron *et al.*, 2015).

Figure 2 – (a) Characterization steps of phosphorene exfoliation by LPE. Images of structures obtained through scanning electron microscopy (SEM) and transmission electron microscopy (TEM). (b) Process of phosphorene exfoliation by O2 PE on SiO_2 (Silicon oxide) substrate coated with Al_2O_3.

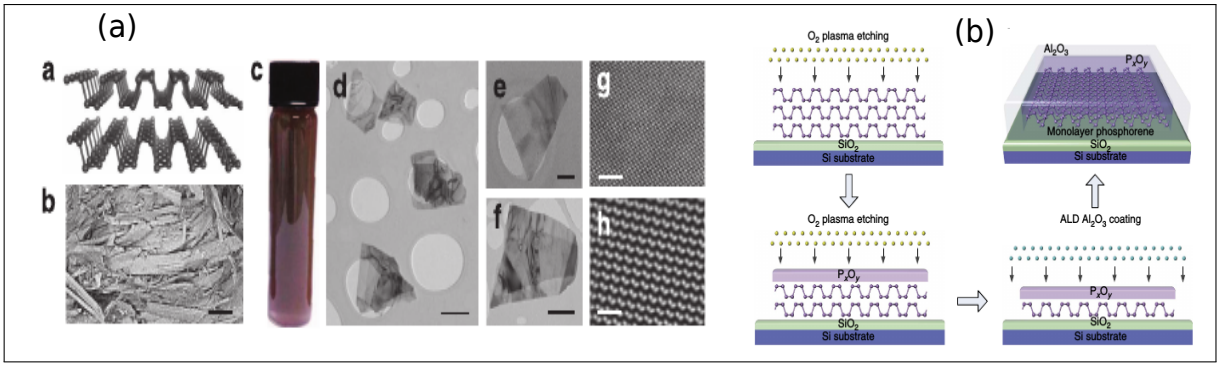

Source: Figure adapted from references (Hanlon *et al.*, 2015; Pei *et al.*, 2016).

Several methods have been developed to stabilize phosphorene and prevent its degradation. Passivation of few-layered material is achieved through encapsulation with polymethyl methacrylate (PMMA) (Cao *et al.*, 2015), hexagonal boron nitride (h-BN) (Doganov *et al.*, 2015), 4-nitrobenzene-diazonium (4-NBD), and 4-methoxybenzene-diazonium (4-MBD), as shown in Figure 3 (a) (Ryder *et al.*, 2016), as well as aluminum oxide (AlO_x) (Wood *et al.*, 2014; Ryder *et al.*, 2016) with significant success. PMMA was not only the first material used for industrial encapsulation of phosphorene but also employed in preliminary isolation steps with other materials (Mittal, 2013).

Encapsulation of phosphorene between h-BN layers has proven to be an important method for isolating the material from the external environment, as shown in Figure 3 (b). Phosphorene is resistant to oxidation and offers the advantage of flexibility during material assembly. The process utilizes graphene contacts for the complete fabrication of stacked 2D heterostructure transistors (Avsar *et al.*, 2015). The results obtained with 4-NBD and 4-MBD solutions are similar. The phosphorene layers are immersed in the solutions, and notable improvements in their morphology are observed after 30 minutes of functionalization. During 25 days of exposure under ambient conditions, the sample did not undergo significant morphological changes. However, after this period, pronounced differences were observed in its morphological structure (Ryder *et al.*, 2016). Among the various methods of passivation, the encapsulation of phosphorene with AlO_x stands out as a promising approach for industrial-scale applications (Akhtar *et al.*, 2017). Transistors with a 25 nm and 30 nm thick Al_2O_3 coating have been produced, resulting in significant improvements such as enhanced moisture resistance (Kim *et al.*, 2015) and hole mobility of 46 cm^2/V.s (Xia; Wang; Jia, 2014). It has been observed that

Figure 3 – (a) Schematic diagram of the passivation of phosphorene by 4 - methoxybenzene - diazonium. (b) A device with phosphorene encapsulation by h-BN with graphene contacts.

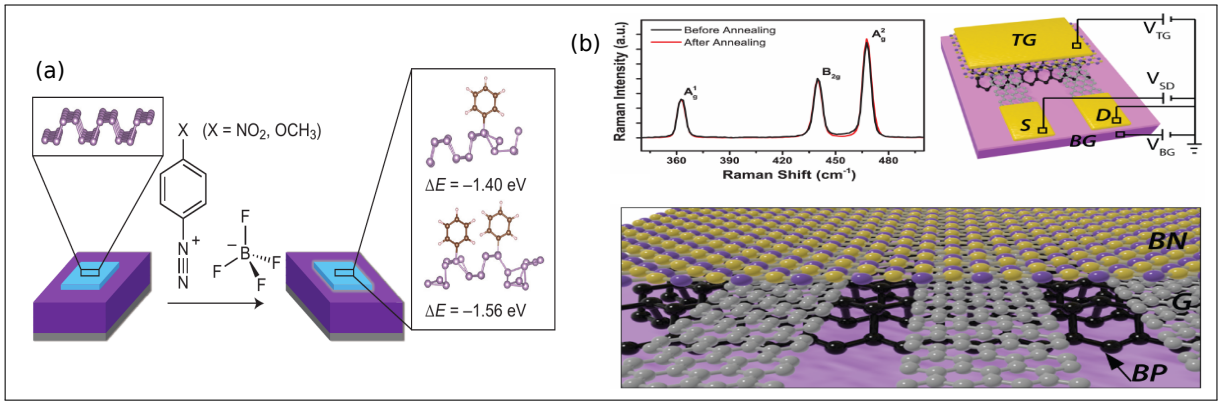

Source: Figure adapted from references (Ryder *et al.*, 2016; Avsar *et al.*, 2015).

the noise level in currents decreases throughout the operating range of the black phosphorus transistor with passivation. Additionally, Raman spectroscopy confirmed that the morphology of the samples remained preserved under ambient conditions for a period of two months (Na *et al.*, 2014a).

Phosphorene nanoribbons (PNRs) has been widely studied by theoretical methods (Lee *et al.*, 2015b; Sorkin *et al.*, 2017; Guo *et al.*, 2014; Carvalho *et al.*, 2014; Hu *et al.*, 2017; Nourbakhsh; Asgari, 2016; Das *et al.*, 2016; Yang *et al.*, 2016; Sisakht *et al.*, 2016; Wu *et al.*, 2016; Poljak; Suligoj, 2016; Yang *et al.*, 2016; Wu *et al.*, 2015; Zhang *et al.*, 2014; Yao *et al.*, 2015) since its emergence as a material applicable in electronic devices, attracting significant attention from researchers due to their fascinating characteristics arising from the distinctive 2D structure of phosphorene and the added quantum confinement resulting from the nanoribbon boundaries. This exploration of PNRs presents a novel approach for developing materials with enhanced electronic and optoelectronic properties, opening up exciting possibilities for various applications. However, its experimental extraction has only emerged in recent years (Watts *et al.*, 2019; Pacchioni, 2019; Yu *et al.*, 2021; Abu *et al.*, 2022) and the production of this material with hight-quality is still a challenge. Figure 4 compares the lengths and widths of PNBs produced by some works in recent years.

We highlight here the work of Watts *et al.* (2019) where individual PNRs with high quality were produced using ionic scissoring of macroscopic black phosphorus crystals. Through the implementation of a top-down approach, a remarkable outcome is achieved in the form of stable liquid dispersions containing PNRs. These nanoribbons exhibit characteristic widths ranging from 4 to 50 nm, primarily consisting of a single layer in thickness, Figure 5 (a). Their

Figure 4 – Comparison of size distribution of PNRs obtained experimentally.

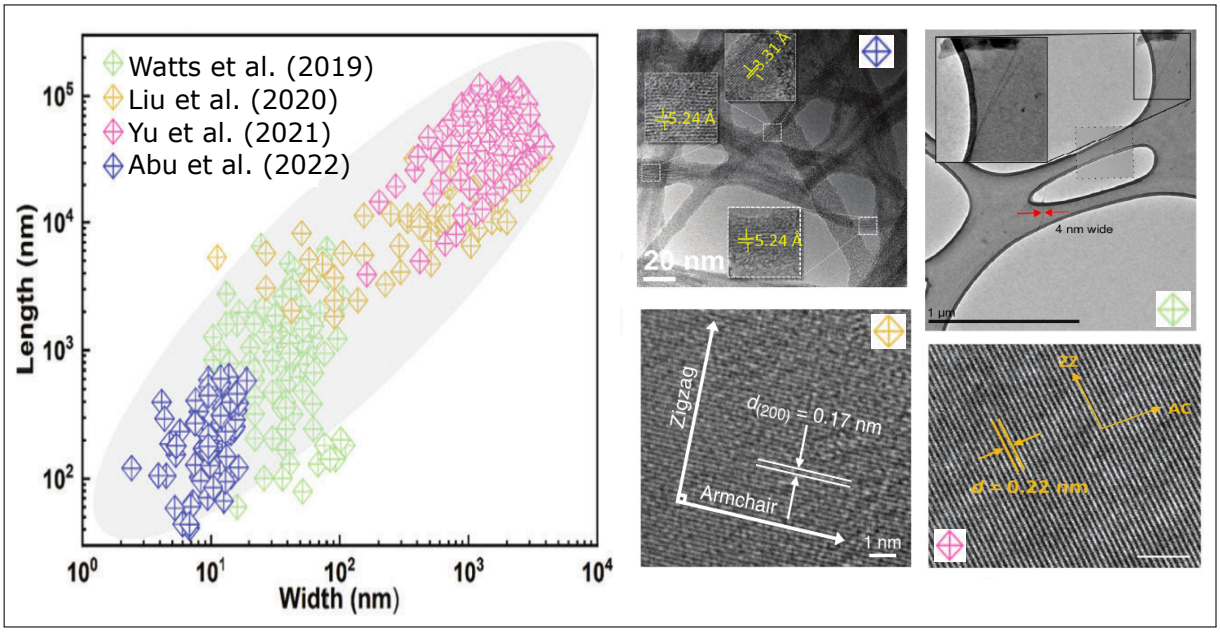

Source: Figure adapted from reference (Abu *et al.*, 2022).

measured lengths can extend up to 75 μm, while their aspect ratios reach impressive values of up to 1,000. It is noteworthy that these nanoribbons possess atomically flat surfaces, akin to single crystals, and their alignment is exclusively oriented in the zigzag crystallographic direction. This one exhibits high flexibility and widths and lengths uniformity. The exceptional uniformity in width along the entire length of the ribbons, combined with their remarkable flexibility, makes them highly suitable for downstream manipulation using liquid-phase methods. This ease of manipulation opens up avenues for exploring predicted exotic states and a diverse range of applications where PNRs are anticipated to deliver transformative benefits. These applications span various fields, including thermoelectric devices, high-capacity fast-charging batteries, and integrated high-speed electronic circuits. The unique properties of PNRs make them a promising candidate for advancing these technologies.

Figure 5 (b) show the image of high-speed atomic force microscopy (HS-AFM) a bifurcated nanoribbons multilayers of a nanoribbon longer than 75 μm. Line profiles at the branching points reveal that the split in the ribbon is caused by the self-cleaving of the multilayer ribbon, which leads to branching occurring at several intervals along its length, particularly in long ribbons. In Figure 5 (c), the presented graph displays the photoluminescence (PL) spectrum of aggregated PNRs deposited on a graphite substrate. The high-energy peaks observed can be attributed to Raman features originating from either the PNRs or the graphite substrate (*). It is noteworthy that single-layer phosphorene, obtained through mechanical exfoliation, emits light

Figure 5 – (a) PNRs exhibit characteristic widths ranging from 4 to 50 nm, primarily consisting of a single layer in thickness. Furthermore, in the right, a scatterplot of PNR length as a function of width for 940 PNRs, measured using TEM. (b) Image of HS-AFM a bifurcated nanoribbons multilayers of a nanoribbon longer than 75 μm. (c) PL spectrum of aggregated PNRs deposited on a graphite substrate. The high-energy peaks observed can be attributed to Raman features originating from either the PNRs or the graphite substrate. (d) EELS) analysis of black phosphorus, distinct features can be observed in three regions, namely regions I, II, and III, typically found in pristine few-layer black phosphorus. The low-loss EELS spectrum demonstrates the presence of expected plasmonic signature peaks, with one peak appearing at approximately 19 eV.

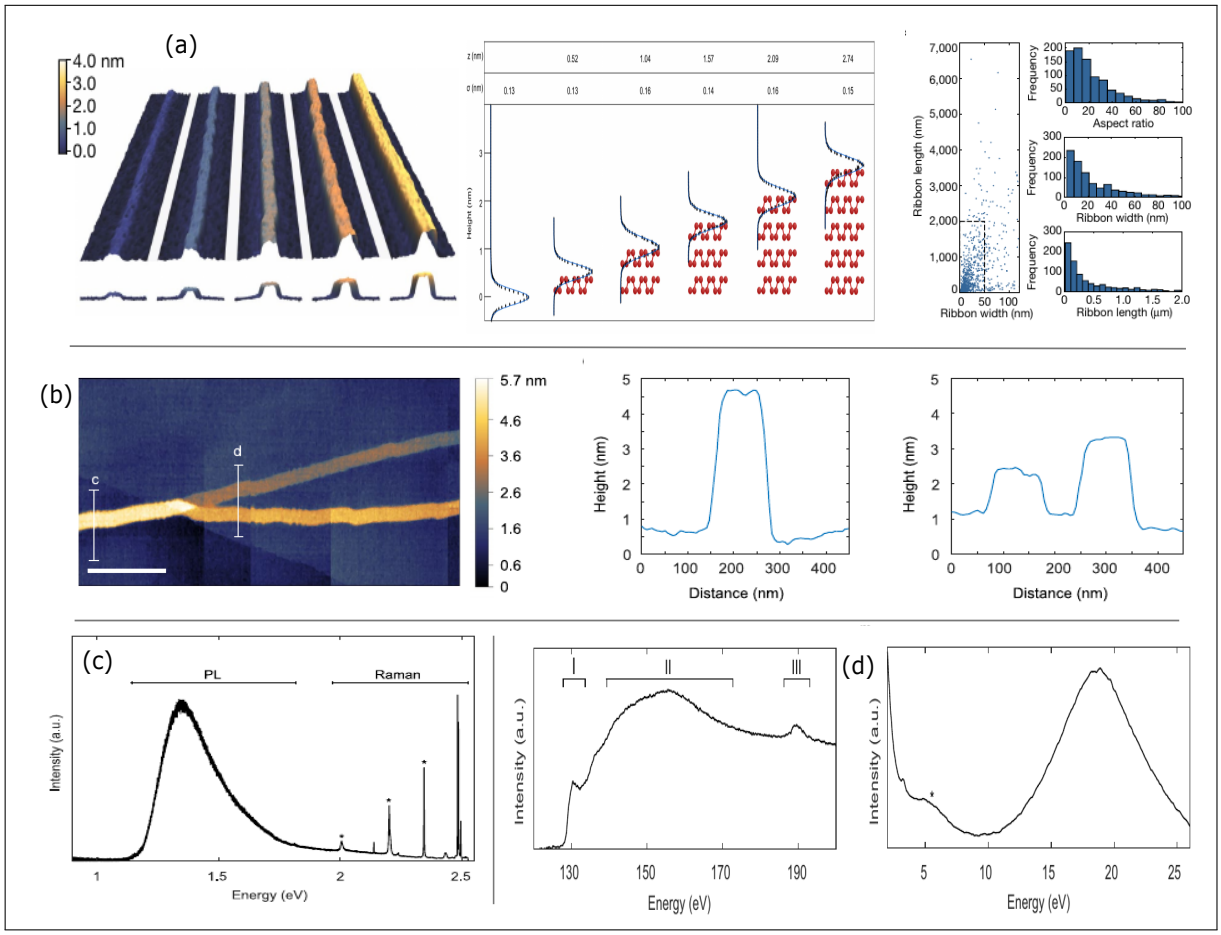

Source: Figure adapted from references (Watts *et al.*, 2019; Pacchioni, 2019; Yu *et al.*, 2021)

at approximately 1.3 eV.

In the electron energy loss spectroscopy (EELS) analysis of BP, distinct features can be observed in three regions, namely regions I, II, and III, in Figure 5 (d). These features are consistent with those typically found in pristine few-layer black phosphorus. Furthermore, the low-loss EELS spectrum demonstrates the presence of expected plasmonic signature peaks, with one peak appearing at approximately 19 eV. Another notable feature is observed around 3.3 eV, which resembles the characteristic found in few-layer BP and is associated with surface plasmons.

1.1.2 Crystalline structure

The crystal structure of phosphorene is composed of an orthorhombic layered lattice, and its structural parameters are typically determined through X-ray diffraction (Brown; Rundqvist, 1965) and *time-of-flight neutron powder diffraction* (Cartz *et al.*, 1979a). Various theoretical studies on electronic and optoelectronic properties are conducted based on experimentally obtained lattice parameters, and their results support and predict interesting properties in PH. Each P atom in PH forms covalent bonds with three other atoms, resulting in simple covalent bonds. The unit cell of phosphorene contains four atoms, with two in one plane and two in another, and the planes are separated by a distance c = 2.33 nm. Despite this separation, a single phosphorene layer is considered a 2D material, and the difference between the planes corresponding to atoms AB and CD is seen as a wrinkling of the material. The lattice constants a_x, a_y, and a_z for the bulk have values of 0.4374 nm, 0.3313 nm, and 1.0473 nm, respectively. The constant a_x is along the x-axis (armchair), a_y is along the y-axis (zigzag), and a_z is along the layer stacking axis z. The distance between atoms along the bonding axis is a = 0.2222 nm for atoms A and B (C and D), and a = 0.2227 nm for atoms A and C (D and B) (Wang; Lan, 2016). Unlike P_4 (white phosphorus), where the arched bonds (Pauling; Simonetta, 1952; Hart *et al.*, 1965) of the 3p orbitals make them highly unstable, the atoms in the phosphorene crystal form angles between each other of 96.34° and 103.09°, which approach the angle of a perfect tetrahedral structure, resulting in greater stability (Carvalho *et al.*, 2016a; Akhtar *et al.*, 2017), Figure 6 (b). The layers of phosphorene are bound together by van der Waals interactions, resulting from the lone pair of electrons left over from the sp^3 bonding of each P atom, Figure 6 (d). This pair of electrons, in a single layer of phosphorene, forms an electron cloud with a 45° angle external to the plane. The resulting structure, when viewed from a perspective above the x-y plane, has a hexagonal geometry, similar to graphene and Boron Nitride, Figure 6 (c). This geometry results in a density of 2.69 g/cm^3, higher than that of P_4 (1.67 g/cm^3), and is also responsible for the anisotropic compressibility of the material. The PH crystal exhibits different variations along its axes (x (a), y (b), and z (c)) when subjected to stresses (compression/extension). An unusual elastic behavior of phosphorene has been observed, with a much higher elastic tensor value in the y-direction (191.9) compared to the other x-directions (52.3) and z (73.0). As a result, the Poisson's ratio (x/y) calculated for the x and y directions is considered to be very large (0.93), while for the z and y directions, it is negative (-0.027). This means that stretching the material in one direction causes an increase in size in the other direction, which is considered unusual.

Figure 6 – (a) High-resolution images of phosphorene via TEM for monolayer and stacked layers. Electron diffraction in exfoliated phosphorene nanoflakes (b) Lattice parameters of the primitive cell of phosphorene. (c) 4×4 supercell with dimensions L_x and L_y. (d) Trilayer stacking of phosphorene nanoflakes, with separation distances given by d_1 and d_2.

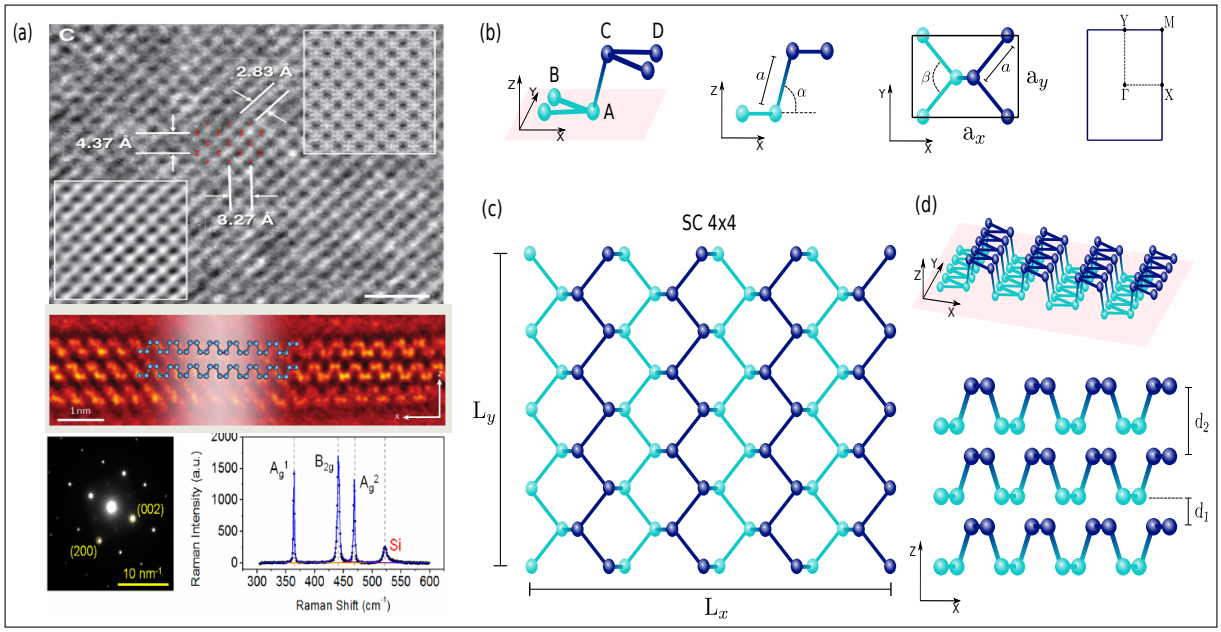

Source: Figure adapted from references (Carvalho *et al.*, 2016a; Yasaei *et al.*, 2015b; Kang *et al.*, 2015)).

Under pressure, the most significant variations occur in the y-direction (zigzag) and z-direction (stacking), while the x-direction (armchair) undergoes minimal changes (Cartz *et al.*, 1979a; Kikegawa; Iwasaki, 1983).

Additionally, phosphorene can exhibit reversible phases under high pressures. Above 5500 MPa at room temperature, the crystal undergoes a structural transition from the orthorhombic phase to the rhombohedral (trigonal) phase, leading to changes in the wrinkling and volume of the sample. With further increasing pressure, the rhombohedral phase transitions to a simple cubic phase at a pressure of 10000 MPa, regardless of temperature (Cartz *et al.*, 1979a; Kikegawa; Iwasaki, 1983; Clark; Zaug, 2010; Burdett; Lee, 1982).

1.1.3 Electronic properties

One of the main advantages of phosphorene over other 2D materials is its direct band gap. For the bulk material, the lowest energy value between the valence and conduction bands is approximately 0.3 eV and is located at the Γ point, as shown in Figure 7 (a). On the other hand, a monolayer of phosphorene has a band gap value of approximately 2.0 eV, which decreases with an increasing number of layers in the material (Carvalho *et al.*, 2016a;

Liu; Neal, 2014; Akhtar *et al.*, 2017; Goswami; Gawande, 2019), and it remains direct. This is in contrast to materials like MoS_2 and WS_2, which undergo a transition from a direct to an indirect band gap as the number of layers increases (Qiao *et al.*, 2014). Furthermore, the energy gap can also be tuned through doping, application of electric fields, chemical functionalization, and strain (compression/extension), providing phosphorene with broad prospects in the field of photocatalysis (Goswami; Gawande, 2019).

From the sp^3 bonding of the P atom in the BP lattice, the orbitals that contribute the most to the formation of the CB and VB are the s and p_z orbitals, resulting from the hybridization of the s, p_x, p_y, and p_z orbitals (Li *et al.*, 2019; Lopez-Bezanilla, 2016), as shown in Figure 7 (b). Experimentally, the energy gap values for a single layer, few layers, and many layers are obtained using photoluminescence methods (Liu; Neal, 2014; Zhang *et al.*, 2014). Theoretical works using *ab initio* (Tran *et al.*, 2014; Jing; Park, 2014; Fei; Yang, 2014; Wei; Peng, 2014; Qin *et al.*, 2015; Shriber *et al.*, 2018) and tight-binding approaches (Takao; Asahina; Morita, 1981; Rudenko; Katsnelson, 2014a; Rudenko; Yuan; Katsnelson, 2015; Sousa *et al.*, 2017b; Lino *et al.*, 2017; Melo *et al.*, 2018; Sousa *et al.*, 2016; Sousa *et al.*, 2017a; Cunha *et al.*, 2019) providing a good approximation of the experimental values. Recently, the dependence of the energy gap on the number of layers was theoretically studied by Duarte *et al*., who derived an analytical expression for the gap energy as a function of the number of layers (Sousa *et al.*, 2017a). The energy range covered by phosphorene (from approximately 0.3 eV to 2.0 eV) is

Figure 7 – (a) Band structure calculated by Density Functional Theory (DFT) for monolayer, bilayer, trilayer, and bulk phosphorene around the center (Γ point) of the first Brillouin zone of the system. (b) Band structure for phosphorene with s, p_x, p_y, p_z parametrization using first principles methods (DFT).

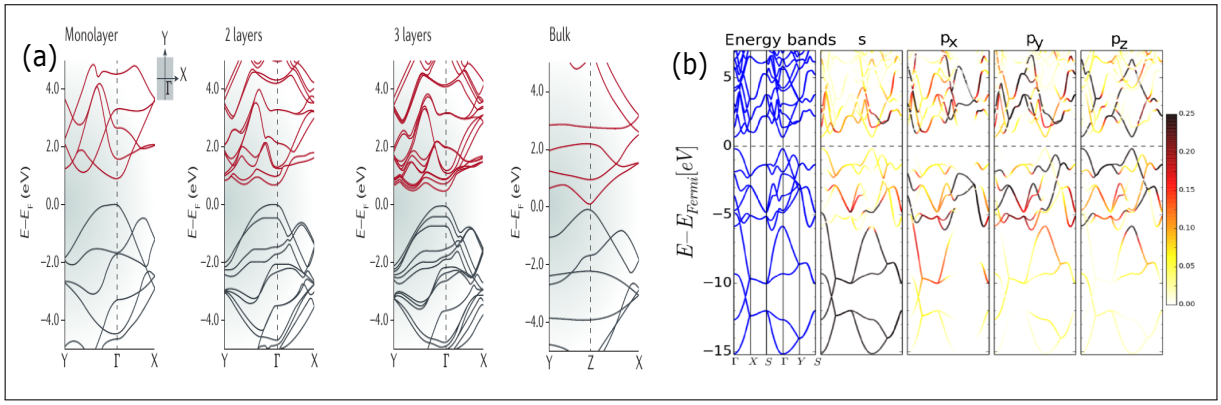

Source: Figure adapted from reference (Carvalho *et al.*, 2016a)

another advantage over other 2D materials such as graphene (zero gap) and TMDs (indirect gap), spanning from the visible to the infrared range.

Just like the anisotropic compressibility discussed in the previous section 1.1.2, the geometric structure of phosphorene also influences its electronic structure, resulting in a highly anisotropic band structure. The effective mass for electrons and holes in the y-direction (zigzag) is approximately 10 times greater than in the x-direction (armchair) (Low *et al.*, 2014). This direction-dependence characteristic significantly affects the electronic and optical properties of the material. In phosphorene nanoribbons, the dependence of the energy gap changes in the confinement directions. When confined along the zigzag direction, the gap is inversely proportional to the width ($1/L$) of the nanoribbon. Conversely, along the armchair direction, the gap decreases proportionally to the square of the inverse width ($1/L^2$) (Sousa *et al.*, 2017a).

An important area of research in anisotropic materials is the electronic phase transition that these materials undergo when subjected to variations in their normal structural conditions. In phosphorene, studies have shown that the electronic phase transition (from semiconductor to semimetal) can occur with the application of stress, doping, and quantum confinement(Guan *et al.*, 2014; Xiang *et al.*, 2015; Dolui; Quek, 2015b; Hu; Dong, 2015; Fei *et al.*, 2015a; Sisakht *et al.*, 2016; Yuan *et al.*, 2016a; Kim *et al.*, 2017b; Baik *et al.*, 2015a). In 2015, Xiang *et al*. subjected a sample of approximately $2.5\times0.7\times0.1$ mm^3 of BP to a self-clamped cylinder piston hydrostatic pressure system, capable of applying pressures up to 2.4 GPa. The study demonstrated that the application of pressure significantly alters the transport properties and induces a semiconductor-semimetal phase transition in the phosphorene sample. At a pressure of approximately 1.2 GPa, a transition to the semimetal phase, known as the Lifshitz topological transition, was identified, characterized by low carrier density among other features. Furthermore, the presence of a linear dispersion in the bulk indicated the possible appearance of Dirac cones in a single layer of BP (Xiang *et al.*, 2015). Theoretical studies supported this direction. Fei *et al*. had previously simulated and discussed the band inversion and formation of Dirac cones in BP bulk under pressures greater than 0.6 GPa using first-principles and $k{\cdot}p$ methods (Fei *et al.*, 2015a). Theoretical works involving mechanical deformation also demonstrated a phase transition in the electronic properties of phosphorene through numerical methods. A model incorporating spin-orbit interaction using the tight-binding method was developed and explored by Sisakht *et al*. (Sisakht *et al.*, 2016). In this model, topological phase transitions in the band structure of bulk phosphorene and phosphorene nanoribbons were observed in the presence of applied tension. Similarly, another tight-binding model allowed for the exploration of the formation of quasi-Dirac cones and Landau levels for electrons in monolayer and bulk

phosphorene, facilitating a deeper study with an adjustable tight-binding Hamiltonian (Yuan *et al.*, 2016a).

Another way to induce an electronic phase transition in monolayer and few-layer BP is through doping. In this case, other materials are added to the surface of the phosphorene. In 2014, Guan *et al*., using BP allotropes, demonstrated through *ab initio* calculations that the semiconductor-to-semimetal phase transition is achievable by connecting different structural phases without a significant energy cost. This makes the assembly of heterostructures with metallic and semiconducting regions particularly valuable (Sisakht *et al.*, 2016). The doping of black phosphorus surface with potassium (K) atoms has been studied experimentally and theoretically using DFT (density functional theory) (Baik *et al.*, 2015a). This method allows for the control of band inversion with the density of K atoms.

After inversion, a Dirac semimetallic state emerges with different dispersions in the zigzag direction (quadratic dispersion) and armchair direction (linear dispersion). Near the Dirac point, the electronic structure exhibits linear dispersion in all directions and features such as the Berry phase and chiral pseudospin, indicating important spin-orbit interaction characteristics similar to graphene. The work by Kim *et al.* (2017b) provides an experimental analysis of the band structure of BP in the inverted band regime using ARPES on samples of black phosphorus doped with K and Rb (Rubidium). The pair of Dirac points, in the inverted band regime, move along the ky axis, and their separation varies with the dopant concentration. This provides support for a possible natural explanation for the different dispersions in the zigzag direction (quadratic dispersion) and armchair direction (linear dispersion). Unlike graphene, the Dirac points in the electronic topological phase transition are stable in BP. According to the research, these characteristics place black phosphorus in a research spectrum beyond 2D Dirac semimetals, as it exhibits exotic quantum transport properties.

1.1.4 Electronic transport properties

Years after the discovery of black phosphorus, studies focusing on its electronic properties were first explored by Keyes (1953). At that time, the measured value of electronic mobility for bulk BP was 350 cm^2/V.s for electrons and 220 cm^2/V.s for holes, with a temperature-dependent proportion given by approximately $T^{-\frac{3}{2}}$. In the following decades, subsequent measurements confirmed the important characteristic of high mobility in BP(Warschauer, 1963; Akahama *et al.*, 1983; Baba *et al.*, 1991).

With the exfoliation of few-layer BP and the observation of the energy gap dependence on the number of layers, new research focusing on its electronic properties has been conducted, further enhancing its prospects in nanoelectronic applications. Obtained values for charge carrier mobility in thin layers of black phosphorus ($\approx$ 10 nm) reached around 1,000 cm^2/V.s (Li *et al.*, 2014), and in the fabrication of FETs, they ranged from 250 to 600 cm^2/V.s ($\approx$ 5-15 nm) (Xia; Wang; Jia, 2014). Furthermore, it has been observed that these values are dependent on the thickness of BP. A theoretical study on FETs reported a hole mobility of approximately 286 cm^2/V.s at room-temperature for a layer thickness of approximately 10 μm (Liu; Neal, 2014). Recent fabrications of few-layer BP with high purity and nanoribbons (BPNR-FET, Black Phosphorus Nanoribbons - Field Effect Transistor) demonstrated hole mobilities of approximately 800 cm^2/V.s and approximately 862 cm^2/V.s, respectively (Tan *et al.*, 2018; Yang *et al.*, 2018). FETs made of few-layer BP encapsulated by h-BN in a vacuum exhibited ultrafast hole mobility of approximately 5,200 cm^2/V.s at room-temperature and 45,000 cm^2/V.s at cryogenic temperatures (Long *et al.*, 2016).

The conductivity of BP depends on its anisotropic characteristics. With different effective masses in different directions, the material's conductivity becomes dependent on the direction of charge carrier flow. Using the self-consistent pseudopotential method, the average effective masses for electrons ($0.22m_0$) and holes ($0.24m_0$) were determined (Liu *et al.*, 2015a). Density functional theory (DFT) simulations suggest adjusting the conductivity along a specific direction by tuning an angle. The conductivity of BP is predominantly due to positive charge carriers (holes), classifying it as a p-type conductivity with a positive Hall coefficient (Keyes, 1953; Warschauer, 1963).

1.1.5 External fields application

The application of electric and magnetic fields in BP sheets and PNRs is a very productive area in the theoretical (Chaudhary *et al.*, 2022; Carvalho *et al.*, 2016a; Akhtar *et al.*, 2017; Rudenko; Yuan; Katsnelson, 2015; Sousa *et al.*, 2017b; Lino *et al.*, 2017; Melo *et al.*, 2018; Jr; Katsnelson, 2015; Sousa *et al.*, 2016; Sousa *et al.*, 2017a; Cunha *et al.*, 2019; Wu *et al.*, 2015; Liu *et al.*, 2015b; Kumar *et al.*, 2016; Dolui; Quek, 2015a; Li *et al.*, 2017a) and experimental (Chaudhary *et al.*, 2022; Carvalho *et al.*, 2016a; Akhtar *et al.*, 2017; Liu *et al.*, 2015b; Kim *et al.*, 2017a; Li *et al.*, 2014; Ren *et al.*, 2021; Li *et al.*, 2018) research. It is well-known that applied an electric field in few-layer BP a Dirac-cone appears. Simulations using

DFT (Dolui; Quek, 2015b), tight-binding method (Yuan *et al.*, 2016a), and experimental results (Kim *et al.*, 2017a) confirm that the direct band gap of the material changes from semiconductor to metal with a critical value of an applied external electric field. The Dirac cone emerges along the Γ - Y direction for few-layer BP at values above a critical field strength **E**. Moreover, the field intensity also controls the position of the Dirac points and the Fermi-Dirac velocities, a characteristic similar to that of graphene (Dolui; Quek, 2015b). However, unlike graphene, the formation of Dirac points in phosphorene exhibits topological stability due to the protection by space-time inversion symmetry (Kim *et al.*, 2017a), which does not exist in graphene, giving it a significant advantage in applicability. According to Kim *et al*., this platform has the potential to serve as more than just a tool for exploring different 2D topological states. It can also provide a gateway to investigating a wide range of intriguing quantum transport phenomena, including quantum criticality, marginal Fermi-liquid behaviors (Isobe *et al.*, 2016; Cho; Moon, 2016), and uncommon Landau levels (Fei *et al.*, 2015b; Yuan *et al.*, 2016b). Figure 8 (a) (left) present the experimental band structure of BP in the band-inverted regime by means of angle-resolved photoemission spectroscopy (ARPES) combined with *in situ* surface doping, which is compared essencially an applied electric field and (right) schematic illustration for the band structure of BP under vertical electric field.

The application of magnetic fields to phosphorene induces an electronic phase transition and a spectrum of Landau levels equidistantly spaced proportional to $\sqrt{n\mathbf{B}}$, similar to graphene. The Hall conductivity of the system in the regime of quantum Hall effect was computed, and the quantization found for the gapped phase was $\sigma_{xy} \propto 2n$ and $\sigma_{xy} \propto 4(n+\frac{1}{2})$ for the semimetallic phase(Yuan *et al.*, 2016a). A theoretical continuum description of the applied magnetic field is provided by Pereira *etal*.. For a phosphorene bilayer, as shown in Figure 8 (b), the Landau level spectrum depends on the magnetic field and the bias applied to the on-site energy, simulating the effect of interlayer bias. When a bias is applied, it has the capability to effectively eliminate the electronic band gap in a material, causing a transition from an insulator to a metal. This transition occurs when the on-site energy difference reaches a critical value(Jr; Katsnelson, 2015).

1.1.6 Miscellaneous applications

Since the first possibility of applying phosphorene in electronic devices, an increasing number of studies have been refining our understanding of its properties and capabilities across

Figure 8 – (a) (left) present the experimental band structure of BP in the band-inverted regime by means of ARPES and (right) schematic illustration for the band structure of BP under vertical electric field (Kim *et al.*, 2017a). (b) Landau leves as a function of magnetic field with intralayer bias 0.74 eV.

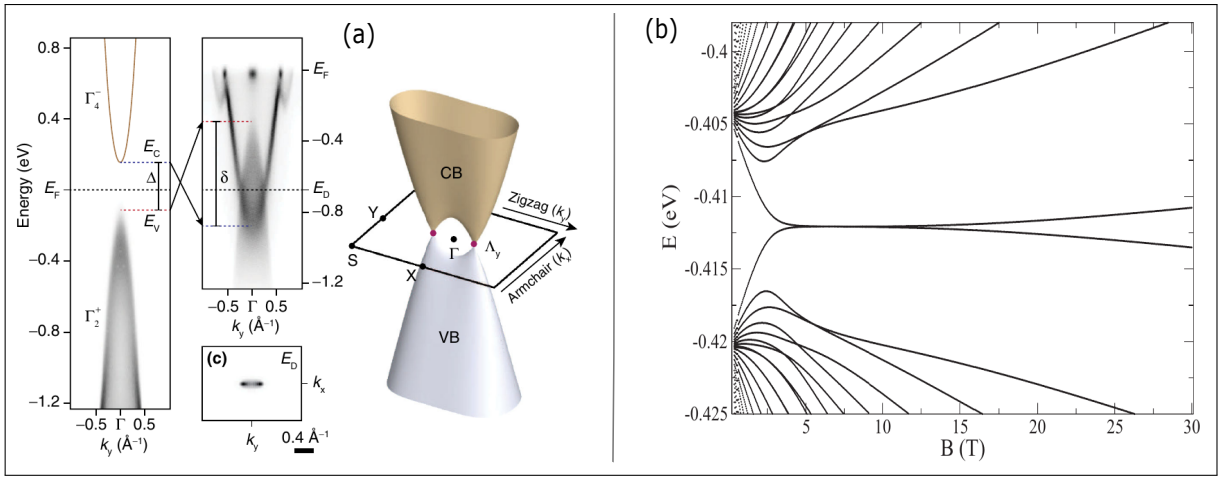

Source: Figure adapted from reference (Jr; Katsnelson, 2015)

various domains of technological development (Li *et al.*, 2014; Liu; Neal, 2014; Xia; Wang; Jia, 2014; Xu *et al.*, 2020; Wu *et al.*, 2021; Perello *et al.*, 2015; Na *et al.*, 2014b; Wang *et al.*, 2014; Chang *et al.*, 2017; Zhu *et al.*, 2015). The results guide advancements in its core functionalities and indicate a vast range of potential applications (Chaudhary *et al.*, 2022). Therefore, it can be said that it is evident that phosphorene plays a pivotal role in the advancement of cutting-edge materials, owing to its remarkable optical, electronic, and mechanical properties that showcase immense potential across numerous fields, including high-speed electronics, optoelectronics, sensors, and biomedicine. However, research exploring the properties and applications of phosphorene is still in its nascent stage, and we will still have a long way to go before reaching greater goals such as replacing other materials in industrial production (Chaudhary *et al.*, 2022).

With all, it is possible to find works on electronic devices BP-based , such as the FET (Field-effect Transistor) . A FET is an electronic device made of semiconductor material that plays a crucial role in amplifying electrical signals. It serves as the fundamental building block in contemporary digital technology, enabling the functioning of various electronic devices. Table 1 shows the results of some of the primary studies on BP-based FETs. The significant and diverse results of these studies indicate a promising future for devices based on phosphorene and, as a result, a path toward its application in integrated circuits. For digital transistors to operate effectively, an optimal semiconducting material should demonstrate specific characteristics. These include a substantial ON/OFF ratio to facilitate efficient switching, high carrier mobility to ensure swift operation, and exceptional conductivity coupled with low OFF-

state conductance to minimize power consumption. Worth highlighting the work of Xu *et al*. (Xu *et al.*, 2020), that recently there have been successful advancements in the fabrication of few-layer phosphorene-based FETs using a gas-phase growth method. The FET devices that were fabricated exhibited a layer thickness within the range of 5 to 10 nanometers. Notably, these devices demonstrated impressive Hall and field-effect mobility values exceeding 1400 and 1000 $cm^2\ V^{-1}s^{-1}$, respectively, at room temperature.

Table 1 – BP-based FETs, including layer thickness, performance parameters, and operating temperature (RT = Room-temperature).

Material/thickness (nm)	Mobility$(cm^2V^{-1}s^{-1})$	ON/OFF ratio A	Temperature	Ref.
BP/10	984	10^5	RT	(Li *et al.*, 2014)
BP/10	286	10^4	RT	(Liu; Neal, 2014)
BP/5	205	10^5	RT	(Xia; Wang; Jia, 2014)
BP/8	1250	10^8	10 K	(Xu *et al.*, 2020)
BP/5	213	10^3	295 K	(Wu *et al.*, 2021)
BP/3	275	10^5	RT	(Perello *et al.*, 2015)
BP/18.7	170	10^2	RT	(Na *et al.*, 2014b)
BP/8.5	400	10^3	RT	(Wang *et al.*, 2014)
BP/6.7	227	10^4	RT	(Chang *et al.*, 2017)
BP/15	310	10^4	RT	(Zhu *et al.*, 2015)

Source: Table adapted from (Chaudhary *et al.*, 2022)

Despite the high electronic mobility observed in BP bulk, the mobility values of few-layer phosphorene are relatively modest in comparison. One possible solution to address the issue of low mobility in very thin or monolayer phosphorene is to employ an ultra-small device geometry, specifically by reducing the channel length to the nanoscale. This approach has the potential to enable ballistic quantum transport, overcoming the limitations of low mobility. In a recent study conducted by Miao, *et al* (Miao *et al.*, 2015), they successfully fabricated FETs using a few layers of BP with a channel length of 20 nm. Nevertheless, the development of high-frequency BP-based FETs is still in its early stages. Currently, experimental results have only demonstrated a frequency response up to f_T = 17.5 GHz and f_{max} = 14.5 GHz. These results were achieved using a relatively short channel length of 250 nanometers, as reported in a study (Zhu *et al.*, 2016).

BP has gained significant attention as a versatile material in the field of optoelectronics, owing to its appealing properties. The ability to tune the bandgap, coupled with optical anisotropy and notable carrier mobility, makes few-layer phosphorene well-suited for applications in light sensing and optical imaging. Their unique characteristics enable them to play a vital role in various optoelectronic devices. Furthermore, the fascinating properties exhibited by

phosphorene, including controllable bandgap, ambipolar charge transport, high mobility, and flexibility, make them highly promising for integration into diverse optoelectronic components. These materials are poised to play a significant role in advancing technologies such as solar cells, photodetectors, and light-emitting diodes (LEDs) . Phosphorene holds great promise as an effective material for solar cells, primarily due to its ability to efficiently absorb a wide range of light wavelengths. The broadband light-absorbing properties of phosphorene make it a compelling candidate for harnessing solar energy in photovoltaic applications. Phosphorene has established itself as a noteworthy player in the field of chemical and biological sensors. Its distinct attributes and features make it a valuable candidate for sensing applications, enabling the creation of advanced sensors with enhanced sensitivity and selectivity. The unique properties of phosphorene open up new possibilities for the detection and analysis of a wide range of chemical and biological substances.

It is worth mentioning that even with many qualities, phosphorene still faces some problems that limit it to a great performance. In addition to the quality and thickness of the thin film semiconductor, contact resistance plays a significant role in influencing the performance of electronic devices. Specifically, the presence of high contact resistance, primarily caused by Schottky barrier formation and contamination at the metal-BP interface, poses considerable challenges in the practical utilization of BP-based devices for various applications. Phosphorene's environmental stability represents a significant constraint on its potential applications in modern technologies. The problem of phosphorene degradation is a critical issue that requires substantial attention and resolution before its widespread use for future applications.

1.2 Defects in 2D crystals

Crystalline structures are defined at a microscopic level as those in which their atoms or ions are grouped in a periodic lattice (Ashcroft; Mermin, 2022). On a macroscopic scale, it is more common to encounter structures in a polycrystalline state, where what is observed are vast quantities of crystal fragments with a large number of atoms or ions arranged periodically. Experimental observation of these structures indicates that perfect lattices are uncommon in a real crystal. One of the most important kinds of defects in the crystal systems is the vacancies defect. Therefore, in this section, we approach the vacancy defects in 2D crystals.

1.2.1 Vacancies defects in 2D crystals

During experimental processes of sample preparation of structures made out of 2D materials, which includes realizations/synthesis itself and transfer/deposition to certain appropriate substrates, always noted defects, such as vacancies, adatoms, edges disorders, grain boundaries, and substitutional or interstitial impurities, Figure 9, (a)-(e), respectively (Addou; Colombo, 2022; Bertoldo *et al.*, 2022; Wu; Ni, 2017; Ahmad *et al.*, 2021; Jiang *et al.*, 2019; Banhart *et al.*, 2011; Araujo *et al.*, 2012). It was well-known for three-dimensional crystals that the presence of structural defects in the crystallographic lattice modifies the optoelectronics and transport properties of the system. Very soon after the experimental realization of graphene (the first obtained 2D material) (Novoselov *et al.*, 2004), a great interest to understand how graphene

Figure 9 – Defects in 2D crystals: (a) vacancies, (b) adatoms, (c) edges disorders, (d) grain boundaries, and (e) substitutional or interstitial impurities.

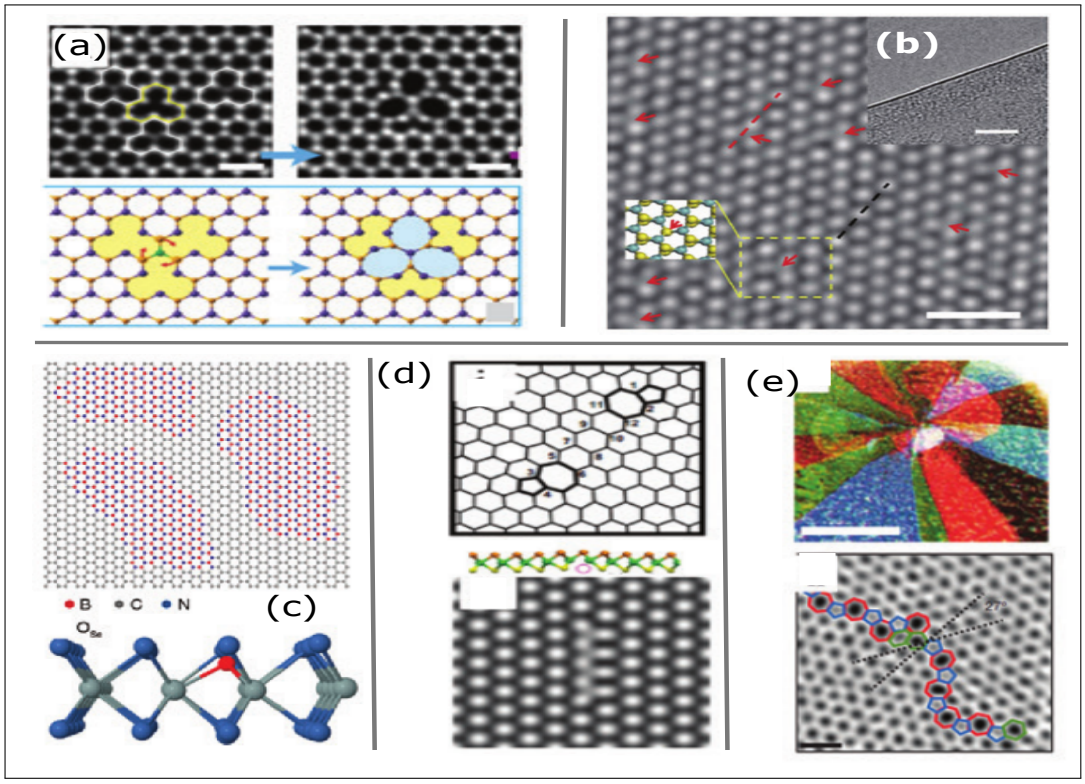

Source: Figure adapted from references (Addou; Colombo, 2022; Bertoldo *et al.*, 2022; Wu; Ni, 2017; Ahmad *et al.*, 2021; Jiang *et al.*, 2019; Banhart *et al.*, 2011; Araujo *et al.*, 2012).

physics is modified due to vacancy disorders, originating from removing carbon atoms, has been the subject of substantial theoretical and experimental investigations. For instance, owing to the defects in the case of few-layer graphene, it was observed electronic mobility reduction (McCreary *et al.*, 2010; Costa *et al.*, 2017), changes in the band structure (Banhart *et al.*, 2011;

Miranda *et al.*, 2022; Kishimoto; Okada, 2016), the possibility of the emergence of magnetic ordering (Brey *et al.*, 2007; Esquinazi *et al.*, 2003; Yazyev; Helm, 2007; Palacios; Ynduráin, 2012; Chen *et al.*, 2014; Nakhmedov *et al.*, 2019; Francis *et al.*, 2015; Ma *et al.*, 2004), and the emergence of zero energy modes, which are localized states around the missing carbon atoms being energetically placed around the Fermi level (Kishimoto; Okada, 2016; Ovdat *et al.*, 2020; Kotakoski *et al.*, 2011; Lee *et al.*, 2005; Palacios *et al.*, 2008; El-Barbary *et al.*, 2003; Hahn; Kang, 1999).

1.2.2 Vacancies defects in phosphorene

Similarly, soon after the phosphorene exfoliation, there was a growing interest in studying defective few-layer BP structures, including intrinsic or extrinsic defects, as well as neutral or charged defects, in order to design and functionalize them for future applications (Li *et al.*, 2015; Zhang; Wu; Yang, 2016; Lei *et al.*, 2017b; Lei *et al.*, 2017a; Kistanov *et al.*, 2016; Smotlacha; Pincak, 2018; Sun *et al.*, 2018; Arra; Babar; Kabir, 2019; Li; Peeters, 2018; Dai *et al.*, 2017; Kiraly *et al.*, 2017; Harsh *et al.*, 2022; Huang *et al.*, 2022; He *et al.*, 2019; Zhan *et al.*, 2019; Li *et al.*, 2022; Aghajanian; Mostofi; Lischner, 2022; Fang *et al.*, 2022; Rijal *et al.*, 2021; Rezaei *et al.*, 2021; Gupta; Periasamy; Narayanan, 2021; Yao *et al.*, 2020; Pei *et al.*, 2020; Kundu; Naik; Jain, 2020; Wang *et al.*, 2015; Kripalani *et al.*, 2019; Shah *et al.*, 2019; Cai *et al.*, 2019; Amini *et al.*, 2019a; Amini *et al.*, 2019b; Riffle *et al.*, 2018; Cai *et al.*, 2016; Gaberle *et al.*, 2018; Hu *et al.*, 2015; Farooq *et al.*, 2015). For instance, vacancies and antidots have been induced in the BP lattice with intention of obtaining tunable optoelectronic properties making this material suitable for applications in LEDs, photocells and photodetectors (Lei *et al.*, 2017a). The experimental study reported in Kiraly *et al.* (2017) observed, via a combination of low-temperature scanning tunneling microscopy/spectroscopy (STM/STS), that the spatial distributions of the wave functions are localized around the atomic vacancies on the surface of bulk BP and they exhibit strong anisotropy, Figure 10 (a). Reference Fang *et al.* (2022) also experimentally demonstrated by means of STM that ionization of single vacancy into negatively charged single vacancy leads to the passivation of dangling bonds and thus the quenching of in-gap states, where the single vacancy exhibits a strong and symmetric Friedel oscillation pattern, while the charged single vacancy shows an asymmetric pattern, Figure 10 (b). From the theoretical point of view, intrinsic defects in the BP lattice structure, such as monovacancies or divacancies, have been investigated for the cases of infinite few-layer BP lattices (Li *et al.*, 2015;

Zhang; Wu; Yang, 2016; Kistanov *et al.*, 2016; Dai *et al.*, 2017; Kundu; Naik; Jain, 2020; Wang *et al.*, 2015; Kripalani *et al.*, 2019; Cai *et al.*, 2019; Hu *et al.*, 2015; Farooq *et al.*, 2015) (Figure 10 (c)), by considering periodic boundary conditions of a large supercell, and of nanostructures, such as nanoribbons (Smotlacha; Pincak, 2018; Sun *et al.*, 2018; Li; Peeters, 2018; Amini *et al.*, 2019b; Rezaei *et al.*, 2021; Amini *et al.*, 2019a). For the BP nanoribbons case, the results indicated a strong structural dependence on the vacancy position with respect to its proximity to the nanoribbon edges(Smotlacha; Pincak, 2018; Sun *et al.*, 2018) and the vacancy type (Li; Peeters, 2018; Amini *et al.*, 2019b) (Figure 9 (d)).

Despite the vast literature regarding different theoretical and experimental research on defective phosphorene (Li *et al.*, 2015; Zhang; Wu; Yang, 2016; Lei *et al.*, 2017b; Lei *et al.*, 2017a; Kistanov *et al.*, 2016; Smotlacha; Pincak, 2018; Sun *et al.*, 2018; Arra; Babar; Kabir, 2019; Li; Peeters, 2018; Dai *et al.*, 2017; Kiraly *et al.*, 2017; Harsh *et al.*, 2022; Huang *et al.*, 2022; He *et al.*, 2019; Zhan *et al.*, 2019; Li *et al.*, 2022; Aghajanian; Mostofi; Lischner, 2022; Fang *et al.*, 2022; Rijal *et al.*, 2021; Rezaei *et al.*, 2021; Gupta; Periasamy; Narayanan, 2021; Yao *et al.*, 2020; Pei *et al.*, 2020; Kundu; Naik; Jain, 2020; Wang *et al.*, 2015; Kripalani *et al.*, 2019; Shah *et al.*, 2019; Cai *et al.*, 2019; Amini *et al.*, 2019a; Amini *et al.*, 2019b; Riffle *et al.*, 2018; Cai *et al.*, 2016; Gaberle *et al.*, 2018; Hu *et al.*, 2015; Farooq *et al.*, 2015) and the several works using different theoretical models to present predictions about the main phosphorene properties, ranging from *ab initio* calculations (Tran *et al.*, 2014; Jing; Park, 2014; Fei; Yang, 2014; Wei; Peng, 2014; Qin *et al.*, 2015; Shriber *et al.*, 2018) to semi-empirical methods, as tight-binding model (Takao; Asahina; Morita, 1981; Rudenko; Katsnelson, 2014a; Rudenko; Yuan; Katsnelson, 2015; Sousa *et al.*, 2017b; Lino *et al.*, 2017; Melo *et al.*, 2018; Jr; Katsnelson, 2015; Sousa *et al.*, 2016; Sousa *et al.*, 2017a) and continuum approach (Jr; Katsnelson, 2015; Sousa *et al.*, 2016; Sousa *et al.*, 2017a; Cunha *et al.*, 2019), to our knowledge, there is a lack of a systematic, appropriate, and carefully taken study on the band unfolding process to deal with large supercells by considering multiple vacancies in multilayer phosphorene and the obtention of their non-duplicated band structures in the reciprocal space in the presence of point defects.

Figure 10 – (a) Observation experimental, via a combination of low-temperature of that the spatial distributions of the wave functions are localized around the atomic vacancies on the surface of bulk BP and they exhibit strong anisotropy. (b) Demonstration by means of STM that ionization of single vacancy into negatively charged single vacancy leads to the passivation of dangling bonds. The single vacancy exhibits a strong and symmetric Friedel oscillation pattern, while the charged single vacancy shows an asymmetric pattern. (c) Schematic illustrations and band structure and wave function at Γ point of a single vacancy. (d) DOS and conductance of defective PNRs with random vacancies for different vacancy concentrations P.

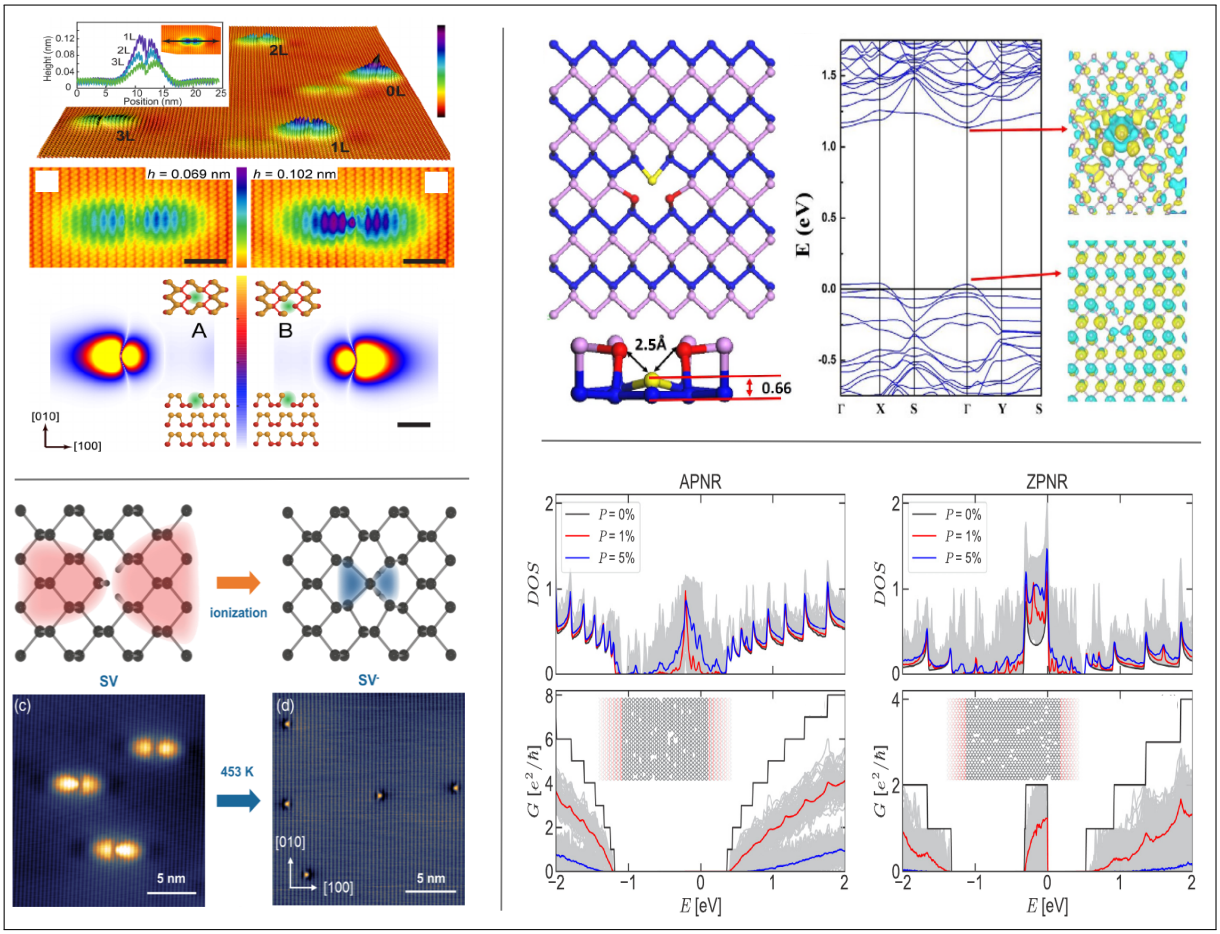

Source: Figure adapted from references (Kiraly *et al.*, 2017; Fang *et al.*, 2022; Farooq *et al.*, 2015; Li; Peeters, 2018).

2 TIGHT-BINDING MODEL TO PHOSPHORENE MULTILAYER

In this chapter, we present the general tight-binding method in the first section. In the second section, we present the tight-binding model to multilayer phosphorene with 15 hoppings parameters (Rudenko; Katsnelson, 2014a). A tight-binding model to multilayer phosphorene with 3 hoppings parameters is shown in the third section. Finally, the continuum approximation to multilayer phosphorene is presented in the fourth section.

2.1 Tight-binding model

The Linear Combination of Atomic Orbitals (LCAO) method is a widely used semi-empirical approach in the calculation of band structure in solid-state physics. The model involves considering a crystalline system where the electron experiences a periodic potential from the lattice, denoted as $V(\vec{r}i+\vec{r}) = V(\vec{r})$, where $\vec{r}i$ represents the translational periodicity vector of the i-th unit cell of the crystal. Consequently, the wave function of the lattice can be expressed as a linear combination of the wave functions of the unit cell. Thus,

$$\Psi_{cristal}(\vec{r}) = \sum_{i,\alpha} a_{i,\alpha}(\vec{r})\psi_{i,\alpha}(\vec{r}), \tag{2.1}$$

where the summation over i occurs overall unit cells of the lattice, and over α it occurs overall atomic orbitals within each unit cell. We should expect that the probability density for the electron in such a system also follows this periodicity, that is, $|\Psi(\vec{r}+\vec{r}i)|^2 = |\Psi(\vec{r})|^2$. Due to this, according to Bloch's theorem, the wave function $\psi i,\alpha(\vec{r})$, which represents the electron in the lattice basis of the unit cell, is a Bloch function that can be written as

$$\psi_{i,\alpha}(\vec{r}) = \frac{1}{\sqrt{N}}\sum_{\vec{r}_i} e^{i\vec{k}\cdot\vec{r}_i}\phi(\vec{r}-\vec{r}_i). \tag{2.2}$$

In general, the unit cells have more than one atom with more than one orbital and this way we can write $\Psi_{cristal}(\vec{r})$ as

$$\Psi_{cristal}(\vec{r}) = \frac{1}{\sqrt{N}}\sum_{i,j,\alpha} a_{i,j,\alpha}e^{i\vec{k}\cdot\vec{r}_i}e^{i\vec{k}\cdot\vec{\tau}_j}\phi_\alpha(\vec{r}-\vec{r}_i-\vec{\tau}_j), \tag{2.3}$$

where τ_j represents the position of i-th atom into uint cell. Applying $\langle\psi_{i,\alpha}(\vec{r})|$ on the two sides of the Schröedinger equation

$$H\left|\Psi_{cristal}(\vec{r})\right\rangle = E\left|\Psi_{cristal}(\vec{r})\right\rangle, \tag{2.4}$$

we will get an alternative form of the equation due to the orthogonality of the Block function, being rewritten as follows

$$\sum_l a_l[\langle\psi_l(\vec{r})|H|\psi_{l'}(\vec{r})\rangle - E\langle\psi_l(\vec{r})|\psi_{l'}(\vec{r})\rangle] = 0, \tag{2.5}$$

where we have generalized the indices $l = \{i, j, \alpha\}$. We can still define

$$H_{l,l'} = \langle\psi_l(\vec{r})|H|\psi_{l'}(\vec{r})\rangle, \tag{2.6}$$

and

$$S_{l,l'} = \langle\psi_l(\vec{r})|\psi_{l'}(\vec{r})\rangle, \tag{2.7}$$

that we call $S_{l,l'}$ of the matrix of *overlap*. Replacing the equations 2.6 and 2.7 in 2.5, we can verify now that the problem is reduced to resolve of the secular equation given by

$$\sum_l a_l[H_{l,l'} - ES_{l,l'}] = 0, \tag{2.8}$$

where the solutions are established by resolving

$$det(H_{l,l'} - ES_{l,l'}) = 0. \tag{2.9}$$

The solution then gives us the eigenenergy and eigenvalues of the wanted system.

2.2 Tight-binding model to multilayer phophorene: 15 hoppings

The band structure of multilayer phosphorene can be calculated using the tight-binding model, as written in the previous section, which consists of writing the charge carrier wavefunction as a linear combination of atomic orbitals (Sousa *et al.*, 2017a). This approach is a semi-empirical method widely used in calculating the band structure in solid-state physics (Lima *et al.*, 2022). The model consists of considering a crystalline system where the electron feels a periodic lattice potential $V(\mathbf{r}+\mathbf{r}_i) = V(\mathbf{r})$, where $\mathbf{r}_i$ represents the translational periodicity vector of the i-th unit cell of the crystal. Based on the Bloch theorem, the probability density for the electron in such a system also obeys such a periodicity, i.e., $|\Psi(\mathbf{r}+\mathbf{r}_i)|^2 = |\Psi(\mathbf{r})|^2$. In this approximation, the Hamiltonian $\hat{H}$, considering that charge carriers can hop to the neighbors of a phosphorus atom, has the form in the second quantization language such as

$$\hat{H} = \sum_i(\varepsilon_i + V_i)c_i^\dagger c_i + \sum_{i\neq j}\tau_{ij}^{||}c_i^\dagger c_j + \sum_{i\neq j}\tau_{ij}^{\perp}c_i^\dagger c_j, \tag{2.10}$$

where $i = \{\mathbf{R}_i, \alpha, \nu\}$ represents the generalized index for the orbital ν of the atomic species α at the atomic site $\mathbf{R}_i$. Here, for the N-layer phosphorene case, one considers just a single-orbital per atom with all atoms of the same species (P), such that the sums run over all sites, a prior, of the crystal lattice, being c_i ($c_i^\dagger$) the operator that annihilates (creates) an electron at the site i with on-site energy ε_i, and $\tau_{ij}^{||}$ ($\tau_{ij}^{\perp}$) is the intralayer (interlayer) hopping parameter between the i-th and j-th sites. Since all atoms are identical, the on-site energies only shift the Fermi energy. Therefore, without loss of generality, we adopted here $\varepsilon_i = 0$. The second and third terms of Eq.(2.10) correspond to the intralayer and interlayer interactions between sites i and j in the same or different layers, respectively. These sums run over 10 intralayer and 5 interlayer hoppings, as shown in Figure 11, with hopping parameters and lattice constants being the ones reported by Rudenko, Yuan & Katsnelson (2015), which takes advantage of the predominance of p_z characteristic near the band edges of multilayer phosphorene to construct a single-orbital tight-binding parameterization with GW_0 quality.

Figure 11 – Sketches of the (a) 10-intralayer and (b) five-interlayer hopping parameters.

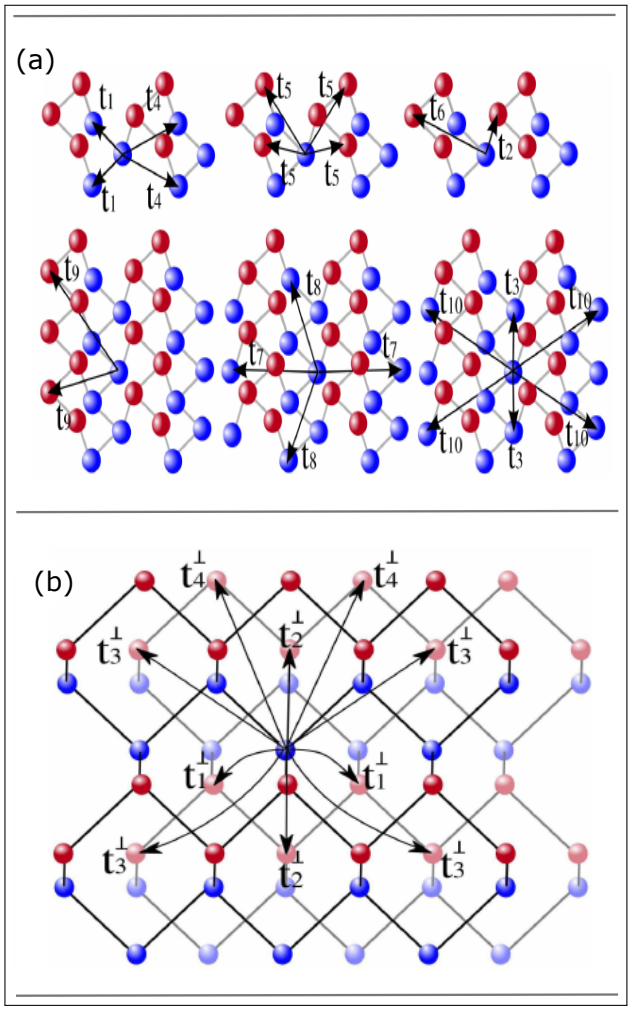

Source: Figure adapted from reference (Sousa *et al.*, 2017a).

In this model, the values in Table 2 are taken for the intralayer and interlayer hopping parameters, as depicted in Figure 11(a) and 11(b), respectively.

Table 2 – Intralayer and Interlayer hopping parameters used for tight-binding calculation for phosphorene multilayer and distance (in Å) between the corresponding interacting lattice sites.

Intralayer	$t^{\parallel}$(eV)	distance(Å)
t_1	-1.482	2.22
t_2	3.729	2.24
t_3	-0.252	3.31
t_4	-0.071	3.34
t_5	-0.019	3.47
t_6	0.186	4.23
t_7	-0.063	4.37
t_8	0.101	5.18
t_9	-0.042	5.37
t_{10}	0.073	5.49
Interlayer	$t^{\perp}$ (eV)	distance (Å)
t_1	0.524	3.60
t_2	0.180	3.81
t_3	-0.123	5.05
t_4	-0.168	5.08
t_5	0.005	5.44

Source: Table elaborated by the author (2023).

Concerning the theoretical obtaining procedure of the hopping parameters, it is worth mentioning that, in general, the band structure is initially calculated by means of first-principles methods, and then a search is done for the hopping parameters that best fit the energy bands obtained by the tight-binding method to those obtained by the first-principles calculations (Araujo *et al.*, 2012), in a similar way as done in the Wannierization procedure of density functional theory (Garrity; Choudhary, 2021). For instance for multilayer BP, a study performed a similar procedure based on first-principles calculations and was reported in Rudenko & Katsnelson (2014a) the hopping parameters for modeling BP structures by using 5 intralayer hoppings whereas in 2015 reported in Rudenko, Yuan & Katsnelson (2015) a more accurate model with 10 intralayer hoppings that fit more properly the BP band structure obtained via first-principle calculations. Here, our results for energy values by the tight-binding model were calculated numerically by code written in MATLAB language (Inc., 2022) and also we have used the *Pybinding* Python package (Moldovan *et al.*, 2017).

2.3 Tight-binding model to multilayer phophorene: 3 hoppings

The Hamiltonian to multilayer phosphorene considering just three hoppings is the same as the Eq. 2.10. A minimal tight-binding model, that captures the main features of the monolayer and bilayer BP band structures, for instance, the anisotropy of the bands and lowest band curvatures, takes into account the two largest intralayer hopping parameters, see t_1 and t_2 in Fig. 12. Such a minimal tight-binding model has been successfully used in some previous works (Li *et al.*, 2017b; Sisakht *et al.*, 2015) in the literature to describe the electronic and transport properties of monolayer and bilayer phosphorene quantum dots and phosphorene nanoribbons and it is also the one adopted here. Therefore, the second summation in the right-hand side of Eq. 2.10 runs over 2 intralayer hoppings. The third summation related to the interlayer coupling effect is assumed here to run just over 1 hopping. Within a minimal tight-binding

Figure 12 – Sketches of the structure with 2-intralayer and 1-interlayer hopping parameters in the minimal model.

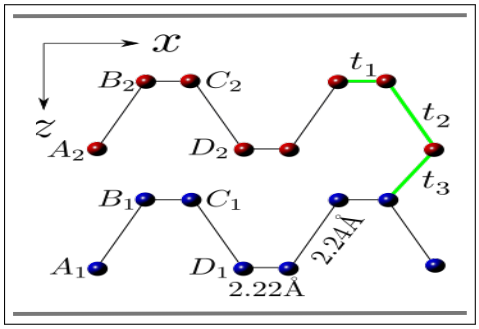

Source: Figure adapted from refence (Sousa *et al.*, 2017a).

model for multilayer systems, at least one interlayer coupling should be considered, in view that the coupling of BP multilayers can be approximately a quasi-1D tight-binding model along z-direction, where each phosphorene layer is associated with an atomic site and consequently the interlayer coupling energy is linked to the hopping parameter of the 1D z-chain. V_i, in turn, is the on-site potential used to introduce the effect of the external electric field.

2.4 Continuum approximation to multilayer phophorene

So far, we have been dealing with the tight-binding method purely numerically, where we use codes and computational language packages to calculate its properties, such as band structure and electronic transport. However, it has been possible to derive semi-analytical relationships within the continuum approximation for the eigenenergies and eigenvectors of a

Table 3 – Intralayer and Interlayer hopping parameters used for the minimal tight-binding calculation for phosphorene monolayer and bilayer and distance (in Å) between the corresponding interacting lattice sites.

Intralayer	$t^{\parallel}$(eV)	distance(Å)
t_1	-1.210	2.22
t_2	3.180	2.24
Interlayer	$t^{\perp}$ (eV)	distance (Å)
t_3	0.220	3.21

Source: Table elaborated by the author (2023).

multilayer phosphorene system. Initially, based in Rudenko, Yuan & Katsnelson (2015) tight-binding model, which we have been using for our numerical calculations, Milton et al. managed to obtain the eigenvalues and eigenvectors semi-analytically by considering lattice symmetries and appropriate boundary conditions. As a result, unitary transformations were performed that simplified the Hamiltonian, allowing for the determination of eigenenergies and eigenvalues for a monolayer of phosphorene. Sousa *et al.* (2017a), considering the boundary conditions and sublattice symmetries of the system, generalize the monolayer Hamiltonian to an n-layer phosphorene system, achieving excellent results for low-energy values near the Γ point. While they obtained a relation for the wave function when the number of layers tends to infinity, we will here generalize the energy eigenstates for the n-layer Hamiltonian according to the model of reference Jr & Katsnelson (2015). The n-layer Hamiltonian is:

$$\mathscr{H}^n = \begin{pmatrix} u_0^n + \eta_x^n k_x^2 + \eta_y^n k_y^2 & \delta^n + \gamma_x^n k_x^2 + \gamma_y^n k_y^2 + iX^n k_y \\ \delta^n + \gamma_x^n k_x^2 + \gamma_y^n k_y^2 + iX^n k_y & u_0^n + \eta_x^n k_x^2 + \eta_y^n k_y^2 \end{pmatrix} \tag{2.11}$$

By diagonalizing $\mathscr{H}^n$, we find the energy of the n-layer system, given by

$$E^n = u_0^n + \eta_x^n k_x^2 + \eta_y^n k_y^2 \pm \sqrt{(\delta^n + \gamma_x^n k_x^2 + \gamma_y^n k_y^2)^2 + (iX^n k_y)^2} \tag{2.12}$$

where the symbols $\pm$ indicate the conduction band (+) and valence band (-), and with all constant parameters specific ($u_0^n, \delta^n, \eta_x^n, \eta_y^n, \gamma_x^n, \gamma_y^n$ and X^n) to the generalized multilayer phosphorene as described in Sousa *et al.* (2017a). Following the steps outlined in Jr & Katsnelson (2015) it is also possible to find the generalized eigenstates by rewriting the Hamiltonian as

$$\mathscr{H}^n = \begin{pmatrix} \varepsilon_1^n & \varepsilon_2^n e^{i\theta_k^n} \\ \varepsilon_2^n e^{i\theta_k^n} & \varepsilon_1^n \end{pmatrix} \tag{2.13}$$

where

$$\varepsilon_1^n = \frac{f_+^n + f_-^n}{2}, \varepsilon_2^n = \sqrt{\left(\frac{f_+^n - f_-^n}{2}\right)^2 + (X^n k_y)^2} \tag{2.14}$$

and

$$\theta_k^n = tan^{-1}\left(\frac{2X^n k_y}{f_+^n - f_-^n}\right), \tag{2.15}$$

where we defined

$$f_\pm^n = (u_0^n \pm \delta^n) + (\eta_x^n \pm \gamma_x^n)k_x^2 + (\eta_y^n \pm \gamma_y^n)k_y^2 \tag{2.16}$$

Thereby, considering the generalized parameters, the Schrödinger equation provides the following equations

$$\varepsilon_1^n \phi_1^n + \varepsilon_2^n e^{i\theta_k^n}\phi_2^n = E_k^n \phi_1^n \qquad \textit{and} \qquad \varepsilon_2^n e^{-i\theta_k^n}\phi_1^n + \varepsilon_2^n \phi_2^n = E^n{}_k \phi_2^n, \tag{2.17}$$

where $\phi_1^n = \phi_A^n + \phi_D^n$ and $\phi_2^n = \phi_B^n + \phi_C^n$ are the spinor components

$$\psi_k^n = \begin{pmatrix} \phi_1^n \\ \phi_2^n \end{pmatrix} \tag{2.18}$$

applied in the Schrödinger equation ($H_k\psi_k = E_k\psi_k$) and specified in the work of Duarte *et al*. (Sousa *et al.*, 2017a). The solution of the Eq. 2.17 is

$$\psi_k^n = \frac{1}{\sqrt{2}}\begin{pmatrix} 1 \\ \lambda e^{i\theta_k^n} \end{pmatrix}, \tag{2.19}$$

where $\lambda = \pm$, with the positive (negative) signs corresponding to electrons (holes) on the conduction (valence) band. Therefore, it is possible to find the generalized eigenstates to the Hamiltonian as in Jr & Katsnelson (2015). We will use these results in chapter 9 in order to obtain the dielectric function semi-analytically. It is worth mentioning that the discussion about the wave function found here deserves care since the Hamiltonian for n-layers is decoupled, the eigenstates for each layer are orthogonal functions.

3 BAND UNFOLDING THEORY

The study of electronic properties in materials like phosphorene requires a modeling approach that considers the effects of defects such as atom vacancies, doping, and others, in a larger parameter network than the lattice parameters of the primitive cell. The supercell approach is widely used for such problems, and the effects of impurities are not ignored in this context. However, the results from the pure and simple supercell model do not provide us with suitable conditions for conducting thorough investigations. When examining the band structure of a supercell with many atoms, we are faced with a complex set of bands that is difficult to analyze. The band unfolding (BU) theory allows us to analyze the band structure by using the supercell approach to unfold the bands of the supercell onto the basis of states of the primitive cell. Recent studies conducted using band unfolding theory have demonstrated how electronic properties of crystals can be altered when an imperfect crystal lattice is considered (Zang; Wang, 2011; Medeiros *et al.*, 2014; Cui *et al.*, 2015; Maspero *et al.*, 2016; Popescu; Zunger, 2012; Popescu; Zunger, 2010). The foundations of the theory are well-defined in the literature (Boykin; G., 2005; Boykin *et al.*, 2007; Boykin *et al.*, 2016; Babar *et al.*, 2018; Ku *et al.*, 2010). In this chapter, we will present the methodology of BU theory and investigate how the influence of impurities can affect the effective electronic structure of a material.

3.1 Supercell parameters

Here, we will define the lattice parameters that we will use to construct the grid of the supercell in which we will simulate the system with the characteristics of the modified crystal. The real-space lattice vectors in the Brillouin zone of the primitive cell and the supercell are denoted by $\mathbf{a}i$ and $\mathbf{A}i$, where $i = 1,2,3$. Similarly, the reciprocal lattice vectors in the reciprocal space of the Brillouin zone of the primitive cell and the supercell are defined as $\mathbf{b}i$ and $\mathbf{B}i$, where $i = 1,2,3$. In general, in real space, a set of basis vectors relate to each other through an invertible 3×3 matrix $\mathbf{M}$ ($\mathbf{A}i = \mathbf{M} \cdot \mathbf{a}i$). We consider that the vectors used in this relation are collinear, which allows us to write the relationship between the vectors of the primitive cell and the supercell as $\mathbf{A}i = Ni \cdot \mathbf{a}i$ in real space and $\mathbf{B}i = \frac{1}{N_i} \cdot \mathbf{b}i$ in reciprocal space, where Ni is the diagonal of $\mathbf{M}$. The relationship between the vectors in the real space and reciprocal space bases is given by $\mathbf{a}_i.\mathbf{b}_j = 2\pi\delta_{ij}$ e $\mathbf{A}_i.\mathbf{B}_j = 2\pi\delta_{ij}$ (Boykin *et al.*, 2007). The number of primitive cells contained in the supercell is given by $N_{cp} = \frac{\Omega_{ZBS}}{\Omega_{ZBP}}$, where Ω_{ZBP} (Ω_{ZBS}) is the volume of

the Brillouin zone of the primitive cell (supercell). Figure 13 illustrates the arrangement of the overall atom distribution in a 2D system in real space and the lattice points in phase space.

Figure 13 – (a) Grid points in real space for a crystal. A crystal composed of Nsc supercells with base vector A has the lattice vector $\vec{R}_s$ that locates the s-th supercell containing i primitive cells, located by the vector $\vec{r}_i$. (b) Phase space with the respective lattice vectors K (supercell) and k (primitive cell).

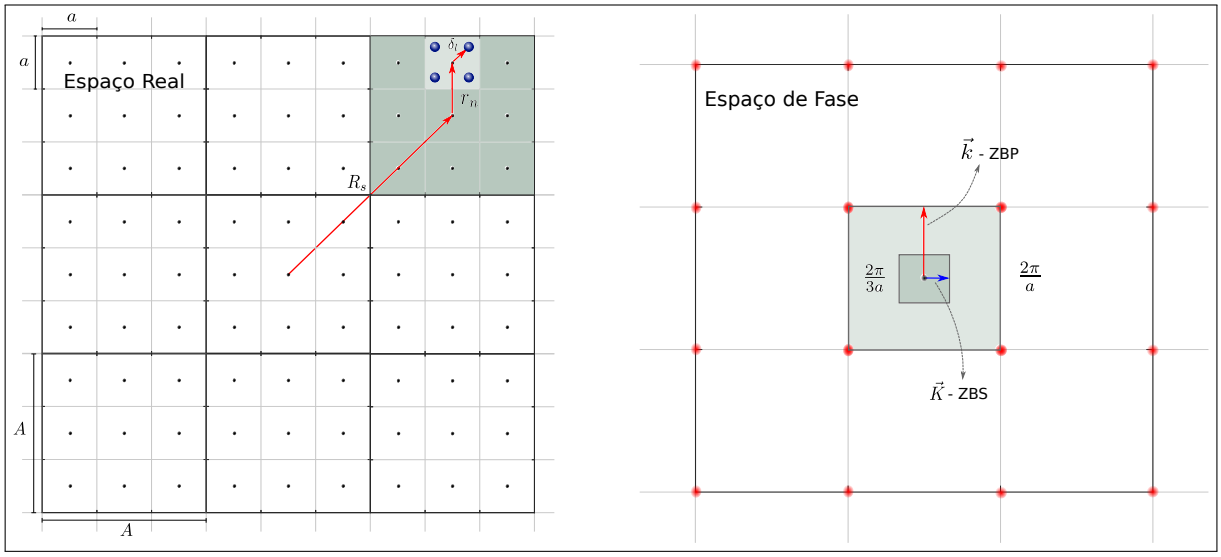

Source: Figure elaborated by the author (2023).

3.2 Spectral weight

The BU method essentially involves calculating the band structure of a supercell in the Brillouin zone of the supercell and projecting the energetic contributions defined by the density of states (spectral weight) that coincide with the band structure of the primitive cell's Brillouin zone due to an imposed relationship between the wave function of the supercell and the wave function of the primitive cell. When we construct a supercell by counting the existing primitive cells within the supercell, we can express the wave function that represents the electron in the supercell as a linear combination of the electron wave functions of the primitive cell, i.e.,

$$|\vec{K},m\rangle = \sum_{i,n} a(\vec{k}_i,n;\vec{K},m)|\vec{k}_i,n\rangle, \tag{3.1}$$

where m (n) is the band index to $|\vec{K},m\rangle$ ($|\vec{k}_i,n\rangle$). The wave function for a crystal in the basis of states $|\vec{k},n\rangle$ acquires a phase factor in the reciprocal space of the primitive cell due to the periodicity of the lattice. For the wave function of the supercell, this phase factor is related to the lattice constant of the supercell (expressed in terms of volumes). The two phases are related to

each other by

$$\vec{k}_i = \vec{K} + \vec{G}_{\vec{k}_i \leftarrow \vec{K}}, \quad i = 1,2,...,N, \tag{3.2}$$

where $\vec{G}_{\vec{k}_I \leftarrow \vec{K}}$ it is the lattice vector of the supercell that completes the primitive cell (completes $\vec{k}i$). We say that $\vec{k}i$ is folded into $\vec{K}$ by a factor $\vec{G}_{\vec{k}_i \rightarrow \vec{K}}$, or that $\vec{K}$ is unfolded into $\vec{k}i$ by the same factor ($\vec{G}_{\vec{k}_i \leftarrow \vec{K}}$) (Boykin; G., 2005; Diretzis *et al.*, 2014). Thus, equation 3.1 takes the form of

$$|\vec{K},m\rangle = \sum_{i,n} a(\vec{k}_i,n;\vec{K},m)|(\vec{K}+\vec{G}_i),n\rangle. \tag{3.3}$$

We can further analyze the eigenstates of the supercell as the projection of these states onto the basis of eigenstates of the primitive cell, and thus write it as

$$|\vec{K},m\rangle = \sum_{i,n} |\vec{k}_i,n\rangle \langle\vec{k}_i,n|\,\vec{K},m\rangle, \tag{3.4}$$

with the eigenstates $|\vec{k}_i,n\rangle$ obeying the normalization and completeness conditions. From the definitions of equations 3.1 and 3.4, it is easy to observe that the basis of states we use to form the eigenstates of the supercell is the one in which they are projected onto the primitive cell with a probability given by

$$P_{\vec{K},m}(\vec{k}_i) = \sum_n |\langle\vec{K},m|\vec{k},n\rangle|^2 = \sum_n |a(\vec{k}_i,n;\vec{K},m)|^2. \tag{3.5}$$

This relationship is defined as the spectral weight. Since we are considering all the unfolded energy states within the Brillouin zone of the primitive cell, the sum of all the spectral functions in this region, governed by the vectors $\vec{G}_i$, must be

$$\sum_i P_{\vec{K},m}(\vec{k}_i) = \sum_{i,n} |a(\vec{k}_i,n;\vec{K},m)|^2 = 1. \tag{3.6}$$

The interpretation of the relationship between the wave functions of the SC and the wave functions of the PC can also be understood as a translation in the lattice given by the translation operator $\sum_{i,n} |(\vec{K}+\vec{G}_i),n\rangle \langle(\vec{K}+\vec{G}i),n|$, such that the lattice vectors governing this translation are given by $\vec{G}_i$.

3.2.1 Spectral function

The spectral function is defined as

$$\mathbf{F}(\vec{k}_i,E) = \sum_m P_{\vec{K},m}(\vec{k}_i)\delta(E-E_m), \tag{3.7}$$

which includes only the $\vec{k}i$ that satisfy $\vec{k}i = \vec{K} + \vec{G}_i$, gives us the energy spectrum of unfolded supercell systems in the primitive Brillouin zone, i.e., the band structure of the supercell projected onto the primitive cell, where it is possible to analyze systems that have modifications in their crystal structure. For a perfect crystal, the spectral function of a supercell will give us the exact band structure of the primitive cell.

3.2.2 Energetic weight

Writing the Hamiltonian in the basis of the supercell states,

$$\mathbf{H} = \sum_m |\vec{K}, m\rangle\langle\vec{K}, m| E_m, \tag{3.8}$$

and solving the Schrödinger equation by applying the wave function of the primitive cell, we obtain

$$E_n = \langle\vec{k}_i, n|\mathbf{H}|\vec{k}_i, n\rangle = \sum_m |\langle\vec{K}, m|\vec{k}_i, n\rangle|^2 E_m = \sum_m |a(\vec{k}_i, n; \vec{K}, m)|^2 E_m, \tag{3.9}$$

with $\vec{k}i = \vec{K} + \vec{G}i$. By doing this, we obtain the energies of the primitive cell on the basis of states of the supercell, unfolded in the primitive Brillouin zone, with the weight of each eigenstate given by $|a(\vec{k}_i, n; \vec{K}, m)|^2$. The effects caused by modifications in the crystal structure of the supercell can now be analyzed in the effective band structure of the primitive cell.

3.3 Block function bases

The crystal is formed by an infinite set of supercells, where each supercell, with translation vector $\vec{R}s$ locating the s-th supercell, consists of a finite number of primitive cells, with translation vector $\vec{\nu}r$ locating the r-th primitive cell within the supercell. This system obeys periodic boundary conditions. Due to this, we can write a wave function that represents an energy state E_n as a Bloch function in the representation of the primitive cell with a phase factor given by $\vec{k}_i$, i.e.,

$$|\vec{k}_i, n\rangle = \frac{1}{\sqrt{N_{cp}}} \sum_{\{\vec{\nu}\}} \sum_{\mu,\alpha} \beta_n^{\mu\alpha}(\vec{k}_i) e^{i.\vec{k}_i.\vec{\nu}_r} |\vec{r} - \vec{\nu}_r\rangle, \tag{3.10}$$

where μ and α represent the summation over atoms and atomic orbitals, respectively. Any vector $\vec{\nu}r$ can be written in terms of the lattice vector of a supercell that contains Npc primitive cells within it. Thus, writing $\vec{\nu}r = \vec{R}s + \vec{r}j$, where $\vec{r}j$ indicates the position of the primitive cell within

the supercell, and considering the relationship between the phase vectors given by Equation 3.2, by substituting these two relationships into Equation 3.10, we obtain

$$|(\vec{K}+\vec{G}_i),n\rangle = \frac{1}{\sqrt{N_{cp}N_{sc}}}\sum_{s,j}\sum_{\mu,\alpha}\beta_n^{\mu\alpha}(\vec{K}+\vec{G}_i)e^{i.\vec{K}.\vec{R}_s}e^{i.(\vec{K}+\vec{G}_i).\vec{r}_j}\,|r-\vec{v}_r\rangle\,, \tag{3.11}$$

where $s = 1,2,\ldots,N_{sc}$ and $j = 1,2,\ldots,N_{pc}$, and we have used $e^{i.\vec{G}i.\vec{R}s} = 1$ as a consequence of the relationship $\mathbf{a}i.\mathbf{b}j = 2\pi\delta_{ij}$. From the perspective of the supercell, the wave function in this representation with phase factor $\vec{K}$ can be written as

$$|\vec{K},m\rangle = \frac{1}{\sqrt{N_{sc}}}\sum_{s,j}\sum_{\mu,\alpha}B_{m,j}^{\mu\alpha}(\vec{K})e^{i.\vec{K}.\vec{R}_s}\,|r-\vec{v}_r\rangle\,. \tag{3.12}$$

As seen in section 3.2, the wave function of the supercell can be understood as a superposition of eigenstates of the primitive cell, being written as a linear combination of these, i.e.,

$$|\vec{K},m\rangle = \sum_{i,n}a(\vec{k}_i,n;\vec{K},m)\,|(\vec{K}+\vec{G}_i),n\rangle\,. \tag{3.13}$$

By substituting equations 3.11 and 3.12 into equation 3.13 and considering the orthonormality of $|r-\vec{v}\rangle$ and some algebraic manipulation, we obtain

$$B_{m,j}^{\mu\alpha}(\vec{K})e^{-i.\vec{K}.\vec{r}_j} = \frac{1}{\sqrt{N_{pc}}}\sum_i a(\vec{k}_i,n;\vec{K},m)\beta_n^{\mu\alpha}(\vec{K}+\vec{G}_i)e^{i.\vec{G}_i.\vec{r}_j}, \tag{3.14}$$

which can also be seen as a set of matrix equations of the form

$$\mathbf{B}_m^{\mu\alpha}(\vec{K}) = \mathbf{U}.\mathbf{A}_m^{\mu\alpha}(\vec{K}), \tag{3.15}$$

where

$$\mathbf{B}_m^{\mu\alpha}(\vec{K}) = \left[B_{m,j}^{\mu\alpha}(\vec{K})e^{-i.\vec{K}.\vec{r}_j}\right]_{j=1,\ldots,N_{pc}}, \tag{3.16}$$

$$\mathbf{A}_m^{\mu\alpha}(\vec{K}) = \left[a(\vec{k}_i,n;\vec{K},m)\beta_n^{\mu\alpha}(\vec{K}+\vec{G}_i)\right]_{i=1,\ldots,N_{pc}} \tag{3.17}$$

and

$$\mathbf{U} = \frac{1}{\sqrt{N_{pc}}}\left[e^{i.\vec{G}_i.\vec{r}_j}\right]_{i,j=1,\ldots,N_{pc}} \tag{3.18}$$

An analysis of the vectors $\vec{r}j$ and $\vec{G}i$ in Equation 3.17 reveals the unitarity of the matrix U, which leads to a solution for $\mathbf{A}_m^{\mu\alpha}(\vec{K})$ in the form

$$\mathbf{A}_m^{\mu\alpha}(\vec{K}) = \frac{1}{\sqrt{N_{pc}}}\sum_j B_{m,j}^{\mu\alpha}(\vec{K})e^{-i.(\vec{K}+\vec{G}_i).\vec{r}_j} \tag{3.19}$$

The normalization of the wave function in the primitive Brillouin zone allows us to extract from Equation 3.15 the coefficients responsible for the weight of each unfolded supercell eigenstate in the primitive cell, i.e.,

$$|a(\vec{k}_i,n;\vec{K},m)|^2 = |\mathbf{A}_m^{\mu\alpha}(\vec{K})|^2. \tag{3.20}$$

With this, we find the probability

$$P_{\vec{K},m}(\vec{k}_i) = \sum_n |a(\vec{k}_i,n;\vec{K},m)|^2 = \frac{1}{N_{pc}} \sum_{\mu,\alpha} \left| \sum_j B_{m,j}^{\mu\alpha}(\vec{K}) e^{-i.(\vec{K}+\vec{G}_i).\vec{r}_j} \right|^2, \tag{3.21}$$

is interpreted as the weight that each supercell eigenstate, with wavevector $\vec{K}$, has when it unfolds into a primitive cell eigenstate with wavevector $\vec{k}_i$. Equation 3.21 represents the sum over all possible states of the squared modulus of the product of supercell eigenvectors with a translation exponential guided by $\vec{G}_i$ within the primitive cell. This expression allows us to obtain information about the band structure in the primitive Brillouin zone solely based on information from the supercell structure, formed by a basis of Bloch functions.

Figure 14 – Supercell (red) into the primitive cell (blue) of Graphene structure in phase-space. The band structure is calculated with the 1 to 9 paths in the supercell so that it corresponds to the desired path to be analyzed in the primitive cell (solid black line in the primitive cell) via the BU process.

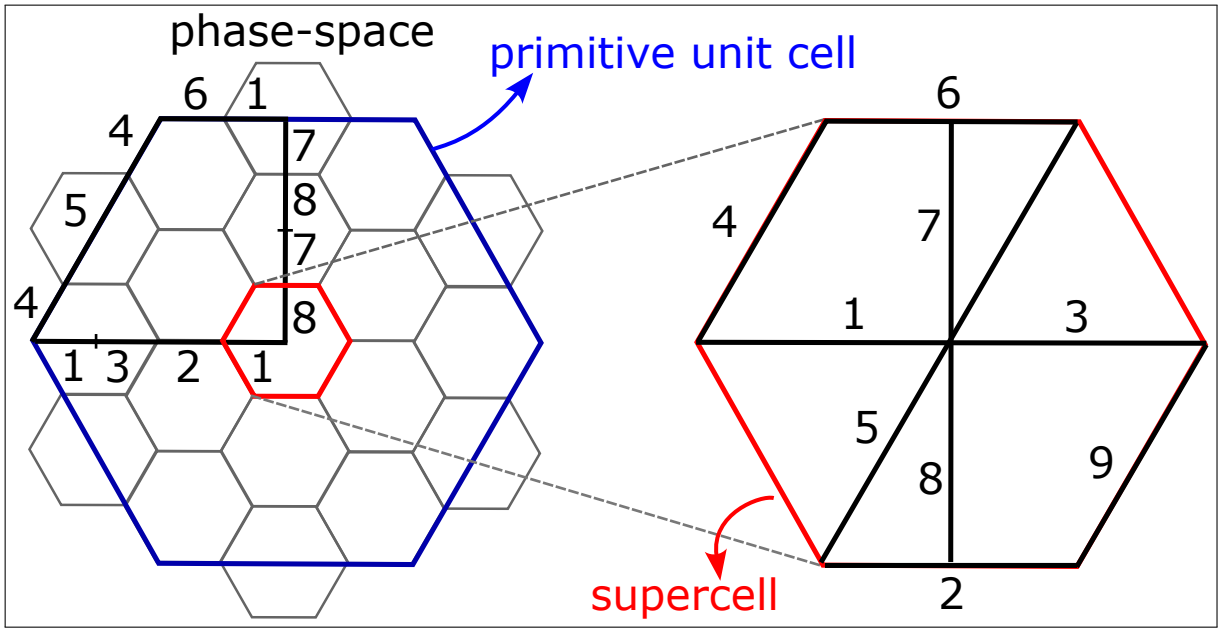

Source: Figure elaborated by the author (2023).

As an example, let's unfold the energy bands of a 6x6 graphene supercell. For this, we will use the Pybinding Python package to calculate the band structure of graphene. With the calculated points in the supercell and the corresponding energies, we can use them to perform

the unfolding into the primitive cell. The path where we need to calculate the band structure of the supercell is not as straightforward as calculating for the primitive cell, where typically the K and K' points are analyzed. To analyze the primitive cell from the supercell, we must consider all the points in the supercell that, when unfolded, fill the path we want to analyze in the primitive cell, as shown in Figure 14. The path in the supercell indicated as number 1 in Figure 14 (b) unfolds into three different locations along the path in the primitive cell, as shown in Figure 14 (a). Another collection of points that unfolds into multiple regions is path 4. By considering the appropriate point correspondence in the supercell, we can unfold them in a way that fills the entire path of points in the primitive cell.

Figure 15 – Example of band unfolding: (a) The result of unfolding the energy bands for a 6×6 supercell of a graphene sheet. (b) Band structure of the primitive cell calculated along the path in the reciprocal space Γ - M - K' - K - Γ. (c) Band structure of the supercell calculated along the path labeled 1-9 in the supercell.

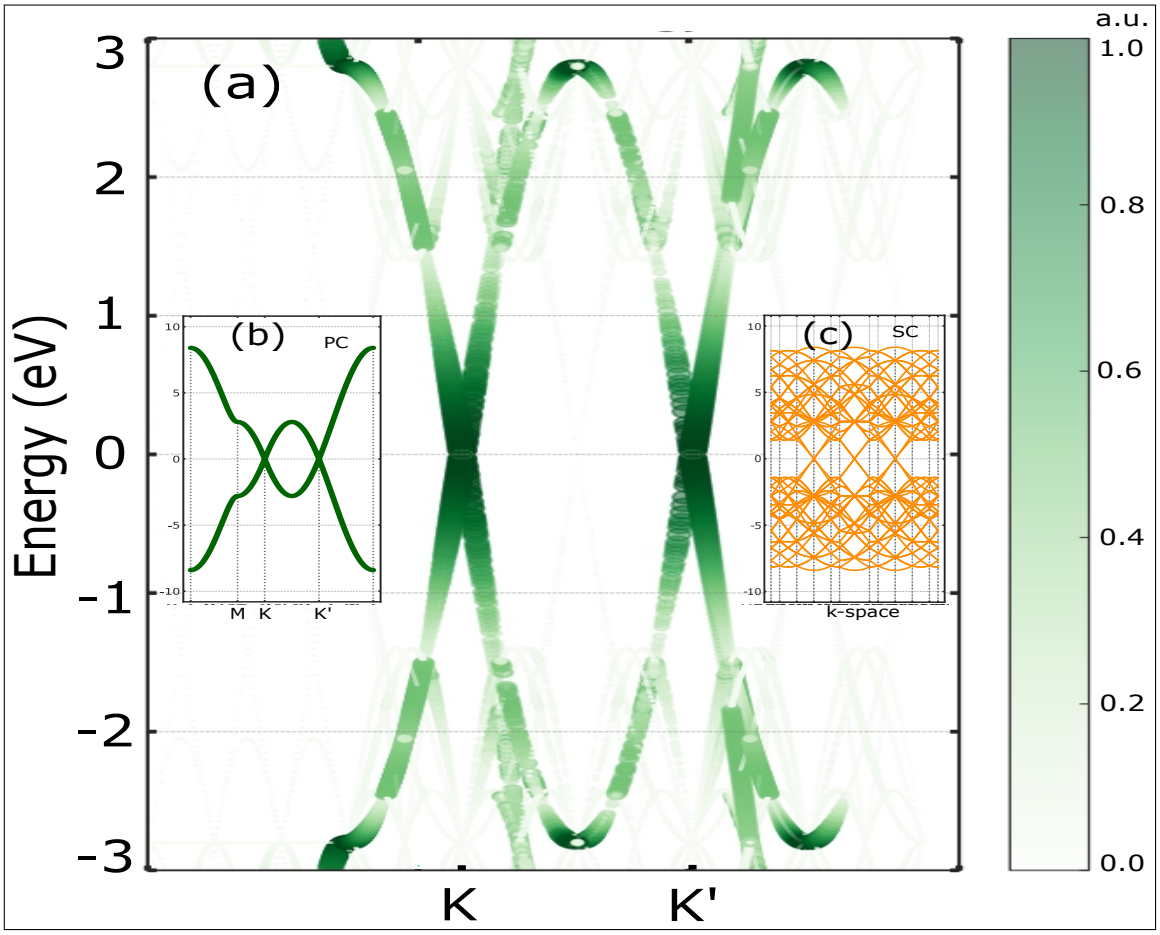

Source: Figure elaborated by the author (2023).

In this example, we will analyze the path in the primitive cell that contains the points K' and K, as shown by the solid black line in the primitive cell in Figure 14 (left). Figure 15 (b) displays the band structure of the primitive cell calculated along the following sequence: Γ - M -

K’ - K - Γ. Figure 14 (right) illustrates the path in the supercell where we need to calculate the energies that will unfold along the primitive cell path. Figure 15 (c) shows the band structure of the supercell calculated along the path labeled 1-9 in the supercell. The result of unfolding the energy bands for a 6×6 supercell of a graphene sheet is depicted in Figure 15 (a). At low energies, the unfolded band result demonstrates great quality, exhibiting in near the Dirac points an identical region compared with the band structure of the primitive cell.

4 LANDAUER-BÜTTIKER FORMALISM

4.1 From macroscopic to mesoscopic systems

The Landauer-Bütiker formalism enables the calculation of conductance in mesoscopic systems where Ohm's Law is no longer sufficient for determining electric current in a conductor of a few nanometers. At this scale, conductance no longer depends on the length or width of the conductor, requiring a quantum approach to describe the phenomenon. Moreover, for electrons moving in one direction, the conductance, previously denoted as

$$G = \frac{I}{V} = \frac{\sigma A}{L}, \tag{4.1}$$

where σ is the conductivity, A is cross-section area of a conductor of length L, is now expressed as

$$G = \frac{I}{V} = \frac{2e^2}{h}, \tag{4.2}$$

where e is the electron charge and h is the plank constant. And supposing electrons being injected in the mode μ in the scattering center, the electrons emerging in mode ν contribute

$$G = \frac{2e^2}{h}|T_{\mu\nu}|^2 \tag{4.3}$$

to the conductance, where $T_{\mu\nu}$ giving us the transmission magnitude for an electron incident from the left in mode μ to be transmitted on the right in mode ν. The overall conductance is calculated by adding up the conductances across all input and output channels.

$$G = \frac{2e^2}{h}\sum_{\mu\nu}|T_{\mu\nu}|^2 \tag{4.4}$$

4.2 Landauer-Bütiker formula

The case analyzed in the previous section considers only one input terminal and one output terminal, which represents the simplest model explained by Landauer. However, problems involving multiple input and output terminals are more common in practical systems. Bütiker described a solution for this type of system by generalizing the case of two terminals to the case of n terminals through the summation over all terminals. Thus, one can express the current flowing through the scattering center by utilizing a square conductance matrix, where the dimensions of the matrix are determined by the number of leads present, available by

$$I_\mu = \sum_\nu [G_{\mu\nu}V_\nu - G_{\nu\mu}V_\mu], \tag{4.5}$$

with

$$G_{\mu\nu} = \frac{2e^2}{h}\bar{T}_{\mu\nu}, \tag{4.6}$$

where

$$\bar{T}_{\mu\nu} = \sum_{\mu\nu} |T_{\mu\nu}|^2. \tag{4.7}$$

We see by Equation 4.5 that to ensure that the current is zero when all the potentials are equal, the coefficients $G_{\mu\nu}$ must satisfy the following rule

$$\sum_{\nu} G_{\mu\nu} = \sum_{\nu} G_{\nu\mu} \tag{4.8}$$

Equation 4.5 provides the following expression for a three-terminal system:

$$\begin{pmatrix} I_1 \\ I_2 \\ I_3 \end{pmatrix} = \begin{pmatrix} G_{12}+G_{13} & -G_{12} & -G_{13} \\ -G_{21} & G_{21}+G_{23} & -G_{23} \\ -G_{31} & -G_{32} & G_{31}+G_{32} \end{pmatrix} \cdot \begin{pmatrix} V_1 \\ V_2 \\ V_3 \end{pmatrix}. \tag{4.9}$$

5 OPTICAL QUANTITIES

5.1 Two-dimensional dielectric function

The two-dimensional dielectric function, with units of length, is (Berkelbach *et al.*, 2015):

$$\varepsilon_2(\omega) = \frac{4\pi^2 e^2}{m^2\omega^2}\sum_{cv}\int_{BZ}\frac{d^2k}{(2\pi)^2}|\lambda\cdot\mathbf{P}^{vc}(\mathbf{k})|^2\delta[E_c(\mathbf{k})-E_v(\mathbf{k})-\hbar\omega], \tag{5.1}$$

where ω is the frequency of the light and $\lambda\cdot\mathbf{P}^{vc}(\mathbf{k}) = \langle\psi_{vk}|\lambda\cdot\mathbf{p}|\psi_{ck}\rangle$. The summation runs over $\mathbf{k}$, the spin variable s, and the band indices v (occupied) and c (unoccupied), and the integral extends over the first Brillouin zone. Eq. (5.1) connects the band structure with the optical properties. The imaginary part of the complex dielectric function ε=$\varepsilon_1 + i\varepsilon_2$ depends on the absorption coefficient $\alpha(\omega)$ by $\alpha(\omega)$=$\omega\varepsilon_2/(nc)$, where n is the ordinary refraction index. The absorption coefficient, in turn, depends on the number of transitions per unit time per unit volume $W(\omega)$ by $\alpha(\omega)$=$\hbar\omega W(\omega)/(uc/n)$, where u is the energy density. The deduction of the two-dimensional dielectric function was performed in Ref. (Bassani *et al.*, 1976) using Fermi's golden rule, so that the number of transitions per unit time per unit volume is given by:

$$W(\omega) = \frac{2\pi}{\hbar}\sum_f |V_{fi}|^2\delta(E_f - E_i - \hbar\omega), \tag{5.2}$$

where $V_{fi} = (eA_0/mc)\lambda\cdot\mathbf{P}^{vc}(\mathbf{k})$ induces a transition from the initial state i of energy E_i to the final state f of energy E_f.

5.2 Momentum matrix elements

The elements of the momentum matrix normal to the layer are zero due to symmetry. Therefore, we will be interested only in the elements of the momentum matrix in the plane, given by:

$$\mathbf{P}^{vc}(\mathbf{k}) = -\frac{im}{\hbar}\langle\psi_{vk}|[r,H]|\psi_{ck}\rangle, \tag{5.3}$$

using the representation of the position operator in the momentum space, we can rewrite Eq. (5.3) as

$$\mathbf{P}^{vc}(\mathbf{k}) = \frac{m}{\hbar}\langle\psi_{vk}|\nabla_k H|\psi_{ck}\rangle. \tag{5.4}$$

This is the main term to obtain semi-analytically the optical quantities that are used phenomenologically to describe the optical properties of multilayer phosphorene. In addition, it is important

to note that Eq. (5.4) disregards on-site energy, in accordance with the most accurate model for the multilayer phosphorene proposed in Rudenko & Katsnelson (2014a), which takes into account the interactions of ten nearest-neighbors intralayer, five nearest-neighbors interlayer, and on-site energies of the four sublattices can be taken as zero.

6 EFFECTS ON THE ELECTRONIC PROPERTIES OF MULTILAYER PHOSPHORENE DUE TO PERIODIC ARRAYS OF VACANCIES

In this chapter, we investigate the effects of atomic vacancies on the band structure of multilayer phosphorene using a combination of the tight-binding model and the band unfolding technique. A detailed description of the used theoretical framework is illustrated for defect-free structures of monolayer, bilayer, and trilayer phosphorene with Bernal stacking, which allowed us to identify that the stability of the unfolded effective band is dependent on the size of the supercell for the *N*-layer phosphorene. Our results demonstrate that due to the presence of monovacancy a quasi-flat state emerges around the Fermi level and the energy difference between the lowest conduction band (or highest valence band) and the quasi-flat state depends on the position of the vacancy and its proximity to the boundary of the supercell, which can bring up consequences to the optical properties of the system. By increasing vacancy concentration, different distinguished forms of vacancy disorder are possible, by keeping or not the sublattice symmetry of the system as well as by assuming a combination of different types of vacancies and layer-localization to form the n atomic vacancies. In general, we find an almost n-fold degenerate quasi-flat state in a system with n vacancies when the sublattice symmetry or/and the inversion symmetry are broken, i.e. when the number of non-equivalent sublattice atoms in each phosphorene sheet is different. Moreover, the occurrence of atomic vacancies in the supercell affects also the energetic position of the bulk states as greater the number of vacancies consequently leads to an increase in the broadening of the n-fold quasi-degenerate quasi-flat states. The present formalism provides an appropriate theoretical platform to investigate point defect effects on the optoelectronic properties of multilayer van der Waals materials.

6.1 Motivation

The recent exfoliation of the layered bulk version of black phosphorus (BP) into the few-layer form, known as *N*-layer phosphorene, in 2014 (Li *et al.*, 2014; Castellanos-Gomez *et al.*, 2014) and the experimental measurements of its anisotropic physical properties, such as the direction-dependent and thickness-dependent high charge-carrier mobility (Li *et al.*, 2014; Rodin; Carvalho; Neto, 2014; Liu; Neal, 2014) and anisotropic angle-resolved optical absorption (Torbatian; Asgari, 2018), places few-layer phosphorene in evidence in the research for new optoelectronic-based systems composed by anisotropic two-dimensional (2D) materials (Carvalho *et al.*, 2016a; Akhtar *et al.*, 2017). Most of the exotic properties of few-layer BP arise

as a consequence of the crystallographic structure and the sp^3 hybridization of the phosphorus atoms organizing in a puckered hexagonal lattice which yields a highly anisotropic band structure, that in turn leads to different effective masses and different group velocities along the x and y directions. Moreover, few-layer phosphorene is a semiconductor material with a tunable band gap ranging from 1.8 eV for the single-layer BP case to ≈ 0.4 eV for bulk form (Castellanos-Gomez, 2015; Dolui; Quek, 2015a; Das *et al.*, 2014; Kim *et al.*, 2015; Chaves *et al.*, 2021; Tran *et al.*, 2014), i.e. spanning from the midinfrared to near-infrared, proving to be an ideal platform material for optoelectronics applications.

During experimental processes of sample preparation of structures made out of 2D materials, which includes realizations/synthesis itself and transfer/deposition to certain appropriate substrates, always are noted defects, such as vacancies, adatoms, edges disorders, grain boundaries, and substitutional or interstitial impurities (Addou; Colombo, 2022; Bertoldo *et al.*, 2022; Wu; Ni, 2017; Ahmad *et al.*, 2021; Jiang *et al.*, 2019; Banhart *et al.*, 2011; Araujo *et al.*, 2012). It was well-known for three-dimensional crystals that the presence of structural defects in the crystallographic lattice modifies the optoelectronics and transport properties of the system. Therefore, very soon after the experimental realization of graphene (the first obtained 2D material) (Novoselov *et al.*, 2004), a great interest to understand how graphene physics is modified due to vacancy disorders, originating from removing carbon atoms, has been the subject of substantial theoretical and experimental investigations. For instance, owing to the defects in the case of few-layer graphene, it was observed electronic mobility reduction (McCreary *et al.*, 2010; Costa *et al.*, 2017), changes in the band structure (Banhart *et al.*, 2011; Miranda *et al.*, 2022; Kishimoto; Okada, 2016), the possibility of the emergence of magnetic ordering (Brey *et al.*, 2007; Esquinazi *et al.*, 2003; Yazyev; Helm, 2007; Palacios; Ynduráin, 2012; Chen *et al.*, 2014; Nakhmedov *et al.*, 2019; Francis *et al.*, 2015; Ma *et al.*, 2004), and the emergence of zero energy modes, which are localized states around the missing carbon atoms being energetically placed around the Fermi level (Kishimoto; Okada, 2016; Ovdat *et al.*, 2020; Kotakoski *et al.*, 2011; Lee *et al.*, 2005; Palacios *et al.*, 2008; El-Barbary *et al.*, 2003; Hahn; Kang, 1999).

Similarly, soon after the phosphorene exfoliation, there was a growing interest in studying defective few-layer BP structures, including intrinsic or extrinsic defects, as well as neutral or charged defects, in order to design and functionalize them for future applications (Li *et al.*, 2015; Zhang; Wu; Yang, 2016; Lei *et al.*, 2017b; Lei *et al.*, 2017a; Kistanov *et al.*, 2016; Smotlacha; Pincak, 2018; Sun *et al.*, 2018; Arra; Babar; Kabir, 2019; Li; Peeters, 2018; Dai

et al., 2017; Kiraly *et al.*, 2017; Harsh *et al.*, 2022; Huang *et al.*, 2022; He *et al.*, 2019; Zhan *et al.*, 2019; Li *et al.*, 2022; Aghajanian; Mostofi; Lischner, 2022; Fang *et al.*, 2022; Rijal *et al.*, 2021; Rezaei *et al.*, 2021; Gupta; Periasamy; Narayanan, 2021; Yao *et al.*, 2020; Pei *et al.*, 2020; Kundu; Naik; Jain, 2020; Wang *et al.*, 2015; Kripalani *et al.*, 2019; Shah *et al.*, 2019; Cai *et al.*, 2019; Amini *et al.*, 2019a; Amini *et al.*, 2019b; Riffle *et al.*, 2018; Cai *et al.*, 2016; Gaberle *et al.*, 2018; Hu *et al.*, 2015; Farooq *et al.*, 2015). For instance, vacancies and antidots have been induced in the BP lattice with intention of obtaining tunable optoelectronic properties making this material suitable for applications in LEDs, photocells, and photodetectors (Lei *et al.*, 2017a). The experimental study reported in Kiraly *et al.* (2017) observed, via a combination of low-temperature scanning tunneling microscopy/spectroscopy (STM/STS), that the spatial distributions of the wave functions are localized around the atomic vacancies on the surface of bulk BP and they exhibit strong anisotropy. Reference Fang *et al.* (2022) also experimentally demonstrated by means of STM that ionization of single vacancy into negatively charged single vacancy leads to the passivation of dangling bonds and thus the quenching of in-gap states, where the single vacancy exhibits a strong and symmetric Friedel oscillation pattern, while the charged single vacancy shows an asymmetric pattern. From the theoretical point of view, intrinsic defects in the BP lattice structure, such as monovacancies or divacancies, have been investigated for the cases of infinite few-layer BP lattices (Li *et al.*, 2015; Zhang; Wu; Yang, 2016; Kistanov *et al.*, 2016; Dai *et al.*, 2017; Kundu; Naik; Jain, 2020; Wang *et al.*, 2015; Kripalani *et al.*, 2019; Cai *et al.*, 2019; Hu *et al.*, 2015; Farooq *et al.*, 2015), by considering periodic boundary conditions of a large supercell, and of nanostructures, such as nanoribbons (Smotlacha; Pincak, 2018; Sun *et al.*, 2018; Li; Peeters, 2018; Amini *et al.*, 2019b; Rezaei *et al.*, 2021; Amini *et al.*, 2019a). For the nanoribbons BP case, the results indicated a strong structural dependence on the vacancy position with respect to its proximity to the nanoribbon edges (Smotlacha; Pincak, 2018; Sun *et al.*, 2018) and the vacancy type (Li; Peeters, 2018; Amini *et al.*, 2019b).

Despite the vast literature regarding different theoretical and experimental research on defective phosphorene (Li *et al.*, 2015; Zhang; Wu; Yang, 2016; Lei *et al.*, 2017b; Lei *et al.*, 2017a; Kistanov *et al.*, 2016; Smotlacha; Pincak, 2018; Sun *et al.*, 2018; Arra; Babar; Kabir, 2019; Li; Peeters, 2018; Dai *et al.*, 2017; Kiraly *et al.*, 2017; Harsh *et al.*, 2022; Huang *et al.*, 2022; He *et al.*, 2019; Zhan *et al.*, 2019; Li *et al.*, 2022; Aghajanian; Mostofi; Lischner, 2022; Fang *et al.*, 2022; Rijal *et al.*, 2021; Rezaei *et al.*, 2021; Gupta; Periasamy; Narayanan, 2021; Yao *et al.*, 2020; Pei *et al.*, 2020; Kundu; Naik; Jain, 2020; Wang *et al.*, 2015; Kripalani *et al.*,

2019; Shah *et al.*, 2019; Cai *et al.*, 2019; Amini *et al.*, 2019a; Amini *et al.*, 2019b; Riffle *et al.*, 2018; Cai *et al.*, 2016; Gaberle *et al.*, 2018; Hu *et al.*, 2015; Farooq *et al.*, 2015) and the several works using different theoretical models to present predictions about the main phosphorene properties, ranging from *ab initio* calculations (Tran *et al.*, 2014; Jing; Park, 2014; Fei; Yang, 2014; Wei; Peng, 2014; Shriber *et al.*, 2018; Qin *et al.*, 2015) to semi-empirical methods, as tight-binding model (Takao; Asahina; Morita, 1981; Rudenko; Katsnelson, 2014a; Rudenko; Yuan; Katsnelson, 2015; Sousa *et al.*, 2017b; Lino *et al.*, 2017; Melo *et al.*, 2018; Jr; Katsnelson, 2015; Sousa *et al.*, 2016; Sousa *et al.*, 2017a) and continuum approach (Jr; Katsnelson, 2015; Sousa *et al.*, 2016; Sousa *et al.*, 2017a; Cunha *et al.*, 2019), to our knowledge, there is a lack of a systematic, appropriate, and carefully taken study on the band unfolding process to deal with large supercells by considering multiple vacancies in multilayer phosphorene and the obtention of their non-duplicated band structures in the reciprocal space in the presence of point defects.

In this context, this work aims to present the usage of the theoretical framework based on the combination of the tight-binding model, discussed in Rudenko & Katsnelson (2014a), Rudenko, Yuan & Katsnelson (2015), Sousa *et al.* (2017a), and the band unfolding formalism, whose technique bases are found defined in references (Zang; Wang, 2011; Medeiros *et al.*, 2014; Cui *et al.*, 2015; Maspero *et al.*, 2016; Nishi *et al.*, 2017; Babar *et al.*, 2018; Boykin; G., 2005; Boykin *et al.*, 2007; Ku *et al.*, 2010; Popescu; Zunger, 2010; Popescu; Zunger, 2012; Allen *et al.*, 2013; Diretzis *et al.*, 2014; Huang *et al.*, 2014; Boykin *et al.*, 2016; Medeiros *et al.*, 2015), to investigate the vacancy-induced changes in the band structures of the monolayer, bilayer, and trilayer phosphorene. Different vacancy formations shall be assumed by removing phosphorous atoms keeping or not the sublattice symmetry of the equivalent sublattices (A/D and B/C associated with the D_{2h}-symmetry) in multilayer BP (Sousa *et al.*, 2017a), as well as we shall also consider different layer locations for the point defects inside the supercell, assuming them in the same layer or different layers, to form single, double, and triple vacancies. The chapter is organized as follows. We present the two theoretical methodologies used in this work to obtain the unfolded band structures of multilayer phosphorene in the presence of a periodic array of vacancies, namely, the tight-binding model in Sec. 6.2 and the unfolding procedure in Sec. 6.3. In Sec. 6.4.1, we show the results and discussions of the analysis of vacancy defects in monolayer phosphorene. In Sec. 6.4.2, we extend our analysis of the presence of point defects for the bilayer and trilayer phosphorene cases. Finally, our final remarks are presented in Sec. 6.5.

Figure 16 – Schematic illustrations of the lattice structure of monolayer phosphorene, emphasizing: in panel (a) the atomic positions, the four inequivalent sublattices (A and B at the bottom sublayer in cyan color and C and B at the top sublayer in blue color), the in-plane (a_1) and out-of-plane (a_2) lattice distances, the in-plane (α) and out-of-plane (β) angles associated to the chemical bonds connecting sublattices in the same and different sublayers, respectively, and the Brillouin zone in reciprocal space with its high symmetry points; in panel (b) the crystallographic structure of phosphorene sketched for the 4×4 supercell case with size $L_x \times L_y$ and the ten-intralayer hopping parameters; and in panel (c) a perspective view of the monolayer and a side view of the multilayer phosphorene cases, indicating the five-interlayer hopping parameters and the lattice parameter in the out-of-plane (z-)direction. (d) Band structures along the high-symmetry path $\mathbf{S}-\mathbf{Y}-\Gamma-\mathbf{X}-\mathbf{S}$ of the pristine (first row) monolayer, (second row) bilayer, and (third row) trilayer phosphorene obtained (left column) solely by the tight-binding model and (right column) via the combination of the tight-binding model and the band unfolding formalism for 6×6 supercell, in order to show the full agreement between them.

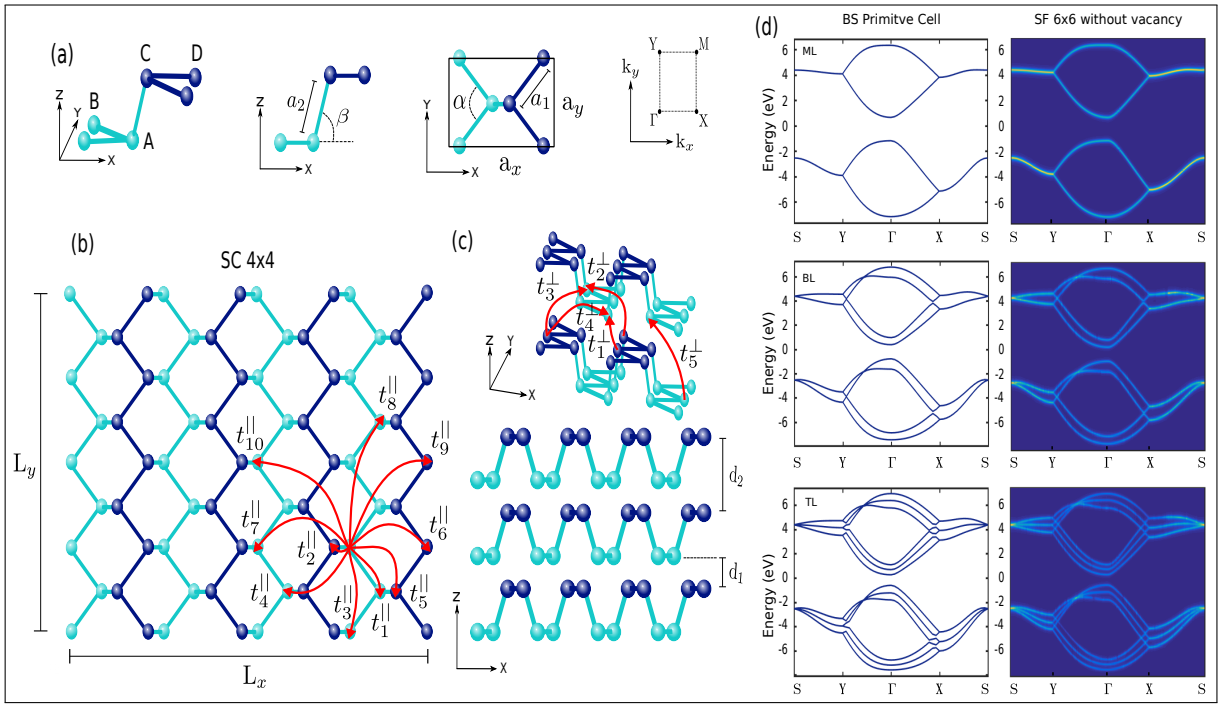

Source: Figure elaborated by the author (2023).

6.2 Tight-binding model

Phosphorene, a 2D material constituted by phosphorus atoms, has a top-view crystallographic structure similar to the honeycomb lattice of graphene. However, in contrast to graphene, it presents out-of-plane chemical bonds, due to the sp^3 hybridization of the phosphorus atoms, which in turn leads to a puckered surface that can be described by two sublayers, as represented by different colors in Figure 16: sublattices A and B (C and D) at the bottom (top) sublayer with cyan (blue) symbols. Thus, as sketched in Figure 16 (a), each monolayer

phosphorene contains four inequivalent sublattices, labeled by A, B, C, and D, per unit cell. By fixing the coordinate system at the B sublattice, as shown in the left panel of Figure 16 (a), the vector positons of such sublattices are given, respectively, by $\mathbf{r}_A = [a_1\cos(\alpha/2), a_1\sin(\alpha/2), 0]$, $\mathbf{r}_B = (0,0,0)$, $\mathbf{r}_C = [a_1\cos(\alpha/2)+a_2\cos(\beta), a_1\sin(\alpha/2), a_2\sin(\beta)]$, and $\mathbf{r}_D = [2a_1\cos(\alpha/2)+a_2\cos(\beta), 0, a_2\sin(\beta)]$, where $a_1 = 0.222$ nm and $a_2 = 0.224$ nm are the bond lengths, and $\alpha = 96.40^\circ$ and $\beta = 71.64^\circ$ the bond angles, as illustrated in the second and third panels of Figure 16 (a). The combination of primitive unit cells gives rise to supercells. The lattice parameters of a supercell are $L_x = Ma_x$ and $L_y = Na_y$ along the x and y directions, respectively, such that a $M\times N$ supercell is formed by assembling M (N) replicas of the primitive cell in the y (x) direction. For example, Figure 16 (b) shows a 4×4 supercell. Phosphorene multilayers have an orthorhombic crystal structure formed by stacking phosphorene monolayers bonded via van der Walls interactions, which we assumed here to be the AB (Bernal) stacking, since this is the most energetically stable stacking configuration according to first-principle calculations(Çakır *et al.*, 2015). The separation between the monolayers is $d_1 = 0.321$ nm and the adjacent distance between two same sublayers in different layers is $d_2 = 0.53$ nm, as sketched in Figure 16 (c).

The band structure of multilayer phosphorene can be calculated using the tight-binding model, which consists of writing the charge carrier wavefunction as a linear combination of atomic orbitals (Sousa *et al.*, 2017a). This approach is a semi-empirical method widely used in calculating the band structure in solid-state physics (Lima *et al.*, 2022). The model consists of considering a crystalline system where the electron feels a periodic lattice potential $V(\mathbf{r}+\mathbf{r}_i) = V(\mathbf{r})$, where $\mathbf{r}_i$ represents the translational periodicity vector of the i-th unit cell of the crystal. Based on the Bloch theorem, the probability density for the electron in such a system also obeys such a periodicity, i.e., $|\Psi(\mathbf{r}+\mathbf{r}_i)|^2 = |\Psi(\mathbf{r})|^2$. In this approximation, the Hamiltonian $\hat{H}$, considering that charge carriers can hop to the neighbors of a phosphorus atom, has the form in the second quantization language such as

$$\hat{H} = \sum_i (\varepsilon_i + V_i) c_i^\dagger c_i + \sum_{i\neq j} \tau_{ij}^{||} c_i^\dagger c_j + \sum_{i\neq j} \tau_{ij}^{\perp} c_i^\dagger c_j, \tag{6.1}$$

where $i = \{\mathbf{R}_i, \alpha, \nu\}$ represents the generalized index for the orbital ν of the atomic species α at the atomic site $\mathbf{R}_i$. Here, for the N-layer phosphorene case, one considers just a single-orbital per atom with all atoms of the same species (P), such that the sums run over all sites, a prior, of the crystal lattice, being c_i ($c_i^\dagger$) the operator that annihilates (creates) an electron at the site i with on-site energy ε_i, and $\tau_{ij}^{||}$ ($\tau_{ij}^{\perp}$) is the intralayer (interlayer) hopping parameter between

the i-th and j-th sites. Since all atoms are identical, the on-site energies only shift the Fermi energy. Therefore, without loss of generality, we adopted here $\varepsilon_i = 0$. The second and third terms of Eq. (6.1) correspond to the intralayer and interlayer interactions between sites i and j in the same or different layers, respectively. These sums run over 10 intralayer and 5 interlayer hoppings, as shown in Figure 22, with hopping parameters and lattice constants being the ones reported by Rudenko *et al.*(Rudenko; Yuan; Katsnelson, 2015), which takes advantage of the predominance of p_z characteristic near the band edges of multilayer phosphorene to construct a single-orbital tight-binding parameterization with GW_0 quality. In this model, the values $t_1^{||} = -1.486$ eV, $t_2^{||} = 3.729$ eV, $t_3^{||} = -0.252$ eV, $t_4^{||} = -0.071$ eV, $t_5^{||} = 0.019$ eV, $t_6^{||} = 0.186$ eV, $t_7^{||} = -0.063$ eV, $t_8^{||} = 0.101$ eV, $t_9^{||} = -0.042$ eV, and $t_{10}^{||} = 0.073$ eV are taken for the intralayer hopping parameters, and $t_1^{\perp} = 0.524$ eV, $t_2^{\perp} = 0.180$ eV, $t_3^{\perp} = -0.123$ eV, $t_4^{\perp} = -0.168$ eV, and $t_5^{\perp} = 0.005$ eV for the interlayer hopping parameters, as depicted in Figures 22 (b) and 22 (c), respectively. Concerning the theoretical obtaining procedure of the hopping parameters, it is worth mentioning that, in general, the band structure is initially calculated by means of first-principles methods, and then a search is done for the hopping parameters that best fit the energy bands obtained by the tight-binding method to those obtained by the first-principles calculations (Araujo *et al.*, 2012), in a similar way as done in the Wannierization procedure of density functional theory (Garrity; Choudhary, 2021). For instance for multilayer BP, a study performed a similar procedure based on first-principles calculations and reported in Rudenko & Katsnelson (2014a) the hopping parameters for modeling BP structures by using 5 intralayer hoppings whereas in 2015 reported in Rudenko, Yuan & Katsnelson (2015) a more accurate model with 10 intralayer hoppings that fit more properly the BP band structure obtained via first-principle calculations.

6.3 Band structure unfolding

Here, we present the band unfolding technique to recover an effective primitive cell picture of the band structure of multilayer phosphorene within the supercell approach. The main idea behind such a computational method is to map the energy eigenvalues obtained from large supercell calculations into an effective band structure, as shall be briefly presented here (Medeiros *et al.*, 2014; Popescu; Zunger, 2010). For defect-free lattice structures, the band unfolding technique for supercell cases provides a strictly exact solution similar to the ones for primitive cells. However, under the influence of perturbations the wave vector is no longer

a good quantum number, and consequently, the primitive approach is no longer appropriate. Therefore, owing to the study of electronic properties of realistic systems, where defects are almost always inevitable, a modeling that considers the effects of defects is required, especially when the defect size is larger than the lattice parameters of the primitive cell. The developments of the theoretical and computational basis of the modern supercell unfolding algorithms are scientifically credited to the researchers Ku *et al.* (2010), Popescu & Zunger (2010), Popescu & Zunger (2012), and Boykin & G. (2005), Boykin *et al.* (2007), Maspero *et al.* (2016). Such a technique overcomes technical issues in the previous methodologies, for instance, the need to discard fluctuations at the outset (Chen; Sher, 1995; Shan *et al.*, 1999; Faulkner; Stocks, 1980) and the inconvenient folding of the energy bands into the smaller supercell Brillouin zone with complicated band interpretation even for relatively small supercells, although the equivalence between the primitive cell and the supercell descriptions of a perfectly periodic material.

The use of the band unfolding technique to explore the electronic properties of 2D materials has also been recently reported, as presented in Medeiros *et al.* (2014), Medeiros *et al.* (2015) and Nishi *et al.* (2017) for defective graphene and twisted bilayer graphene, respectively. To our knowledge, Babar *et al.* (2018) is the only found work in the literature to date with the closest methodology to ours in the investigation of defects in BP. However, Babar *et al.* (2018) investigation focus was on the intrinsic, robust, and high-temperature Kondo state in 2D semiconducting phosphorene induced by substitution of Cr atom in the BP lattice. Moreover, their calculations were based on spin-polarized density functional theory within the projector augmented-wave formalism, combined with a Hubbard-like on-site Coulomb interaction with resulting electronic band structures for the supercells being unfolded by the band-unfolding technique implemented in the *BANDUP code* (Medeiros *et al.*, 2014; Medeiros *et al.*, 2015). It is important to point out that no tight-binding results for point defects (mono, double and triple vacancies) in multilayer BP were discussed in their work.

Within the theoretical framework based on the supercell approach to investigate the role of defects on the electronic band structure of 2D materials, one needs to take supercells large enough to prevent defects from interacting with their replicas. However, the resulting supercell Brillouin zone (with volume Ω_{SBZ}) is much smaller than the primitive cell Brillouin zone (with volume Ω_{PBZ}), *i.e.* $\Omega_{SBZ} < \Omega_{PBZ}$, generating a dense set of energetic curves that is hard to extract meaningful physics. Nonetheless, the electronic states obtained in the supercell and in the primitive cell Brillouin zones pictures form a complete basis set, and thus, any state in

a given of such representations can be expanded as a linear combination of the other subset so that the supercell Brillouin zone states can be projected in the primitive cell Brillouin zone ones. More specifically, for each supercell Brillouin zone wave vector $\mathbf{K}$ there are $N = \Omega_{PBZ}/\Omega_{SBZ}$ wave vectors $\mathbf{k}_i$ in the primitive cell Brillouin zone, such that

$$\mathbf{k}_i = \mathbf{K} + \mathbf{G}_{\mathbf{k}_i \leftarrow \mathbf{K}}, \quad i = 1, 2, ..., N, \tag{6.2}$$

where the vectors $\mathbf{G}_{\mathbf{k}_i \leftarrow \mathbf{K}}$ belong to the supercell reciprocal lattice. A given supercell state $|\mathbf{K}, m\rangle$, where m is the band index, can be written as a linear combination of the primitive cell states $|\mathbf{k}_i, n\rangle$ as

$$|\mathbf{K}, m\rangle = \sum_{\{\mathbf{k}_i\}, n} a(\mathbf{k}_i, n; \mathbf{K}, m) |\mathbf{k}_i, n\rangle. \tag{6.3}$$

We can also analyze the eigenstates of the supercell as their projections onto the base of the eigenstates of the primitive cell and, thus, write it as

$$|\mathbf{K}, m\rangle = \sum_{i,n} |\mathbf{k}_i, n\rangle \langle \mathbf{k}_i, n | \mathbf{K}, m\rangle, \tag{6.4}$$

with the eigenstates $|\mathbf{k}_i, n\rangle$ obeying the completeness and normalization conditions. From the definitions of Eqs. (6.3) and (6.4), it is easy to see that the state basis to form the supercell eigenstates is the one in which these are projected onto the primitive cell with probability given by

$$\begin{aligned} P_{\mathbf{K},m}(\mathbf{k}_i) &= \sum_n |\langle \mathbf{K}, m | \mathbf{k}_i, n \rangle|^2 \\ &= \sum_n |a(\mathbf{k}_i, n; \mathbf{K}, m)|^2. \end{aligned} \tag{6.5}$$

This relation is named as the spectral weight. The sum over all probabilities into the primitive cell, *i.e.* overall $\mathbf{k}_i = \mathbf{K} + \mathbf{G}_i$, where $i = 1, 2, ..., N$, will be 1. The spectral function $\mathbf{F}(\mathbf{k}_i, E)$ is defined as

$$\mathbf{F}(\mathbf{k}_i, E) = \sum_m P_{\mathbf{K},m}(\mathbf{k}_i) \delta(E - E_m). \tag{6.6}$$

Equation (6.6), which includes only $\mathbf{k}_i$ that obeys $\mathbf{k}_i = \mathbf{K} + \mathbf{G}_i$, gives us the energy spectrum of unfolded supercell systems in the primitive cell Brillouin zone, *i. e.* the band structure of the supercell projected in the primitive cell. For a perfect crystal, the spectral function of a supercell results in the exact band structure of the primitive cell. This can be verified for the pristine multilayer phosphorene case in Figure 16 (d), where we show (left panels) the primitive

Brillouin and (right panels) the supercell Brillouin zones states for (first row) monolayer, (second row) bilayer, and (third row) trilayer cases in the absence of any type of defect. Here, we assumed a 6×6 size supercell in order to get a full agreement between the primitive and spectral phosphorene band structures, especially around the region of interest at low energies and close to the Γ-point. The role of the supercell size in the agreement between the different primitive and supercell pictures shall be discussed in detail even in the presence of defects in the next section (Sec. 6.4). It is possible because the spectral function also allows for analyzing defective systems providing a meaningful physical representation for it when lattice deviations from the perfect crystal structures are small.

6.4 Results and discussions

6.4.1 Defects in monolayer phosphorene

In this subsection, we investigate the effects of defects created by removing one or more atoms from the BP supercells on the unfolded band structure of monolayer phosphorene obtained within the supercell approach described in Sec. 6.3. Our investigation is performed for low-density cases of vacancies considering seven different configurations of point defects by removing one, two, or three phosphorus atoms of the supercell, as well as by keeping and/or not the sublayer (inversion) symmetry and sublattice symmetry. The latter characteristic is concerning the equivalence of the A/D and B/C missing phosphorous atoms in upper and lower atomic sublayers, due to the D_{2h} symmetry of phosphorene. Therefore, for the $n > 1$ case of missing atoms, one can have symmetric and asymmetric intrinsic defects, being categorized into symmetric when one removes n atoms belonging to identical sublattices at the same sublayer or equivalent sublattices A/D or B/C in different sublayers, otherwise, it is characterized as asymmetric. Such defective atomic arrangements for a 6×6 supercell are shown in the left panels of Figure 17 for monovacancy (MV) and of Fig. 18 for divacancy (DV) and trivacancy (TV) cases. For all the studied cases, we assume that the vacancies are located in the center of the supercell in order to reduce the interactions between their copies in the neighbor supercells. It is important to mention that the investigated defective structures here are rigid, in the sense that no lattice reconstruction is considered due to one or more atoms being removed, i.e. no relaxation and no passivation of the BP structures around the vacancies are assumed, which would provide additional modifications in the observed electronic properties. Relaxed structural

configurations of bilayer BP in the presence of vacancies were investigated in Kripalani *et al.* (2019), as well as in Kundu, Naik & Jain (2020), Wang *et al.* (2015) in the presence of both vacancies and self-interstitial defects in few-layer phosphorene, for example. Before

Figure 17 – (a) Crystallographic structure of a 6×6 monolayer phosphorene supercell in the presence of a monovacancy (MV). (b) Projected band structure (spectral function) in the primitive Brillouin zone by taking 2×2, 4×4, and 6×6 supercells (from left to right) within the supercell band unfolding picture. (c) Folded phosphorene band structure calculated using a 6×6 supercell solely with the tight-binding model.

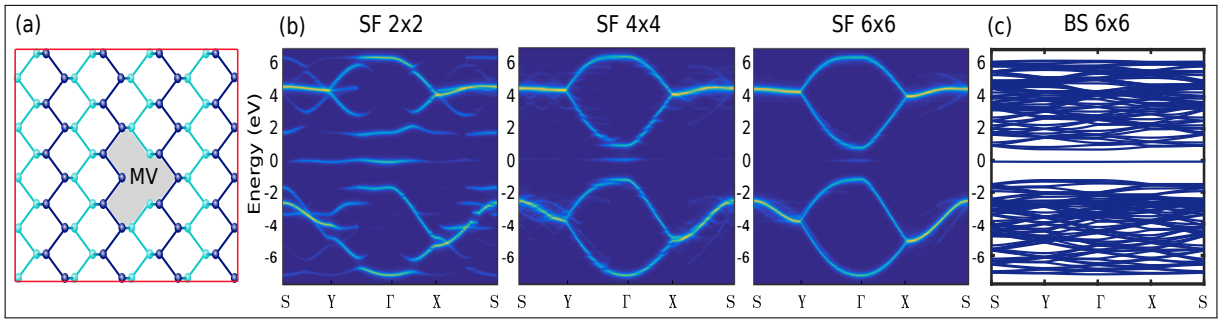

Source: Figure elaborated by the author (2023).

describing the monovacancy effects induced in the BP lattice, let us briefly discuss the role of the supercell size within the unfolded band structure picture. Note that an appropriate choice for the supercell size is one that shall avoid interactions between the copies of the defects in neighboring supercells, which would occur due to the long-range interaction between atoms in phosphorene (Rudenko; Yuan; Katsnelson, 2015). For this purpose, we calculated the phosphorene band structure in the presence of a monovacancy by increasing the supercell size until we observed a good agreement between the bulk states of the unfolded BP band structure for the defective case and the primitive Brillouin zone band structure for the non-defective case, as well-known in the literature (Rudenko; Katsnelson, 2014a; Rudenko; Yuan; Katsnelson, 2015; Jr; Katsnelson, 2015; Sousa *et al.*, 2017a). Carrying out this analysis, we can observe band structure instabilities after the unfolding procedure for small supercells, as depicted in Figure 17 (b) by comparing panels (from left to right) for 2×2, 4×4, and 6×6 supercells, being the latter the less affected. Therefore, from now on we assume a supercell with a 6×6 size for investigating the states associated with point defects in multilayer BP, considering that this is the smallest stable configuration found in the presence of defects in monolayer BP.

From Figures 17 (b) and 17 (c) for 6×6 supercell unfolded and folded band structures, respectively, one notices that: (i) the presence of a monovacancy in the crystalographic BP lattice is responsible for creating a quasi-flat mid-gap defect state located at $\approx$ 0.60 eV below the

unfolded conduction band with a high intensity around the Γ-point in the reciprocal space. The emergence of such a quasi-flat state is due to the sublattice symmetry breaking caused by the imbalance in the number of equivalent sublattices by one P atom removal, *i.e.* $N_{A/D} \neq N_{B/C}$. The presence of such a defective state is typical of deep-level localized defects (Kishimoto; Okada, 2016; Ovdat *et al.*, 2020; Kotakoski *et al.*, 2011; Lee *et al.*, 2005; Palacios *et al.*, 2008; El-Barbary *et al.*, 2003; Hahn; Kang, 1999; Li *et al.*, 2015; Zhang; Wu; Yang, 2016; Lei *et al.*, 2017b; Lei *et al.*, 2017a; Kistanov *et al.*, 2016; Smotlacha; Pincak, 2018; Sun *et al.*, 2018; Arra; Babar; Kabir, 2019; Li; Peeters, 2018; Dai *et al.*, 2017; Kiraly *et al.*, 2017; Harsh *et al.*, 2022; Huang *et al.*, 2022; He *et al.*, 2019; Zhan *et al.*, 2019; Li *et al.*, 2022; Aghajanian; Mostofi; Lischner, 2022; Fang *et al.*, 2022; Rijal *et al.*, 2021; Rezaei *et al.*, 2021; Gupta; Periasamy; Narayanan, 2021; Yao *et al.*, 2020; Pei *et al.*, 2020; Kundu; Naik; Jain, 2020; Wang *et al.*, 2015; Kripalani *et al.*, 2019; Shah *et al.*, 2019; Cai *et al.*, 2019; Amini *et al.*, 2019a; Amini *et al.*, 2019b; Riffle *et al.*, 2018; Cai *et al.*, 2016; Gaberle *et al.*, 2018; Hu *et al.*, 2015; Farooq *et al.*, 2015); (ii) no-strong effect is observed in the monolayer BP bulk states in the presence of a monovacancy, such that the anisotropic dispersion along the armchair and zigzag directions is preserved. From the dimensions of the smallest stable supercell in the presence of point defects, *i.e.* $(L_x, L_y) = (Ma_x, Na_y)$ with $M = N = 6$, and a_x and a_y associated with the BP lattice parameters a_1 and a_2 in real space, one can estimate that defects located at a distance smaller than ≈ 3 nm shall interact with their neighboring copies and consequently should present changes in the energy spectrum, as the ones verified in left and middle panels of Figure 17 (b), that in turn shall modify the optoelectronic properties of the system.

For double vacancy defects, we consider three possibilities for the lattice-removal arrangements (Li; Peeters, 2018): (i) divacancy of type I (DV1), when we remove two neighbor atoms from different sublayers, for instance as shown in the left panel of Fig. 18(a) by removing sublattices A and C (or B and D), (ii) divacancy of type II (DV2), when one removes two neighbor atoms from the same sublayer, for instance as shown in the left panel of Figure 18 (b) by removing sublattices A and B (or C and D), and (iii) divacancy of type III (DV3), which occurs when two P atoms far apart are removed from the supercell, as illustrated in the left panel of Figure 18 (c). In this situation, different combinations for P atoms removal could be assumed, being the two P atoms removed from equivalent sublattices ($A-D$, $B-C$) with other four combinations belonging to the same sublattices ($A-A$, $B-B$, $C-C$, $D-D$), or from non-equivalent sublattices ($A-B$, $A-C$, $D-B$, $D-C$). Although DV3 defects can be seen as a double monovacancy

Figure 18 – (left) Crystallographic structure of the different types of vacancies in monolayer phosphorene, namely, (a) DV1, (b) DV2, (c) DV3, (d) TV1, (e) TV2, and (f) TV3. (middle) Projected band structures (spectral function) in the primitive Brillouin zone and (right) folded phosphorene band structures calculated solely using the tight-binding approach by taking a 6×6 supercell. Enlargements are shown as insets in the right panels in order to emphasize the mid-gap states for each defective case around the Γ point.

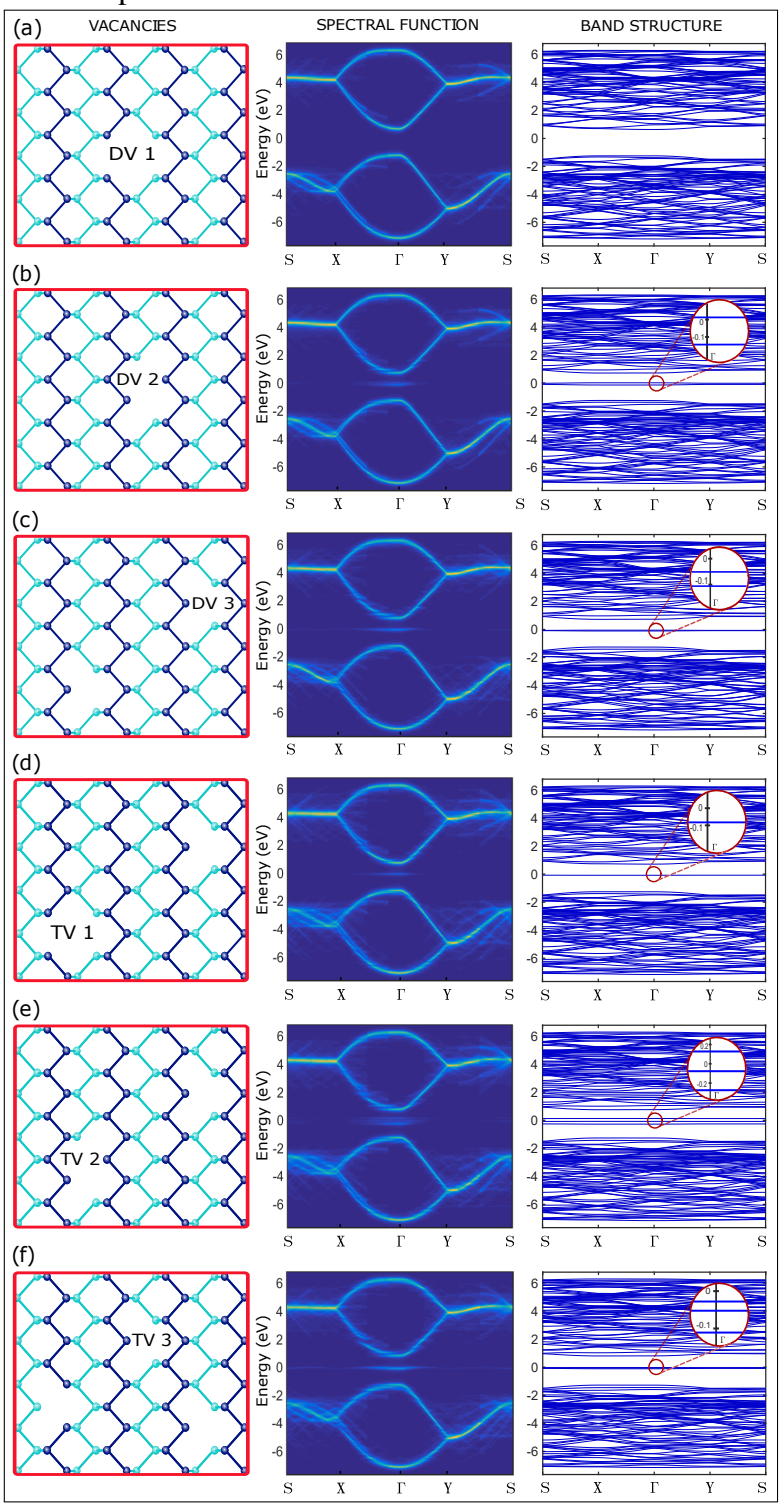

Source: Figure elaborated by the author (2023).

inside the supercell, in fact, its structural nature differs from the isolated monovacancies in the supercell interacting with its copy in the neighbor cell, owing to the interaction distance between the defects, being much smaller for the case of isolated monovacancies. Concerning the sublattice and sublayer (inversion) symmetries in the defect formation defined in terms of the number of removals of different sublattice atoms in the same or different sublayers, note that DV1 and DV2 cases correspond to the symmetric and asymmetric cases, respectively, *i.e.* for the DV1 (DV2) defect the two removed atoms belong to (non-)equivalent sublattices, preserving (breaking) the sublattice symmetry of BP lattice, such that $N_{A/D} = N_{B/C}$ ($N_{A/D} \neq N_{B/C}$). In addition, DV2 defects break the inversion symmetry, since the two removed atoms belong to the same layer creating a layer imbalance, *i.e.* $N_A + N_B \neq N_C + N_D$. The unfolded and folded monolayer band structures in the presence of divacancies for the three defective investigated cases (DV1, DV2, and DV3) are shown in the middle and right panels of Fig. 18, respectively. From that, one notices that DV1 defects do not create a mid-gap state, and no significant changes are observed in the monolayer BP band structure [see Figure 18 (a)]. This happens because of the crystal symmetry that is maintained (Zhang; Wu; Yang, 2016; Li; Peeters, 2018): both sublattice and sublayer (inversion) symmetries are preserved due to the balance of sublattices in both BP layers ($N_A + N_B = N_C + N_D$ and $N_{A/D} = N_{B/C}$). For the DV2 case [see Figure 18 (b)], as a consequence of the breaking of both sublattice and inversion symmetries, mid-gap states are present in the monolayer BP band structure. Analyzing the bandwidth of this mid-gap state in the band structure of the primitive cell [right panel in Figure 18 (b)] in comparison to the one for monovacancy shown in Figure 18 (c), this reveals to us the existence of two defective states, as depicted in the enlargement in the right panel in Figure 18(b). This is due to a double P atoms removal, being one corresponding state per atom removal. From Figure 18 (c) for the DV3 case, one also observes the appearance of mid-gap states, similar to the DV2 case, except that now, for the DV3 case, it is an even closer two quasi-fold degenerate defective states. The difference between the two defective mid-gap states in DV2 and DV3 cases is of ≈ 0.22 eV and ≈ 0.05 eV, respectively. These values were graphically verified by taking the maximum and minimum values of the bandwidth of the defective bands in the spectral bands for the unfolded states and not the energy difference in the folded defective bands as shown in the enlargements of each spectrum. It is worth highlighting about the geometrical form of the considered DV3 defect in Figure 18 (c). From all the possibilities discussed in the previous paragraph for the DV3 formation, one assumes the one where the two atoms are removed from the same sublattice.

Therefore, one would expect a two-fold degeneracy for the vacancy-bound states lying inside the gap region. However, keep in mind that when the number of vacancies increases in the supercell, the inter-vacancy distance decreases and thus the localized wavefunctions on two adjacent vacancies positions can overlap, lifting the degeneracy of the states, as we observed of ≈ 0.05 eV for the double monovacancy in the DV3 case.

In order to validate and compare our results obtained via tight-binding model for divacancies with those reported in the literature (Hu *et al.*, 2015; Babar *et al.*, 2018) by performing first-principles calculations, it is important to mention that Hu *et al.* (2015) showed that divacancies, labeled there as DV-(5|8|5)-1, DV-(555|777), and DV-(4|10|4) associated with the defect formation being equivalent to our DV1 type [see Figure 18 (a)], have little effect on phosphorene's electronic properties such that defective phosphorene monolayers still show semiconducting with similar band gap values to perfect phosphorene, whereas divacancies of type DV-(5|8|5)-2, similar to our DV2 type [see Figure 18 (b)], can introduce unoccupied localized states into phosphorene's fundamental band gap. Both reported statements in Hu *et al.* (2015) are in full agreement with our results as shown in Figures 18 (a) and 18 (b).

Reference Babar *et al.* (2018) reported the emergence of such a mid-gap state in the unfolded band structure with Cr impurity absorbed at the divacancy of the monolayer and bilayer phosphorene. Moreover, similarly to our results for intrinsic point defects, they found that the position of the Cr impurities in bilayer phosphorene plays an important role in the electronic features that may lead to a phase transition transforming the semiconducting electronic band to a metallic band structure, due to a defect-induced band touching between the defective state and the conduction band.

Following the divacancy formation's discussion, let us now consider the case with a slightly increasing in the concentration, *i.e.* taking the case of trivacancies. The increase in vacancy concentration allows us to consider combined situations of defects. For trivacancies, they can be formed by: one monovacancy and one divacancy of type I (DV1), labeled as TV1 [see left panel of Figure 18 (d)], one monovacancy and one divacancy of type II (DV2), labeled as TV2 [see left panel of Figure 18(e)], three different monovacancies, labeled as TV3 [see left panel of Figure 18 (f)], or even by increasing the coalescence, similarly to nano-holes/nano-pores/antidots, as reported in Lei *et al.* (2017a), Sun *et al.* (2018). The role of the coalescence of the point defects in the electronic band structures within the unfolded picture for high vacancy concentration is not considered here.

The middle and right panels of Figures 18 (d), 18 (e), and 18 (f) show the unfolded and folded band structures in the presence of trivacancies for the three defective investigated cases (TV1, TV2, TV3), respectively. Analyzing the band structure in the presence of a TV1 defect [Figure 18 (d)], one notices only one defective state lying inside the gap, whose emergence in the band structure can be explained by the crystallographic formation of the TV1 defect and by the previous results for monovacancy and divacancies. Knowing that TV1 defects are formed by a combination of a monovacancy and a DV1 defect, where the latter [Figure 18 (a)] does not create a mid-gap state due to the conservation of the lattice symmetry and, on the other hand, the former [Figures 17 (b, c)] holds a defective state owing to the breaking of both sublattice and sublayer symmetries, it was natural to expect the appearance of only one mid-gap defective state corresponding to the monovacancy. Therefore, energetically speaking, one can state that the TV1 defect induced in a monolayer BP is energetically equivalent to the monovacancy case. For the TV2 defective case [Figure 18 (e)], three defect bands appear in the mid-gap with an energetic separation of the order of ≈ 0.15 eV between adjacent quasi-flat bands. Two of them are originated from the DV2 defect [see Figure 18 (b)] and one of them comes from the monovacancy [see Figures 17 (b, c)]. This is due to the fact that both MV and DV2 defects, that compose the TV2 defect, break the sublayer and sublattice symmetries of monolayer BP. Observing the consequences of a TV3 defect in BP lattice shown in Figure 18 (f), one notes that the combination of three monovacancies composing a TV3 defect gives rise to a quasi-three-fold degenerate state, one state per P atom removal. By comparing the cases formed by multiplies monovacancies: the monovacancy itself [Figure 17 (b)], the divacancy of type III [DV3 - Figure 18 (c)], and the trivacancy of type III [TV3 - Figure 18 (f)], we observe an increase in the density of states around the Fermi energy in the middle of the gap due to the *n*-fold quasi-degeneracy induced by the multiple *n* monovacancies.

6.4.2 Defects in multilayer phosphorene

So far, the obtained results in the previous section for monolayer BP suggest that an energy bands control, such as the degeneracy and the energetic position of the defective bands, can be achieved by playing with the concentration of defects and its structural lattice formation, like the type and position of the vacancy, which agrees with the previously reported works (Li *et al.*, 2015; Zhang; Wu; Yang, 2016; Kistanov *et al.*, 2016; Li; Peeters, 2018). In addition to the discussed defect-induced controlling of the phosphorene band structure, in this section

we investigate the layer degree of freedom in the defect formation, assuming the same types of point defects with one, two, and three removed *P* atoms as in Sec. 6.4.1, but now taking this removal from different BP layers. We shall focus our discussion on defective multilayer phosphorene systems with two and three layers for the monovacancy case and the defective di- and tri-vacancies of type II, where one has mid-gap states, *i.e.* for the cases with breaking of the sublattice and/or sublayer symmetries. The lowest-energy spectrum for bilayer phosphorene in the presence of monovacancy, divacancy of type II, and trivacancy of type II are presented in Figures 19 (a), 19 (b), and 19 (c), respectively. Three different configurations associated with the position of the atomic removals in the point defect formation were assumed for each case. The energy values at the Γ-point of the bottom of the conduction band, the top of the valence band, and the maximum and minimum values of the defective states bandwidth of the unfolded band structures are presented when one removes *P* atoms in one of the layers or in both layers, as sketched by the brightest layers in the side view of the bilayer BP structures located below panels (a) to (c) in Figure 19. For comparison, Figures 19 (a) - 19 (c) also display the non-defective bilayer results in solid green and black lines for the top and the bottom of the valence and conduction bands, respectively, as well as the obtained values (dashed gray lines) from the spectral energy bands discussed in the previous section for the monolayer BP defective bands in the presence of vacancies. In general speaking, concerning the defective bands [red triangles in Figure 19 (a-c)], one can observe that: (i) defects induced in both layers in the bilayer system exhibit the larger defective bandgap width when compared to the one-layer defective case formation and also to the defective monolayer case (dashed gray lines); (ii) the cases where *P* atoms are removed at just one of the layers present energy levels that are only slightly different when comparing removals in the bottom and top layers, displaying a slightly lower defect bandgap width when the vacancy is formed in the lower sublayer, and (iii) the defective bandgap width in these one-layer defective cases are even smaller than the monolayer defective case. The latter can be explained by keeping in mind that multilayer phosphorene has a tunable bandgap width with the number of BP layers, exhibiting a smaller bandgap width the greater the number of stacked BP layers. Consequently, in general, it was already expected for a certain defect type that the defective bands in a bilayer system would be closer than in a monolayer situation for the same induced defect type since the bilayer BP bandgap is smaller than the monolayer one in the pristine case. Thus, in turn, removing *P* atoms in just one of the layers some hoppings are turned off, leading to an energetic reduction of defective bandgap

Figure 19 – Energetic position at the Γ-point of the unfolded lowest-bands around the Fermi energy in the presence of (a, d) a monovacancy (MV), (b, e) a divacancy of type II (DV2), and (c, f) a trivacancy of type II (TV2) in the (a, b, c) bilayer and (d, e, f) trilayer phosphorene. Black [blue] squares, down and up red [pink] triangles, and green [olive] circles correspond to the bottom of the conduction band (CB), the top and bottom mid-gap defective bands (DB), and the top of the valence band (VB) in the bilayer [trilayer] band structure, respectively. For better visualization, the middle defective states in the energy scale are omitted in the TV2 case in panels (c) and (f). Three [four] configurations in the defect formations are shown along the horizontal axis in each panel with its respective band structures at the bottom of panels (a-c) for bilayer and in panel (g) for trilayer case. The brightest crystallographic layers in the illustrations at the bottom of the panels denote the defective atomic layers. Solid black [blue] and green [olive] lines are associated with the bottom and top of the conduction and valence bands at the Γ-point of the unfolded spectral bands, respectively, for the defect-free bilayer [trilayer] system. Black dashed lines represent the energetic position of the defective bands for these point defects induced in a monolayer phosphorene.

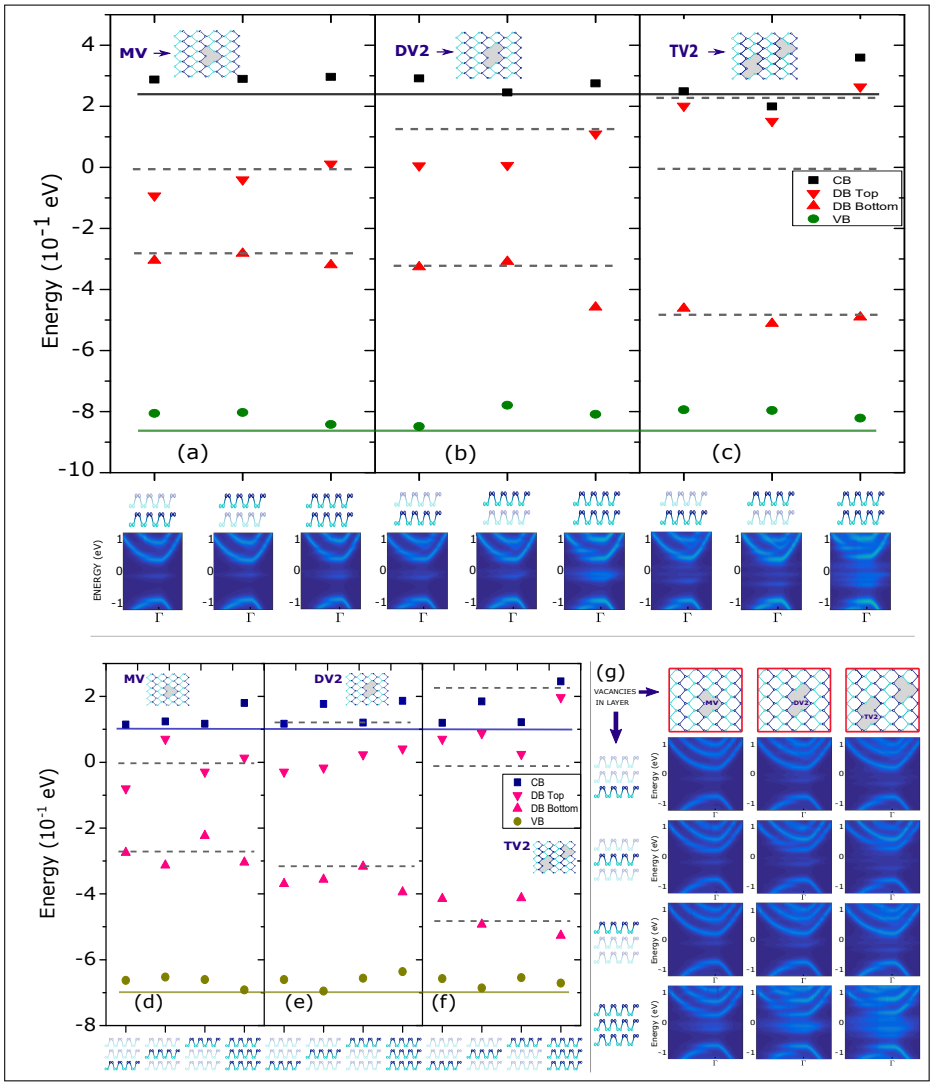

Source: Figure elaborated by the author (2023).

width. Note that this defective bandgap reduction roughly holds true for all results of one-layer defective bilayer BP cases for the left and middle data in Figures 19 (a) - 19 (c).

Statements (i) and (ii) can be understood in an intuitive energetic way based on the five interlayer hoppings tight-binding model assumed here (see Sec. 6.2). From Figure 16 (c), one can realize that only one among the five interlayer hoppings, namely $t_5^{\perp}$, corresponds to connections between sublattices belonging to the lower sublayer of the bottom layer with the sublattices belonging to the top layer. In this way, defects created in the lower sublayer will have a less pronounced interlayer energetic effect than defects created in the upper sublayer when the defective sublayer is located at the bottom of the sample, since *P* atoms removed from the lower sublayer will turn off fewer interlayer hoppings than defects created in the top sublayer. This explains [statement (ii)] why the configurations where the vacancy is formed in the lower sublayer display a slightly lower defective bandgap width when compared with the case where the vacancy is formed in the upper sublayer, being due to the number of turned-off interlayer shopping. Note that, when the defective layer is in the bottom sublayer, only the $t_5^{\perp}$ interlayer hoppings will be turned off, while in the case of the defective layer being in the top sublayer, not only the $t_5^{\perp}$ interlayer hoppings will be turned off, but also the $t_1^{\perp}$ to $t_4^{\perp}$ interlayer hoppings. And indeed that is the case here, being the monovacancy created by removing a *P* atom from the lower sublayer in the BP system, the DV2 divacancy by removing two non-equivalent sublattices in the lower sublayer, and the TV2 trivacancy composed by a monovacancy and a DV2 divacancy.

Two physical insights can be given to explain statement (i). One of them is concerning the number of turned-off interlayer hoppings. By the energetic view, the more *P* atoms are removed from both BP layers in the bilayer system, the more and more $P-P$ interlayer bonds are turned off and consequently the lower the interaction between the sublayers, leading to a greater energetic distance between the defective bands. The second physical insight is related to the localization of the wave function of such point defect states. In defective 2D systems, it is well-known that the probability amplitudes of such defective states are preferably located in the vicinity of the missing atoms, as reported for graphene (Kishimoto; Okada, 2016; Ovdat *et al.*, 2020; Kotakoski *et al.*, 2011; Lee *et al.*, 2005; Palacios *et al.*, 2008; El-Barbary *et al.*, 2003; Hahn; Kang, 1999) and phosphorene (Smotlacha; Pincak, 2018; Sun *et al.*, 2018; Li; Peeters, 2018; Amini *et al.*, 2019b). Keeping that in mind and also knowing that defects here created in both layers are formed by removals of *P* atoms from the same sublattice belonging to a certain sublayer in the two, top and bottom, BP layers, it is expected a greater repulsion of the wave

functions distributed in each layer being greater the more P atoms are removed. Thus, more energetically stable defective levels must have slightly higher energies as compared to the case when one removes P atoms of just one layer.

In addition to the observations discussed previously on the defective bilayer spectra in Figures 19 (a) - 19 (c), also note that the situation of monovacancy in Figure 19 (a) in which one atom of P is removed from each sublayer of the bilayer BP will correspond to the divacancy case, as in fact it is confirmed by comparing the data on the right side of Figure 19 (a) with the data on the left side of Figure 19 (b), where they have the same energy values for the defective and bulk bands. Furthermore, giving quantitative features of the bilayer energy spectra in the presence of defects, by comparing Figures 19 (a) - 19 (c), one observes that: the defective bandgap widths range from ≈ 0.24 eV for one-layer induced monovacancy case to ≈ 0.85 eV for the TV2 trivacancy in the case where the defects are equally distributed in both layers; the energy difference between the defective states in the monovacancy case shown in Figure 19 (a) ranges between ≈ 0.15 eV for vacancies distributed in a single layer of the bilayer BP and ≈ 0.30 eV for the equally distributed vacancy case, being the top defective band located between ≈ 0.42 eV and ≈ 0.30 eV below the conduction band, respectively; for the DV2 divacancy case [Figure 19 (b)] with the defect distributed just in one of the layers, one has that the top mid-gap states are located at ≈ 0.25 eV below the conduction band with an average energy separation of ≈ 0.30 eV, while for the equally distributed defect in both layer the highest defective state is at ≈ 0.13 eV below the conduction band; and the energetically highest defective state in TV2 trivacancy case is just a few tens of meV below the conduction band. Concerning the bulk states, Figures 19 (a) - 19 (c) show that the maximum valence-conduction energy value difference is ≈ 1.13 eV, corresponding to the TV2 case with the defect distributed in both layers.

Figures 19 (d) - 19 (f) show similar results as the ones in Figures 19 (a) - 19 (c), but now for point defects created in trilayer BP systems. In the trilayer BP system, one has more layer combination possibilities for the defect's spatial distributions that can be created in only one or two of the three layers or even in the three BP layers. We present results for monovacancy [Figure 19 (d)], DV2 divacancy [Figure 19 (e)], and TV2 trivacancy [Figure 19 (f)] focusing on the situations where point defects are formed in just one (bottom, middle, or top) of the three BP layers or equally distributed in all the three BP layers, as indicated by the brightest crystallographic layers in the illustrations below each panel of Figures 19(d)-19 (f). In general, note that analogously to the bilayer results, the energetic positions of the valence,

conduction, and defective bands strongly depend on the vacancy type and concentration, as well as on how the defects are distributed per layer. Also here, the higher the defect concentration, the larger the defective bandgap width, especially for cases where the vacancies are equally distributed in all three layers, as can be seen in the unfolded band structures shown in Figure 19 (g). It is very interesting to note that the defective bands are shifted upward when the defect is located in the middle layer, regardless of the defect type [see second columns of data in each panel of Figures 19 (d)-19 (f)]. This can be understood by the number of turned-off interlayer hoppings, since the middle layer is adjacently connected to the top and bottom layers, being energetically responsible for more interlayer connections. Quantitatively speaking, the minimum and maximum values found in trilayer results for the defective bandgap width are of the order of ≈ 0.19 eV for the monovacancy case with the vacancy located at the top layer, as can be seen in Figure 19 (d), and of ≈ 0.72 eV for the TV2 trivacancy with the vacancies equally distributed in the three BP layers, as shown in Figure 19 (f), respectively. Similar to the bilayer case, results for one-layer distributed DV2 divacancy in a trilayer BP system [Figure 19 (e)] exhibit approximately the same defective bandgap width (here of ≈ 0.33 eV) regardless of whether it is located on the bottom, middle, or top layer. The unfolded band structures in Figure 19 (g) show that the higher the vacancy concentration, one observes the increase in the bandgap width and an approximation between the defective and bulk states, indicating that large concentrations could lead to a transition from semiconductor to metal in multilayer phosphorene system due to defects. Such semiconductor-to-metal transition was already reported in Figure 19 (a)-(f) in the bilayer BP system due to a defect-induced band touching between the defective state and the conduction band, as mentioned in the previous section.

6.5 Conclusions

We have calculated the band structures of defective multilayer phosphorene (monolayer, bilayer, and trilayer), by means of a supercell approach with periodic boundary conditions, assuming different types of point defects distributed in the same or different BP layers. For that, we projected the band structure of the supercell into the Brillouin zone of the unit cell in order to have a clear picture of the effects of the vacancies on the unfolded recovered energy bands. Such a presented theoretical framework based on the combination of the tight-binding model and the band unfolding technique allowed us to determine the appropriate size of the supercell for defective BP systems. Our results showed that a 6×6 supercell is able to recover

the effective and expected BP band structure when one considers low vacancy densities on the BP lattice. It is worth mentioning that previous theoretical approaches (Li *et al.*, 2015; Zhang; Wu; Yang, 2016; Kistanov *et al.*, 2016; Dai *et al.*, 2017; Kundu; Naik; Jain, 2020; Wang *et al.*, 2015; Kripalani *et al.*, 2019; Cai *et al.*, 2019; Hu *et al.*, 2015; Farooq *et al.*, 2015) that dealt with intrinsic defects in the BP lattice structure did not employ the unfolding of the bands combined with the tight-binding model and consequently, no systematic discussion concerning the defect's effects on the band structures could be clearly stated, as presented here, presenting them in general solely indirect results such as densities of states and local densities of states in the presence of defects.

Concerning the presence of defects, we showed that a monovacancy in monolayer phosphorene induces a mid-gap state energetically located ≈ 0.30 eV below the conduction band, presenting a non-dispersive character and a negligible effect on the bulk bands. Interestingly, a DV1-type double vacancy does not create a mid-gap state because the sublattice symmetry is not broken when we remove equivalent atoms in different sublattices. For the DV2 and DV3 cases, two mid-gap states appear very close to each other, with an energetic difference between these defective states, *i.e.* a defective bandgap width, of ≈ 0.22 eV and 0.05 eV for the DV2 and DV3 cases, respectively. The emergence of such defective mid-gap states is due to the breaking of the sublattice symmetry and/or sublayer (inversion) symmetry of the system. We observed that the results for trivacancies can be understood as the interplay effects induced by monovacancy and divacancy in the BP band structure. In addition to the vacancy type and concentration, the results discussed for defects distributed in the bilayer and trilayer BP systems indicated that adding layers is another way to control the energetic position and bandgap width of the defective bands.

Finally, our investigation showed that the unfolding formalism is clearly able to exhibit the defective band structure of multilayer phosphorene and that the presence of defects can be useful to control the electronic and optoelectronic properties of a few phosphorene layers by changing the type, concentration, and layer distribution of the vacancies.

7 PHOSPHORENE NANORIBBONS BY BAND UNFOLDING FORMALISM

7.1 Motivation

As seen before in the section 1.1.1, PNRs have been widely studied by theoretical methods (Lee *et al.*, 2015b; Sorkin *et al.*, 2017; Guo *et al.*, 2014; Carvalho *et al.*, 2014; Hu *et al.*, 2017; Nourbakhsh; Asgari, 2016; Das *et al.*, 2016; Yang *et al.*, 2016; Sisakht *et al.*, 2016; Wu *et al.*, 2016; Poljak; Suligoj, 2016; Yang *et al.*, 2016; Wu *et al.*, 2015; Zhang *et al.*, 2014; Yao *et al.*, 2015) while its experimental production is still taking its first steps in recent years (Watts *et al.*, 2019; Pacchioni, 2019; Yu *et al.*, 2021; Abu *et al.*, 2022). PNRs draw attention since their emergence as a material applicable to electronic devices, attracting significant attention from researchers due to their fascinating characteristics arising from the distinctive 2D structure of phosphorene and the added quantum confinement resulting from the nanoribbon boundaries. This exploration of PNRs presents a novel approach for developing materials with enhanced electronic and optoelectronic properties, opening up exciting possibilities for various applications. However, its experimental extraction has only emerged in recent years and the production of this material with hight-quality is still a challenge.

Experimentally, high-quality nanoribbons have been produced by Watts *et al*.. Through the implementation of a top-down approach, a remarkable outcome is achieved in the form of stable liquid dispersions containing PNRs. These nanoribbons exhibit characteristic widths ranging from 4 to 50 nm, primarily consisting of a single layer in thickness, Figure 20 (a). Their measured lengths can extend up to 75 μm, while their aspect ratios reach impressive values of up to 1,000. It is noteworthy that these nanoribbons possess atomically flat surfaces, akin to single crystals, and their alignment is exclusively oriented in the zigzag crystallographic direction. This one exhibits high flexibility and widths and lengths uniformity. The exceptional uniformity in width along the entire length of the ribbons, combined with their remarkable flexibility, makes them highly suitable for downstream manipulation using liquid-phase methods. This ease of manipulation opens up avenues for exploring predicted exotic states and a diverse range of applications where PNRs are anticipated to deliver transformative benefits. These applications span various fields, including thermoelectric devices, high-capacity fast-charging batteries, and integrated high-speed electronic circuits. The unique properties of PNRs make them a promising candidate for advancing these technologies. In Figure 20 (b), we can observe the photoluminescence spectrum of grouped PNRs that have been placed on a graphite substrate.

The peaks with higher energy levels that we see in the spectrum can be attributed to specific characteristics of the Raman effect, which could originate from either the PNRs themselves or the graphite substrate. From a theoretical standpoint, the band structure of phosphorene nanoribbons

Figure 20 – (a) PNRs exhibit characteristic widths ranging from 4 to 50 nm, primarily consisting of a single layer in thickness. (b) PL spectrum of aggregated PNRs deposited on a graphite substrate. The high-energy peaks observed can be attributed to Raman features originating from either the PNRs or the graphite substrate. (c) DOS and conductance of defective PNRs with random vacancies for different vacancy concentrations P.

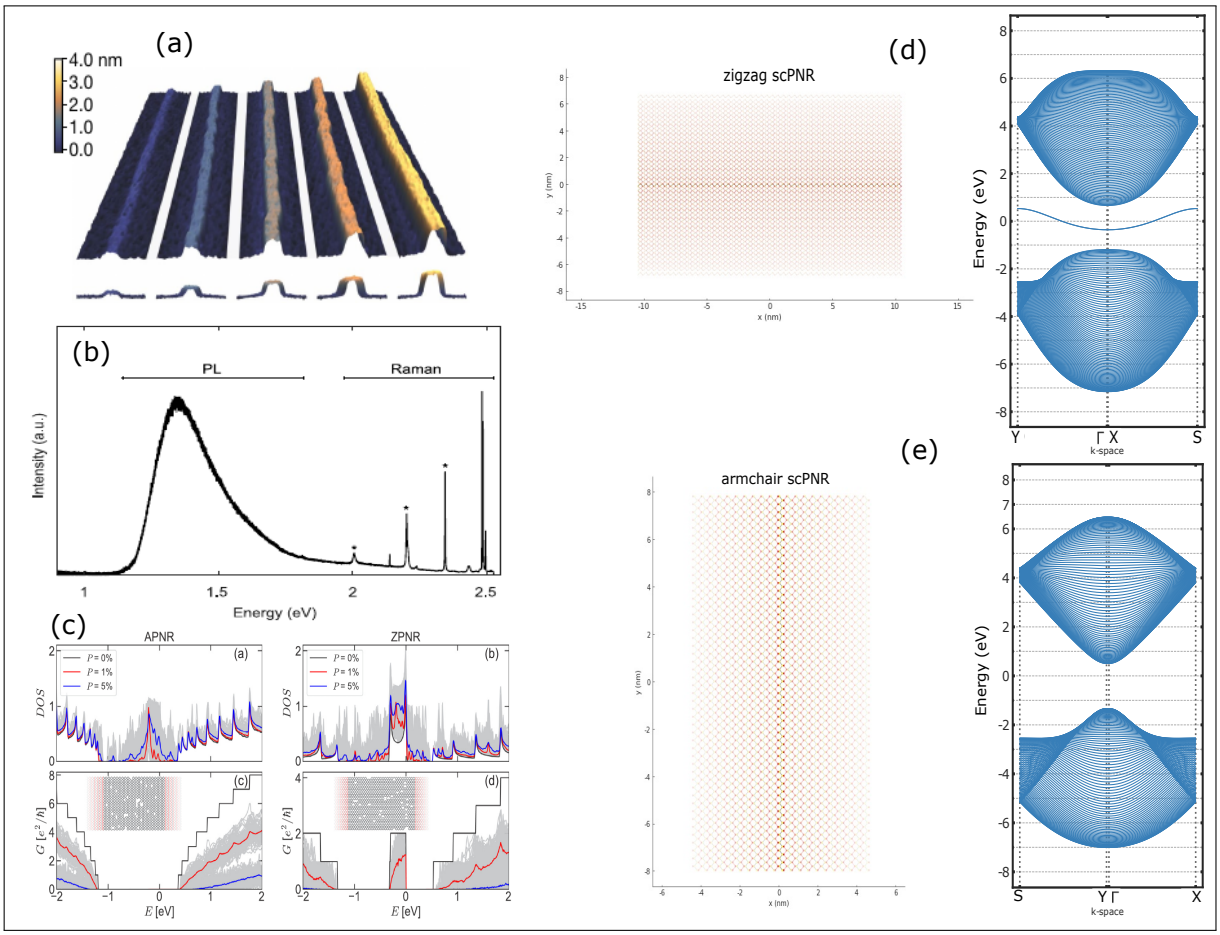

Source: Figure adapted from (Watts *et al.*, 2019; Li; Peeters, 2018).

can be calculated using numerical packages such as the Pybinding Python package. Figure 20 (d) and (e) displays the structure in the real space and band structure of zigzag (40×1) and armchair (1×40) of scPNRs, respectively. Other studies on vacancy defects have also been conducted using this package. Figure 20(c) presents the results of nanoribbons with random defects and the effects of these defects on the electronic structure of the material. Furthermore, other results have indicated a strong structural dependence on the vacancy position concerning its proximity to the nanoribbon edges (Smotlacha; Pincak, 2018; Sun *et al.*, 2018) and the vacancy type (Li;

Peeters, 2018; Amini *et al.*, 2019b).

In this section, we will present the results of the electronic structure analysis of PNRs using the band unfolding technique. The discussions on the influence of confinement on energy states are highlighted by the discretization of energy levels in the primitive cell, and the effects of vacancy defects confirm previous studies on the impact of defects on the electronic structure of PNRs.

7.2 Results and discussions

7.2.1 Pristine phosphorene nanoribbons

We can consider a PNR as a type of supercell (scPNR), where we do not take into account the periodic boundary conditions in one of the $x-$ and y-directions. By relinquishing the periodic boundary conditions in the x-direction, we form an scPNR with zigzag edges in the y-direction. Conversely, if we do not consider the periodic boundary conditions in the y-direction, we form scPNR with armchair edges in the x-direction. The electronic properties of these structures are well-known and extensively studied from a theoretical perspective (Lee *et al.*, 2015b; Sorkin *et al.*, 2017; Guo *et al.*, 2014; Carvalho *et al.*, 2014; Hu *et al.*, 2017; Nourbakhsh; Asgari, 2016; Das *et al.*, 2016; Yang *et al.*, 2016; Sisakht *et al.*, 2016; Wu *et al.*, 2016; Poljak; Suligoj, 2016; Yang *et al.*, 2016; Wu *et al.*, 2015; Zhang *et al.*, 2014; Yao *et al.*, 2015). However, there is a lack of literature that approaches these structures from the standpoint of band unfolding formalism. In this study, we will investigate scPNRs using the band unfolding theory.

The supercell parameters considered in Section 3.1 are valid for our nanoribbon construction. The combination of primitive unit cells gives rise to supercells. The lattice parameters of a supercell are $L_x = Ma_x$ and $L_y = Na_y$ along the $x-$ and y-directions, respectively, such that a $M\times N$ supercell is formed by assembling M (N) replicas of the primitive cell in the $y-$ (x)-direction, forming what we now refer to as scPNRs. Figure 21 (a)-(d) illustrates the variations of these structures in the inner panels. We analyzed the system as a hypothesis of variable interference, where the four variables are armchair nanoribbon, zigzag nanoribbon, and their variations in the $x-$ and y-directions, by increasing the size of the supercell. Figures 21 (a) and (b) display the projected energies along with their corresponding spectral weights for armchair scPNR configurations of dimensions 1×10 and 5×15, respectively. The discretization of energy levels in the confinement direction (y-direction) is evident, allowing for accurate estimation of

Figure 21 – Projected energy of scPNRs armchair (a)-(b) and zigzag (c)-(d). By increasing the size of the 1×10 (10×1) to 5×15(15×5) for armchair (zigzag) scPNR, we observe in the Γ-Y (Γ-X) direction (confinement direction) an increase in the number of discrete energy levels and a reduction in their width. For both cases, the estimation of low-energy levels with excellent precision, typically ranging from 0.1 to 0.5 eV. For zigzag scPNR case, the transition energies between the lower levels range from approximately 2-2.5 eV, with specific transitions occurring at 2.15 eV, 2.25 eV, and 2.45 eV. These levels are consistent with a possible electronic resonant Raman effect in Figure 20 (b) (Watts *et al.*, 2019).

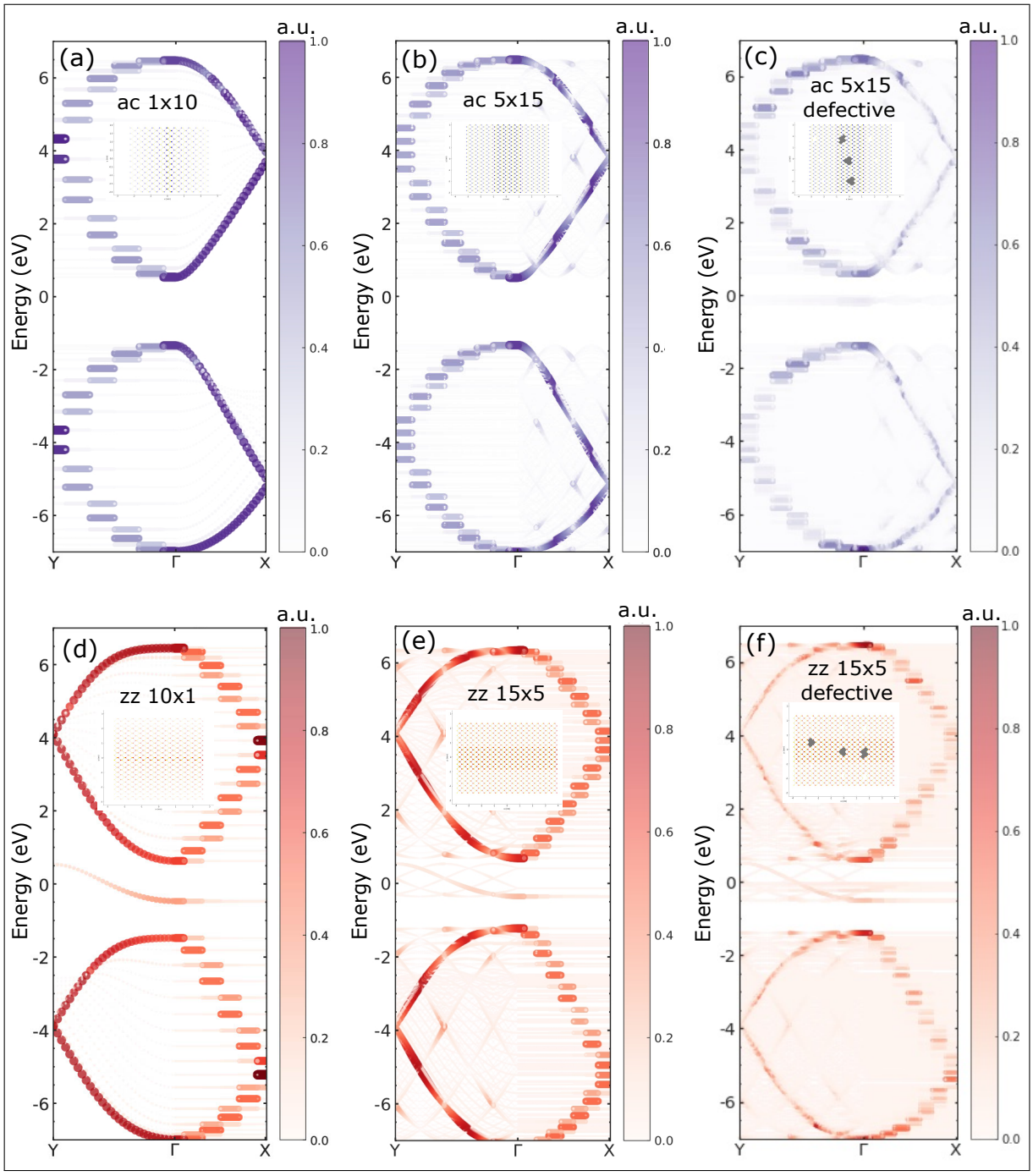

Source: Figure elaborated by the author (2023).

low-energy levels with excellent precision, typically ranging from 0.1 to 0.5 eV. Furthermore, we can observe the presence of energy levels with higher spectral weights, indicating a higher probability of occupation. By increasing the size of the 1×10 armchair scPNR to 5×15, we observe in the Γ-Y direction (confinement direction) an increase in the number of discrete energy levels and a reduction in their width. This confirms our notion that a nanoribbon behaves as a supercell, given that there is an integer number of primitive cells within the supercell. As the supercell approaches infinity, the system tends towards a bulk-like behavior. In the Γ-X direction, which encompasses periodic boundary conditions in real space, we also observe an enlargement of the scPNR. However, since there are no modifications to the crystal structure in this direction, the energy projection tends towards the band structure of the primitive cell, as if the crystal were kept pristine. This behavior is evident in Figure 21 (b).

For a zigzag scPNR, as shown in Figure 21 (c) and (d), the opposite edges consist of non-equivalent sublattice atoms, breaking the sublattice symmetry of the crystal and giving rise to a quasi-flat state in the middle of the energy gap. By unfolding the energy bands of the zigzag scPNR, we also observe the state in the middle of the energy gap, which is characterized by a lower spectral weight compared to the conduction and valence bands. This indicates that the transition can occur directly between these bands. In the zigzag scPNR, the confinement occurs in the *x*-direction in real space, and we observe discrete energy levels in the Γ-X direction in phase space. Similar to the armchair scPNR, when we increase the size of the zigzag scPNR from 10×1 to 15×5, we identify an increase in the number of discrete energy levels and a reduction in their width in the Γ-X direction (confinement direction). The transition energies between the lower levels range from approximately 2-2.5 eV, with specific transitions occurring at 2.15 eV, 2.25 eV, and 2.45 eV. These levels are consistent with a possible electronic resonant Raman effect in Figure 20 (b) (Watts *et al.*, 2019). In the Γ-Y direction, where no modifications are made to the crystal, the energy projection tends to align with the band structure of the primitive cell, as if the crystal were left untouched, as well as to armchair scPNR, just like in the armchair scPNR case, as we can compare in 21 (b).

7.2.2 Vacancy defect in phosphorene nanoribbons

As we observed in the previous chapter (Chapter 6), it is evident that vacancy defects modify the electronic properties of few-layer phosphorene sheets. Based on our analysis, we have found that the unfolding formalism effectively demonstrates the flawed band structure of

multilayer phosphorene. We have also discovered that defects can be leveraged to manipulate the electronic and optoelectronic characteristics of a small number of phosphorene layers. This manipulation involves altering the type, concentration, and distribution of vacancies within the layers. Additionally, our findings indicate that a supercell with dimensions of 6×6 can accurately restore the anticipated and desired band structure of BP under conditions where vacancy densities on the BP lattice are low. We would not expect significantly different results, primarily due to the fact that we are now considering supercells without periodic boundary conditions in one of their two-dimensional directions, forming what we refer to as scPNRs (supercell phosphorene nanoribbons). In the investigation of vacancy defects in scPNRs, we analyzed defects that break the sublattice symmetry (D_{2h}) of the phosphorene crystal. These defects include the absence of a single atom from sublattice A/B (C/D) and the absence of two atoms from the same sublattice A/B (C/D). These defects were randomly distributed in a 5×15 armchair scPNR and a 15×5 zigzag scPNR. Figure 21 (c) and (f) illustrate the band unfolding results for these supercells. It can be observed that the effects of defects on the electronic structure were more pronounced in the energy gap region and in directions where there is no confinement. In the case of zigzag scPNRs [Figure 21 (f)], the defect bands disperse within the gap region around the Γ point, exhibiting a discrete appearance between 0 eV and -0.5 eV. On the other hand, for armchair scPNRs [Figure 21 (c)], the defect band energies range between 0 eV and -0.25 eV, showing a continuous appearance. In the zigzag scPNR, the confinement direction is the *x*-direction, and no significant change in the energy levels is observed when compared to the defect-free scPNR [Figure 21 (e)], except for a slight decrease in the energy levels. This outcome was expected, as the defect bands disperse within the gap region, leading to an energy rearrangement among the levels. The same phenomenon occurs in the armchair scPNR, but in the Γ-Y direction in the momentum space. A more pronounced effect is observed in both cases at lower energy levels in the conduction bands, specifically in directions where there is no confinement. A distortion of the bands near the Γ point is observed, indicating a low probability of charge carriers occupying that region.

7.3 Conclusions

We have been investigating PNRs using the band unfolding formalism. Treating PNRs as a type of supercell (scPNR), we first analyzed the behavior of the unfolded band structure of perfect crystal nanoribbons with armchair (zigzag) edges of sizes 1×10 (10×1) and

5×15 (15×5). The discretization of energy levels in the confinement direction (x-direction for zigzag and y-direction for armchair) is evident, allowing for accurate estimation of low-energy levels with excellent precision, typically ranging from 0.1 to 0.5 eV, for armchair scPNR case. The transition energies between the lower levels range from approximately 2-2.5 eV, with specific transitions occurring at 2.15 eV, 2.25 eV, and 2.45 eV, for zigzag scPNR case. In addition, by increasing the size of the 1×10 (10×1) to 5×15(15×5) for armchair (zigzag) scPNR, we observe in the Γ-Y (Γ-X) direction (confinement direction) an increase in the number of discrete energy levels and a reduction in their width. As the supercell approaches infinity, the system tends towards a bulk-like behavior.

For the analysis of defective scPNRs, we investigated defects that break the sublattice symmetry (D_{2h}) of the phosphorene crystal. These defects include the absence of a single atom from sublattice A/B (C/D) and the absence of two atoms from the same sublattice A/B (C/D), which were randomly distributed in a 5x15 armchair scPNR and a 15x5 zigzag scPNR. In the case of the zigzag scPNR, the defect bands disperse within the gap region around the Γ point, exhibiting a discrete appearance between 0.1 eV and -0.5 eV. On the other hand, for the armchair scPNR, the defect band energies range between 0 eV and -0.25 eV, showing a continuous appearance. A distortion of the bands near the Γ point is observed, indicating a low probability of charge carriers occupying that region.

In conclusion, our results provide a new perspective for a more accurate analysis of phosphorene nanoribbon structures, which can be highly valuable for controlling electronic and optical properties in the development of novel optoelectronic devices.

8 ANISOTROPIC ELECTRONIC TRANSPORT IN MONOLAYER AND BILAYER PHOSPHORENE

8.1 Introduction

Studies on the electronic transport of two-dimensional (2D) materials have triggered several proposals for controlling the electron propagation in these systems, such as lenses (Lee *et al.*, 2015a; Chen *et al.*, 2016; Milovanović *et al.*, 2015; Libisch *et al.*, 2017), beam splitters (Papasimakis *et al.*, 2013; Ryzhii; Ryzhii, 2007; Degl'Innocenti *et al.*, 2014; Vasić *et al.*, 2013), and modulators (Habib; Lake, 2012; Nakaharai *et al.*, 2013; Araújo *et al.*, 2020; Araújo *et al.*, 2021; Araújo *et al.*, 2022). Within this context, a growing literature has sought quantum analogous' optical devices in nanostructured 2D-based materials to manipulate the electronic propagation, as for instance in monolayer (Wang *et al.*, 2019; Araújo *et al.*, 2020; Araújo *et al.*, 2021) and bilayer graphene(Huang *et al.*, 2019; Abdullah *et al.*, 2019). In addition, optic-like phenomena in other structures, such as phosphorene p-n junctions, suggest that it could become an ideal platform for studying collimation, direction switching, and electron flow filtering in optical-electronic devices.(Dana *et al.*, 2020; Betancur-Ocampo *et al.*, 2019; Sarkar *et al.*, 2017; Li *et al.*, 2017; Li *et al.*, 2019)

Samples of few-layer 2D materials extracted from their bulk versions often contain patches of different numbers of layers in the same region of the sample. The possibility of finding new physical properties in such regions has led in the last two decades to several studies on electronic (Wang *et al.*, 2016; Lane *et al.*, 2018; Jaskólski *et al.*, 2018; Hu; Ding, 2012) and transport (Ju *et al.*, 2015; Abdullah *et al.*, 2017; Jamaati; Namiranian, 2017; Abdullah *et al.*, 2018; Yin *et al.*, 2016; Abdullah *et al.*, 2019) properties. In most cases, as occurs in monolayer-bilayer graphene junctions, the two individual portions have qualitatively different band structures so that new effects, not observed in each portion separately, can arise. Recent works addressing monolayer-bilayer graphene junctions (Jamaati; Namiranian, 2017; Chico *et al.*, 2012; Nakanishi *et al.*, 2010; Mirzakhani *et al.*, 2017; Mirzakhani *et al.*, 2018; Mirzakhani *et al.*, 2017; Rusekas *et al.*, 2012; Nakanishi *et al.*, 2011; Koshino *et al.*, 2010; Mirzakhani *et al.*, 2023) showed that the transport properties are strongly affected by the geometry of the interfaces, exhibiting a pronounced incident angle dependent transmission and a different dependence for electron beams incident from K and K$'$ Dirac points, leading to possible efficient valley polarization of the transmitted wave for certain graphene junction configurations.

Phosphorene, a single-layer or few-layers of Black Phosphorus (BP), has received significant attention in recent years (Xia *et al.*, 2019) after results showed its high electronic mobility (Xia *et al.*, 2014), widely tunable band gap (Das *et al.*, 2014), and strong in-plane anisotropy (Carvalho *et al.*, 2016b). Due to its crystallographic structure composed of P atoms with sp^3 hybridization, phosphorene displays a puckered structure, which in turn makes to emerge a significant difference in their electronic and transport properties along the armchair and zigzag directions (Xia *et al.*, 2014). This is a direct consequence of the anisotropic aspect of phosphorene band structure that manifests itself in direction-dependent effective masses and group velocities, with higher electron/hole effective mass (Liu *et al.*, 2014) and lower phonon group velocity (Jain; McGaughey, 2015) along the zigzag direction when compared to the armchair direction. Another important aspect of BP is the dependence of the band gap on the number of layers (Sousa *et al.*, 2017a). Experiments have shown that for monolayer BP the gap value is ≈ 1.8 eV, being reduced to ≈ 0.4 eV in bulk samples (Liu *et al.*, 2014; Tran *et al.*, 2014; Castellanos-Gomez, 2015; Dolui; Quek, 2015a; Das *et al.*, 2014; Zhang *et al.*, 2017). In contrast to bilayer graphene, which shows an increase in the band gap with the application of an external electric field (Zhang *et al.*, 2009; Ohta *et al.*, 2006; Castro *et al.*, 2010), the band gap in bilayer phosphorene is reduced by an electric field, which can lead to a transition from semiconductor to semimetal with the appearance of two Dirac cones around the Γ-point. This counter-intuitive fact was theoretically (Dolui; Quek, 2015a; Baik *et al.*, 2015b) predicted in 2015 and experimentally (Ehlen *et al.*, 2018; Kim *et al.*, 2017a; Kim *et al.*, 2015) verified in 2017.

Recently, the anisotropic electronic transport (Sarkar *et al.*, 2017; Li *et al.*, 2017; Betancur-Ocampo *et al.*, 2019) and optical (Li *et al.*, 2019) behaviors of monolayer phosphorene modulated by periodic potential superlattices have been reported. De Sarkar *et al.* (2017) demonstrated that the transport properties through multiple potential barriers in monolayer phosphorene along the armchair direction are distinct from their counterparts in both conventional 2D electron gas with Schrödinger-like quasiparticles and graphene or surfaces of topological insulators hosting massless Dirac quasiparticles. This particularity is a consequence of the highly anisotropic phosphorene band structure that exhibits for small momentum values an approximately parabolic dispersion relation along the $\Gamma - X$ (armchair) direction and approximately linear dispersion relation along the $\Gamma - Y$ (zigzag) direction and therefore charge carriers behave similarly as Schrödinger and gapped Dirac-like particles, respectively. Moreover, Li *et al.* (2017) reported asymmetric Klein tunneling behavior for massless Dirac fermions with a chiral character gener-

ated from anisotropic 2D electron gas systems, viewed as patterned few-layer BP superlattices, in which such chiral states exhibit a tunable transmission probability of the wave packets with a normal incidence that is no longer unity. Additionally, Betancur-Ocampo *et al.* (2019) found negative and anomalous reflection for tilted junctions and also observed anti-super-Klein tunneling in phosphorene p-n junctions in the case in which the junction is parallel to the armchair edge. These unconventional electronic transport features make phosphorene-based physical systems promising candidates for nanoelectronic applications.

Following the example of few-layer graphene-based planar junctions (Chu *et al.*, 2017; Rusekas *et al.*, 2012; Nakanishi *et al.*, 2011; Koshino *et al.*, 2010; Mirzakhani *et al.*, 2023; Hu; Ding, 2012; Abdullah *et al.*, 2019; Mirzakhani *et al.*, 2017; Mirzakhani *et al.*, 2018; Nakanishi *et al.*, 2010; Chico *et al.*, 2012; Abdullah *et al.*, 2017; Jamaati; Namiranian, 2017; Abdullah *et al.*, 2018), i.e. 2D lateral junctions formed by portions with a different number of layers, a natural research direction is to investigate similar physical systems composed of other 2D materials, in particular, anisotropic semiconductors, since such materials are expected to exhibit physical properties significantly different from those found in typical semiconductors as well as in graphene due to their highly anisotropic band structures. In this sense, the existence of both monolayer and bilayer portions in the same exfoliated phosphorene samples (Brent *et al.*, 2014c; kou *et al.*, 2015) motivated us to systematically study the transport properties of hybrid phosphorene junctions, which consist of monolayer phosphorene portions laterally coupled to bilayer phosphorene portions, formed by one or two interfaces, such as: monolayer-bilayer (MB), monolayer-bilayer-monolayer (MBM), and bilayer-monolayer-bilayer (BMB) junctions (see Figure 22). With this goal, in this paper, we study how the conductances and trajectories of incident electron beams are affected by the different phosphorene junction configurations with the two most commonly considered interfaces/edges (armchair and zigzag) and how to manipulate their electron transport properties when the system is subjected to an out-of-plane electric field, perpendicular to the electron propagation direction. To our knowledge, no similar systematic work has been reported in the literature considering the different types of edge alignments and different numbers of interfaces in few-layer phosphorene lateral junctions. In this direction, Lin *et al.* (2017) investigated, by first-principles calculations, the structural and electronic properties of the lateral heterostructures of MB phosphorene junctions; Shukla *et al.* (2021) explored, using the first-principles formalism, the interlayer properties of a vertically stacked bilayer BP structure with paired substitutional doping and studied the role played by dopants in the quantum transport

properties of MBM BP nanojunctions; and Gong *et al.* (2019) considered just zigzag-edge MB phosphorene nanoribbon junctions.

This section is organized as follows. In Sec. 8.1.1, the system setup assumed in our numerical calculations and the theoretical framework, based on the tight-binding model, used to describe the transport properties of the investigated few-layer phosphorene junctions are present. Section 8.2 is dedicated to the discussions of the main results for the conductances and probability current densities for the different phosphorene junctions, with zigzag and armchair interfaces formed by one or two interfaces in the presence or not of a perpendicular electric field. Such results will be explained in the context of the band structure alignment associated with the phosphorene dispersion relations for each portion of the BP junctions, being their physical features also reviewed in Sec. 8.2.

8.1.1 Model

BP is a layered material where each individual atomic layer has phosphorus atoms connected to three nearest neighbors by covalent chemical bonds, being two in-plane and one out-of-plane (Jr; Katsnelson, 2015). Because of the different bond angles owing to the non-planar structure of phosphorene, each phosphorus atom has two neighbors at a distance of 2.224 Å in the same sublayer and a third one at 2.244 Å in the adjacent sublayer [see Fig. 22(a)] (Carvalho *et al.*, 2016b; Sousa *et al.*, 2017a), so that the lattice parameters are 4.374 Å and 3.313 Å along the zigzag and armchair directions, respectively (Cartz *et al.*, 1979b). The resulting top-view crystal structure resembles the graphene honeycomb lattice. However, the sp^3 hybridization between $3s$ and $3p$ BP atomic orbitals creates ridges that result in a puckered surface (Jr; Katsnelson, 2015; Sousa *et al.*, 2017a). Similarly to multilayer graphene that can be isolated by peeling procedures, two BP monolayers are coupled via van der Waals interactions giving rise to a bilayer phosphorene. Their separation distance is of 3.214 Å. In this paper, we consider AB- (Bernal) stacked bilayer BP, as shown in Fig. 22(b).

This is energetically the most stable stacking configuration for multilayer BP according to first-principle calculations(Çakır *et al.*, 2015) and can be obtained by shifting the upper and lower phosphorene layers by a distance of half of the unit cell along the armchair or zigzag directions (or similarly, by a $\pi/3$ rotation) (Li *et al.*, 2017b).

We theoretically investigate MB, MBM, and BMB phosphorene junctions, such as schematically illustrated in Figure 22(d), 22(e), and 22(f), respectively. These are the junctions

made of the same two-dimensional material from portions with different numbers of layers commonly found. We consider two types of edges: armchair and zigzag. Thus, for phosphorene junctions with armchair (zigzag) edges, the interface will be along the zigzag (armchair) direction.

Charge carriers in multilayer phosphorene (Rudenko *et al.*, 2015; Sousa *et al.*, 2017a) can be described by the following tight-binding Hamiltonian (Sousa *et al.*, 2017a)

Figure 22 – (a) Side and (b) top views of the AB-stacked bilayer phosphorene crystal structure, emphasizing the orientation of the system [armchair (zigzag) direction along the $x(y)$-axis], the two distinct intralayer distances given by 2.22 Å between sites at a same sublayer and by 2.24 Å between sites at different sublayers, the intralayer (t_1 and t_2) and interlayer (t_3) hoppings, and the primitive vectors $\mathbf{a}_1$ and $\mathbf{a}_2$. P atoms at the upper and lower layers are represented by red and blue symbols, respectively. Three phosphorene junctions are studied, namely: (d) monolayer-bilayer (MB), (e) monolayer-bilayer-monolayer (MBM), and (f) bilayer-monolayer-bilayer (BMB). The interfaces that separate the monolayer and bilayer portions are assumed here to exhibit armchair or zigzag terminations, as well as to be aligned or anti-aligned with respect to the atomic bonds at both boundary sides of the domain wall in the junctions, as shown in the panel (c). For all three BP junctions, it was taken finite-size phosphorene nanostructures with nanoribbons width of W and a non-zero perpendicularly applied electric field (i.e., along the z-direction) only in the bilayer BP regions. The domain wall length is defined as L in the MBM and BMB junctions.

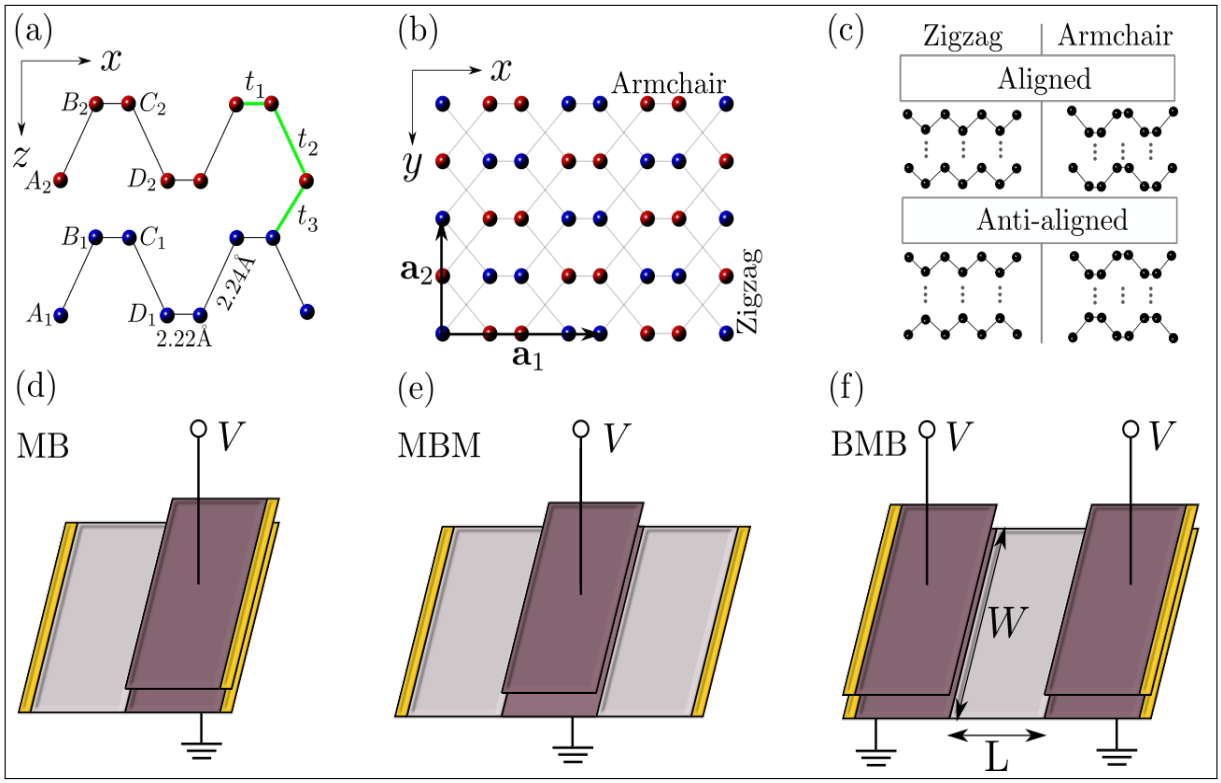

Source: Figure elaborated by the author (2023).

$$H = \sum_i (\varepsilon_i + V_i) c_i^\dagger c_i + \sum_{i \neq j} \tau_{ij}^{\parallel} c_i^\dagger c_j + \sum_{i \neq j} \tau_{ij}^{\perp} c_i^\dagger c_j, \tag{8.1}$$

where the sum runs over all sites of the crystal lattice, c_i ($c_i^\dagger$) is an operator that annihilates (creates) an electron at site i with on-site energy ε_i, and $\tau_{ij}^{||}$ ($\tau_{ij}^{\perp}$) is the intralayer (interlayer) hopping parameter between sites i and j. Rudenko & Katsnelson (2014b) provided in 2014 the tight-binding parameters within the context of the five-intralayer hopping model, and one year later, they obtained (Rudenko *et al.*, 2015) from DFT-GW calculations over a wide energy range a more accurate description but now with ten-intralayer hoppings. A minimal tight-binding model, that captures the main features of the monolayer and bilayer BP band structures, for instance, the anisotropy of the bands and lowest band curvatures, takes into account the two largest intralayer hopping parameters [see t_1 and t_2 in Fig. 22(a)]. Such a minimal tight-binding model has been successfully used in some previous works (Li *et al.*, 2017b; Sisakht *et al.*, 2015) in the literature to describe the electronic and transport properties of monolayer and bilayer phosphorene quantum dots and phosphorene nanoribbons and it is the one adopted here. Therefore, the second summation in the right-hand side of Eq. 8.1 runs over 2 intralayer hoppings. The third summation related to the interlayer coupling effect is assumed here

Within a minimal tight-binding model for multilayer systems, at least one interlayer coupling should be considered, in view that the coupling of BP multilayers can be approximately a quasi-1D tight-binding model along z-direction, where each phosphorene layer is associated with an atomic site and consequently the interlayer coupling energy is linked to the hopping parameter of the 1D z-chain. V_i, in turn, is the on-site potential used to introduce the effect of the external electric field. This field is applied along the z-direction, i.e., $\mathbf{F} = (0,0,F_z)$, and is perpendicular to the propagation direction between the input and output leads. The intralayer hopping parameters are $t_1 = -1.21$ eV and $t_2 = 3.18$ eV and the interlayer hopping parameter $t_3 = 0.22$ eV, as defined in Fig. 22(a). We use phosphorene nanoribbons with width $W \approx 18.2$ nm, domain walls [in Figure 22(e) and 22(f)] with length $L \approx 41.9$ nm, subject to a perpendicular electric field only in the bilayer regions. The phosphorene junctions MBM and BMB can have domain walls with aligned or anti-aligned interfaces, as shown in Fig. 22(c), so this alignment (anti-alignment) can influence the transport properties. One can associate four sub-layers with a phosphorene bilayer, so the effect of applying a perpendicular electric field is to provide each sub-layer with an on-site potential, namely, $(1/2+\varepsilon)V$, $(1/2-\varepsilon)V$, $(-1/2+\varepsilon)V$, and $(-1/2-\varepsilon)V$, where V is the potential difference between the top and bottom phosphorene monolayers that form the phosphorene bilayer and $\varepsilon = 0.202$ is a linear scaling factor (Li *et al.*, 2017b). The perpendicular electric field strength F_z is related to V by $V = eF_z d$, where e is the elementary

Figure 23 – (Color online) Band structures and conductances for monolayer and bilayer phosphorene nanoribbons with (a - h) armchair and (i - p) zigzag edges. Three different bias potentials are taken: (c, d, k, l) $V = 0$, (e, f, m, n) $V = V_c$, and (g, h, o, p) $V = 2V_c$, with $V_c = 1.5$ eV. For the monolayer BP case (a, b, i, j), one shows only results in the absence of a perpendicular electric field, since a non-zero V solely shifts the energy spectrum, changing thus its Fermi level.

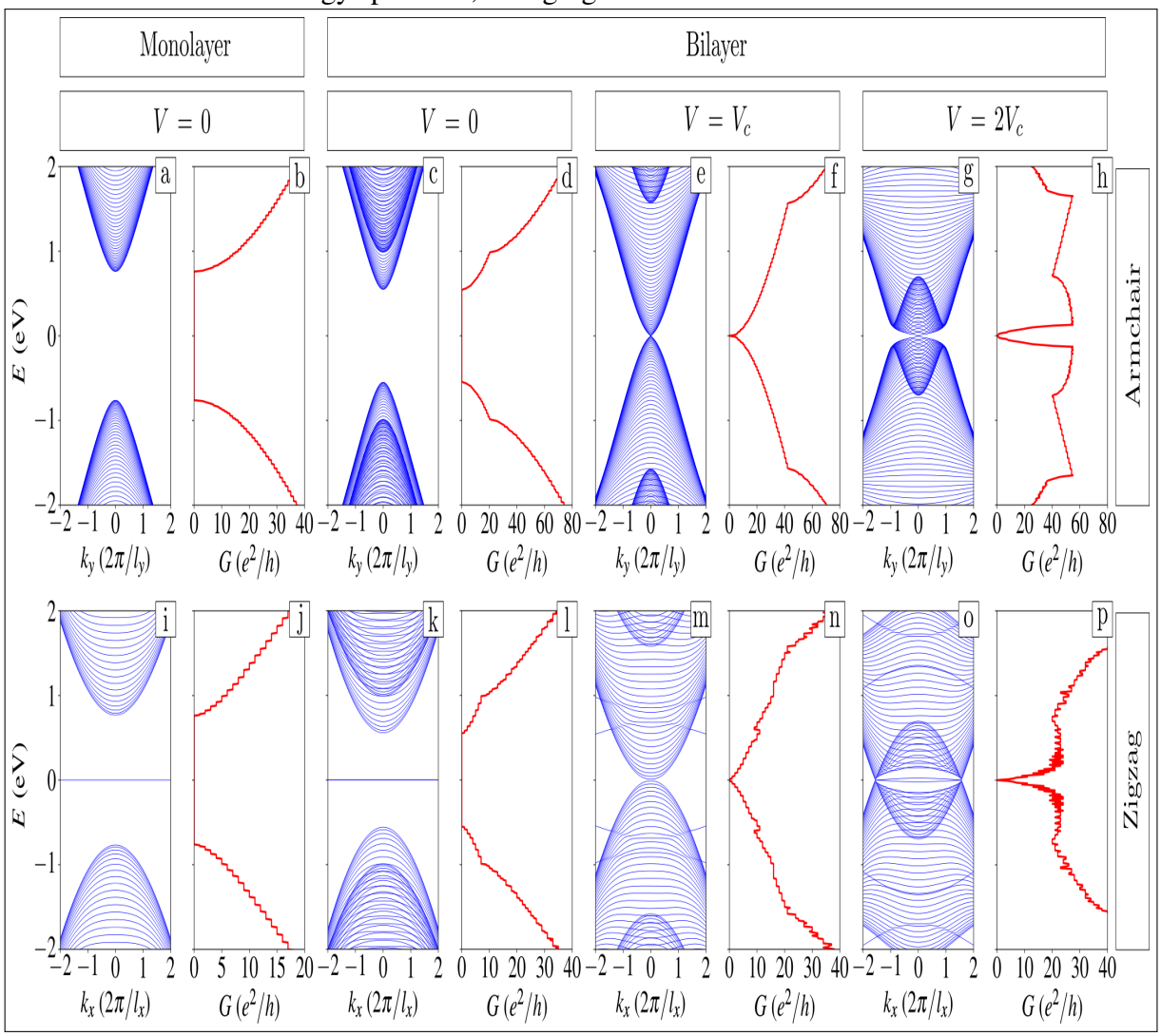

Source: Figure elaborated by the author (2023).

electric charge and $d = 3.214$ Å} is the inter-layer separation. The theoretical framework used here is based on the Landauer-Büttiker formalism, where the transport properties are computed within the wave function approach (Groth *et al.*, 2014) and by using the tight-binding model (Sousa *et al.*, 2017a; Rudenko *et al.*, 2015). In this sense, two leads are connected to each phosphorene junction so that we are going to study the transport of charge carriers from the left lead to the right lead in the scattering region. Within the Landauer-Büttiker formalism, these leads act as wave guides leading plane waves into and out of the scattering region (Groth *et al.*, 2014).

In the next section, we calculate the conductance as a function of the Fermi energy for the phosphorene junctions (d) MB, (e) MBM, and (f) BMB of Fig. 22. Then, we investigate the effect of potential modulation, edge type (armchair or zigzag), alignment/anti-alignment of the interfaces, variation of the domain wall length, and input lead width reduction. Finally, we address the collimation of charge carriers at the interfaces for the three proposed phosphorene junctions by calculating the probability of current density. All the electronic transport calculations were performed using the Kwant code, a free (open source) Python package for numerical calculations on tight-binding models (Groth *et al.*, 2014).

8.2 Results

Monolayer and bilayer BP band structures are highly anisotropic, exhibiting a direct band gap. Within the ten (five) intralayer (interlayer) hopping parameters tight-binding model (Fu; Cheng, 2019), the band gap in the absence of external fields is ≈ 1.838 eV for monolayer BP and ≈ 1.126 eV for bilayer BP. Under the effect of a perpendicular electric field (i.e., the bias gate (Dolui; Quek, 2015a; Baik *et al.*, 2015b; Ehlen *et al.*, 2018; Kim *et al.*, 2017a)) or doping (Shukla *et al.*, 2021), bilayer BP energy spectrum shows interesting topological features driven by a gap closing due to the breaking of inversion symmetry, such as a gapless linear band structure in the semimetal phase around the $\Gamma - Y$ direction, but exhibits a quadratic dispersion with band-inversion along the $\Gamma - X$ direction (Li *et al.*, 2017b). For monolayer BP, the application of a perpendicular electric field F_z only shifts the energy spectrum, changing thus the Fermi level of the system. In contrast, for biased bilayer BP, the valence and conduction bands are shifted in different directions close to the band gap center. This causes a decrease of the band gap with increasing the electric field magnitude and drives a semiconductor-to-semimetal transition when $F_z = F_c$, where F_c is the critical perpendicular electric field of ≈ 3.41 V/nm. (Rudenko *et al.*, 2015; Fu; Cheng, 2019; Li *et al.*, 2017b).

The phosphorene junctions investigated in this work are composed, as seen, of portions of monolayers and bilayers. In this sense, previously analyzing the band structure and conductance of each portion separately is essential for understanding and discussing the transport properties in such junctions. Figures 23(a) and 23(b) [Figure. 23(i) and 23(j)] show the band structure and conductance, respectively, of a monolayer with armchair [zigzag] edges in the absence of a perpendicular electric field. Likewise, in Figure 23(c) and 23(d) are shown the band structure and conductance, respectively, of a bilayer with armchair edges in the absence of a

perpendicular electric field. The effect of a perpendicular electric field is displayed in Figure 23(e) and 23(f) for $V = V_c$, and in Figure 23(g) and 23(h) for $V = 2V_c$, where $V_c = 1.5$ eV is the potential corresponding to the critical perpendicular electric field F_c. The bilayers with zigzag edges are shown following the same sequence as above in Figure 23(k)-(p).

Taking t_1=-1.21 eV, t_2=3.18 eV, and t_3=0.22 eV, one obtains for the direct band gap in monolayers E_{bg}^{M}=$2t_2 + 4t_1$=1.51 eV and in bilayers E_{bg}^{B}=$2t_2\sqrt{1+(t_3/t_1)^2} + 4t_1 - 2t_3$=1.09 eV (Li *et al.*, 2017b), in agreement with the values obtained by the tight-binding model with fifteen hopping parameters proposed in reference (Rudenko *et al.*, 2015). The band gap is inherently due to the puckered crystal structure of phosphorene. The effect of a perpendicular electric field on the energy spectrum of monolayers is only to increase the band gap, having little effect on the main characteristics of the energy bands. On the other hand, in bilayers, the effect of applying a perpendicular electric field is the displacement in different directions of the valence band and the conduction band close to the band gap center. This causes a decrease in the band gap as the external field increases and leads to a semiconductor-semimetal transition when the potential assumes the value $V_c \approx 1.5$ eV [Figure 23(e) and 23(m)]. The difference between the band gap behavior under the application of an external field in monolayers and bilayers is due to the interlayer coupling, which is also responsible for the decrease of the band gap. As shown below, the electrically tunable band structure of bilayer BP has important consequences for the transport properties of phosphorene junctions of monolayers and bilayers. For perpendicular electric fields with strengths greater than F_c, the valence and conduction bands undergo a transition resulting in the formation of a Dirac-type energy spectrum. Such behavior can be seen in Figure 23(g) (armchair case) and 23(o) (zigzag case). For low energies in both cases, the energy spectrum resembles those of graphene nanoribbons, in which the presence of one (two) Dirac cone (cones) in the zigzag (armchair) case is observed.

Next, we investigate the conductance and probability current density of the phosphorene junctions displayed in Figure 22(d), 22(e), and 22(f). Figures 24(a)-(d) [24(e)-(h)] show the conductance G as function of Fermi energy E of monolayer and bilayer phosphorene junctions with zigzag [armchair] interfaces for various parameter settings. We consider three values for the applied potential in the bilayer regions, namely, $V = 0$ represented by the black curve, $V = V_c$ represented by the blue curve, and $V = 2V_c$ represented by the red curve. In Figure 24(a) and 24(e) [Figure 24(b) and 24(f)] we show the results for a perpendicular electric field pointing into [out] the page taking the same width for the lead and the scattering region. In Figure 24(c), 24(d),

24(g), and 24(h) we consider the influence of reducing the width of the input lead. Finally, in Figure 24(d) and 24(h), we verify the effect of inserting lateral leads that can collect scattered charge carriers at the interface as well as eliminate reflections at the edges. As seen in Fig. 24, in

Figure 24 – (Color online) Conductances, in units of e^2/h, as a function of Fermi energy, in units of eV, of monolayer and bilayer phosphorene junctions. Three values for the applied potential were taken, namely, $V = 0$ represented by the black curve, $V = V_c$ represented by the blue curve, and $V = 2V_c$ represented by the red curve. Panels from (a) to (d) [from (e) to (h)] refer to zigzag [armchair] interfaces. In panels (a) and (e) [(b) and (f)], we consider a perpendicular electric field pointing into [out] the page and the same width for the lead and the scattering region. In panels (c), (d), (g), and (h), we consider the input lead width to be smaller than the scattering region width. Finally, in panels (d) and (h), lateral leads were inserted in order to eliminate reflections at the edges and collect scattered charge carriers at the interface.

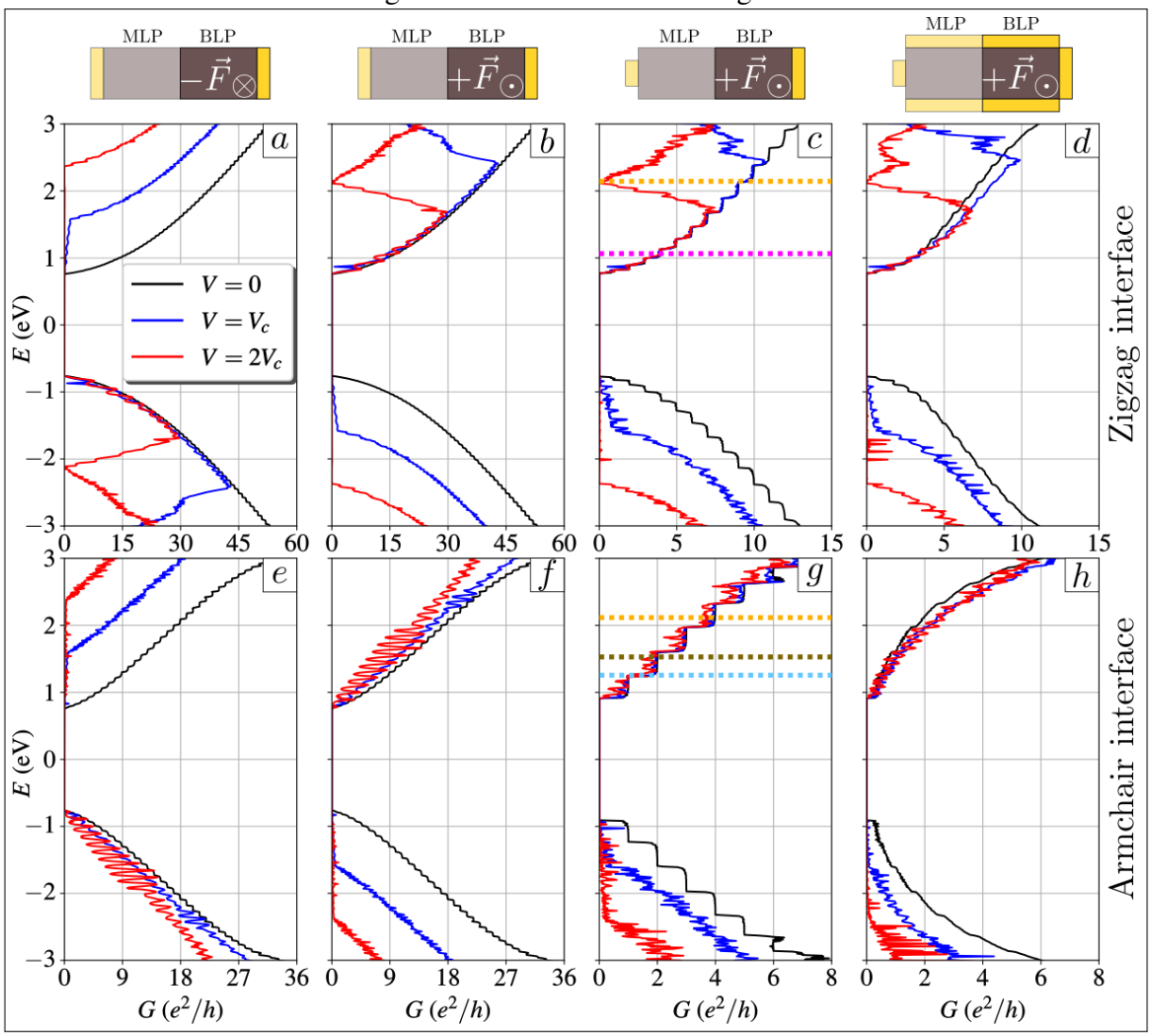

Source: Figure elaborated by the author (2023).

the absence of the external field the electron-hole symmetry is maintained and the conductance increases together with the Fermi energy. This is expected since the conductance is determined by

the number of occupied subbands which increases with increasing Fermi energy. In this situation, the band gap of the MB phosphorene junction is determined by the band gap of the monolayer region, as the separation between the lower subbands is greater than that of the bilayer region. The presence of an applied potential breaks the electron-hole symmetry, as can be seen in Fig. 24 for $V = V_c$ and $V = 2V_c$. This symmetry break can be explained by the fact that a charge carrier with $E > 0$ injected by the left lead will be transmitted through the interface passing from the monolayer region in the absence of external fields to the bilayer region composed of two coupled monolayers, the bottom one is subjected to a potential $\approx V/2$ and the top one is subjected to a potential $\approx -V/2$. On the other hand, by reversing the direction of the perpendicular electric field, the bottom monolayer will be subjected to a potential $\approx -V/2$ and the top monolayer will be subjected to a potential $\approx V/2$, so that when the direction of the perpendicular electric field is reversed, the conductance is reflected with respect to $E = 0$, as can be seen in Figure 24(a), 24(b), 24(e), and 24(f). The band gap in the monolayer region is larger than in the bilayer region. Thus, the interface separating the two portions of this phosphorene junction acts as a potential step for the charge carriers injected into the scattering region. Therefore, charge carriers coming from the left side with positive Fermi energies E_1, greater than the lowest subband V_1 of the bilayer region and smaller than the lowest subband V_2 of the monolayer region, will cross the interface delimited by $V_1 < E_1 < V_2$, which can be interpreted in terms of a potential well. On the other hand, for negative Fermi energies E_2, greater than the lowest subband of the monolayer region and smaller than the lowest subband of the bilayer region, the charge carriers coming from the left side will cross the interface delimited by $V_2 < E_2 < V_1$, which in turn can be interpreted in terms of a potential barrier.

The effect of reducing the width of the input lead is shown in Figure 24(c), 24(d), 24(g), and 24(h). Qualitatively, the behavior of the conductance in relation to the Fermi energy is preserved, however, a reduction in $G(E)$ is observed when compared to the case where the width of the input lead is equal to the width of the scattering region, since the conductance is determined by the number of occupied subbands which is proportional to the width of the input lead. The influence of inserting lateral leads in the scattering region is shown in Figure 24(d) and 24(h). In this configuration, charge carriers are emitted by the input lead and can be collected by the output lead as well as by the two inserted lateral leads, so that charge carriers that previously reflected at the edges or scattered at the interface are now collected by the lateral leads, reducing the number of charge carriers collected by the output lead individually, preserving

Figure 25 – (Color online) Probability current densities for the phosphorene junction considered in panel (c) of Fig. 24. We take two specific values for the Fermi energy, namely, $E = 1.07$ eV [panels (a) and (b)] and $E = 2.14$ eV [panels (c) and (d)]. Panels (a) and (c) illustrate the case where $V = 0$, and panels (b) and (d) illustrate the case where $V = 2V_c$. As can be seen, the presence of an applied potential can result in (i) collimation of the electron beam at the interface [panels (a) and (b)] and (ii) interruption of the current between the input and output leads [panels (c) and (d)].

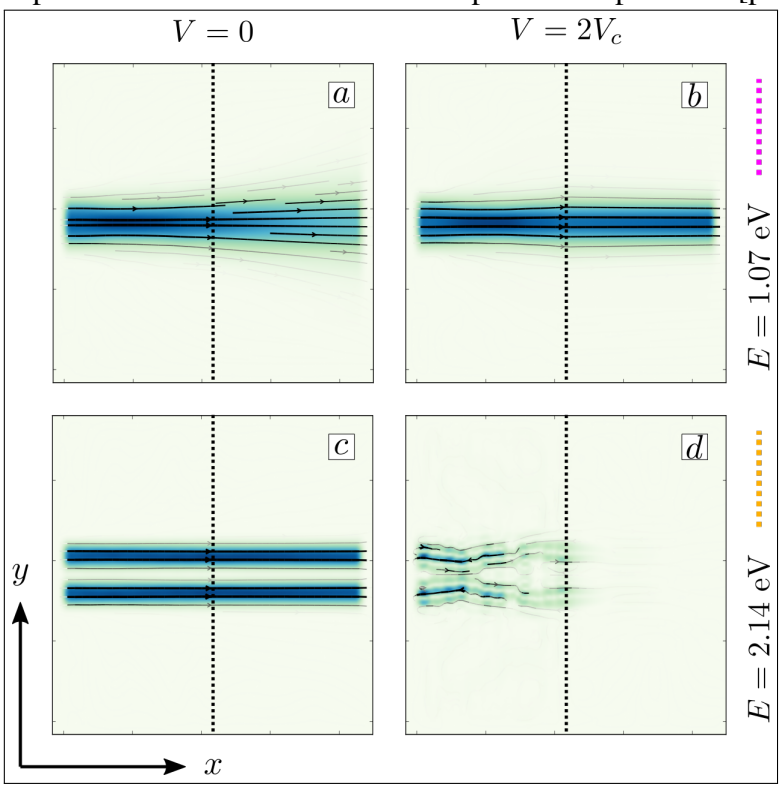

Source: Figure elaborated by the author (2023).

the behavior qualitatively similar to the case where the lateral leads are absent. In phosphorene junctions with zigzag interfaces (armchair edges) conductances approaching zero are observed for certain values of Fermi energy. This is due to the inversion of the concavity of the subbands at these Fermi energy values in bilayer region with the appearance of quasi-flat subbands at the transition threshold. Such an effect is absent in phosphorene junctions with armchair interfaces (zigzag edges). This difference in conductance behavior for the zigzag and armchair cases is therefore due to the anisotropy in the phosphorene band structure, which implies subbands with different aspects. The possibility of modulating the current in an electronic device through gate potentials is essential for the development of logic gates. In this sense, we explore in more detail the substantial reduction of conductance for specific Fermi energy values, as shown in Figure 24(a)-(d) for phosphorene junctions with zigzag interfaces. For that, we analyze the behavior of the probability current density taking two specific values for the Fermi energy, namely, $E = 1.07$ eV and $E = 2.14$ eV represented by the pink and yellow dashed lines, respectively, in Fig.

Figure 26 – (Color online) Probability current densities for the phosphorene junction considered in panel (g) of Fig. 24. We take three specific values for the Fermi energy, namely, $E = 1.23$ eV [panels (a), (b), and (c)], $E = 1.55$ eV [panels (d), (e), and (f)], and $E = 2.14$ eV [panels (g), (h), and (i)]. Panels (a), (d), and (g) illustrate the case where $V = 0$, panels (b), (e), and (h) illustrate the case where $V = V_c$, and panels (c), (f), and (i) illustrate the case where $V = 2V_c$. As can be seen, the presence of an applied potential can result in collimation of the electron beam at the interface.

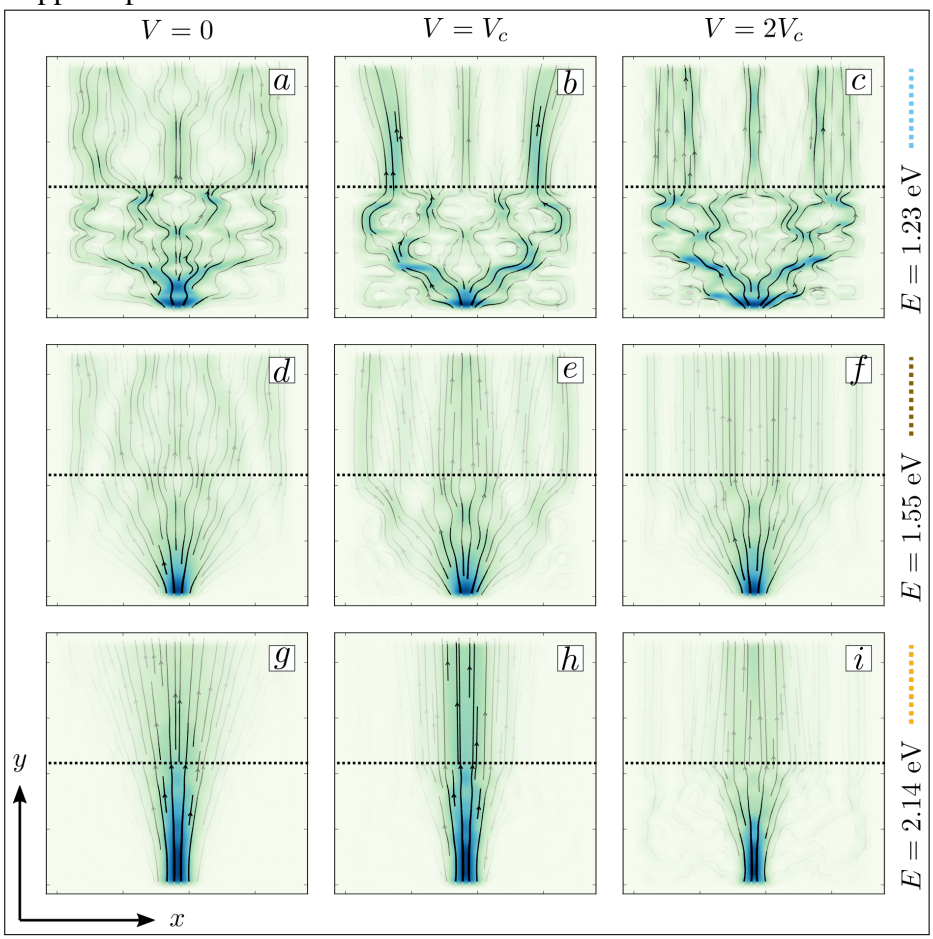

Source: Figure elaborated by the author (2023).

24(c). Fig. 25 shows the probability current density for these two specific Fermi energy values considering $V = 0$ [Figure 25(a) and 25(c)] and $V = 2V_c$ [Figure 25(b) and 25(d)]. By Figure 25(a) and 25(b) it can be seen that the applied potential can collimate the electron beam at the interface at $E = 1.07$ eV. This can be verified by panel (d) of Fig. 24, where it is noted that the conductance between the input and output leads for $V = V_c$ or $V = 2V_c$ in the range $1.0 < E < 2.0$ eV is greater than that conductance for $V = 0$. This is due to the fact that collimation at the interface reduces the number of electrons collected by the lateral leads, increasing the number of electrons transmitted from the input lead to the output lead. On the other hand, for $E = 2.14$ eV, it can be seen by Figure 25(c) and 25(d) that the current is interrupted by the application of the potential $V = 2V_c$, and this is in agreement with panel (c) of Fig. 24, in which a substantial

reduction is observed for this Fermi energy.

Let us now consider the case where the interface is armchair and therefore the edge is zigzag in Fig. 26. We present the probability current densities for three specific values for the Fermi energy, namely, $E = 1.23$ eV (blue dashed line) which corresponds to a jump from the first to the second conductance plateau, $E = 1.55$ eV (brown dashed line) which corresponds to an approximately constant range from the end of the second conductance plateau, and $E = 2.14$ eV (yellow dashed line) which also represents an approximately constant range, but from the beginning of the fourth conductance plateau, as shown in Fig. 24(g). Due to the qualitative similarity between the results of panels (c) and (g) of Fig. 24 for $0 < E < 1.5$ eV, it is expected that the probability current densities in these two cases are also qualitatively similar, except for the case where $E = 1.23$ eV, as it is located at a jump between two consecutive plateaus, as seen by comparing panel (a) of Fig. 25 with panels (a), (d), and (g) of Fig. 26. The effect of the presence of an external field, as in the case of a zigzag interface, is to collimate the electron beam at the interface, as presented in Figure 26(b), 26(e), and 26(h) for $V = V_c$ and in Figure 26(c), 26(f), and 26(i) for $V = 2V_c$. The collimation is more pronounced as the value of the potential increases. The next phosphorene junction we study is the one formed by two monolayer portions coupled to a single bilayer portion, as shown in Fig. 22(e). As the band gap of the monolayer region is larger than that of the bilayer region in the absence of external fields, the lower subbands in the three portions act as a potential well for electrons injected by the input lead with Fermi energies greater than the lowest subband of the bilayer region and as a potential barrier for holes with Fermi energies greater than the lowest subband of the monolayer region. This implies, as in the MB case previously analyzed, in an electron-hole symmetry, which can be broken by the application of a potential. Fig. 27 shows the conductance as a function of Fermi energy for the MBM phosphorene junction, both with zigzag interface [Figure 27(a)-(f)] and armchair interface [Figure 27(g)-(l)], taking various parameter settings. In panels from (a) to (d) and from (g) to (j) of Fig. 27, we take three values for the applied potential, $V = 0$ represented by the black curve, $V = V_c$ represented by the blue curve, and $V = 2V_c$ represented by the red curve. In panels (e), (f), (k), and (l) we take three values for the domain wall length, which is the region delimited by the bilayer, namely, $L \approx 10$ nm represented by the yellow curve, $L \approx 20$ nm represented by the pink curve, and $L \approx 40$ nm represented by the green curve. Domain wall interfaces can be aligned or anti-aligned. Thus, in Fig. 27 we consider aligned interfaces in panels (a), (b), (g), and (h), and anti-aligned interfaces in all other panels. As can be seen

Figure 27 – (Color online) Conductances, in units of e^2/h, as a function of Fermi energy, in units of eV, of MBM phosphorene junctions. Three values for the applied potential were taken in panels from (a) to (d) and from (g) to (j), namely, $V = 0$ represented by the black curve, $V = V_c$ represented by the blue curve, and $V = 2V_c$ represented by the red curve, and three values for the domain wall length were taken in panels (e), (f), (k), and (l), namely, $L \approx 10$ nm represented by the yellow curve, $L \approx 20$ nm represented by the pink curve, and $L \approx 40$ nm represented by the green curve. Panels from (a) to (f) [from (g) to (l)] refer to zigzag [armchair] interfaces. In panels (b), (d), (f), (h), (j), and (l) we consider the input lead width to be smaller than the scattering region width. We consider both the case where the domain wall interfaces are aligned and the case where they are anti-aligned.

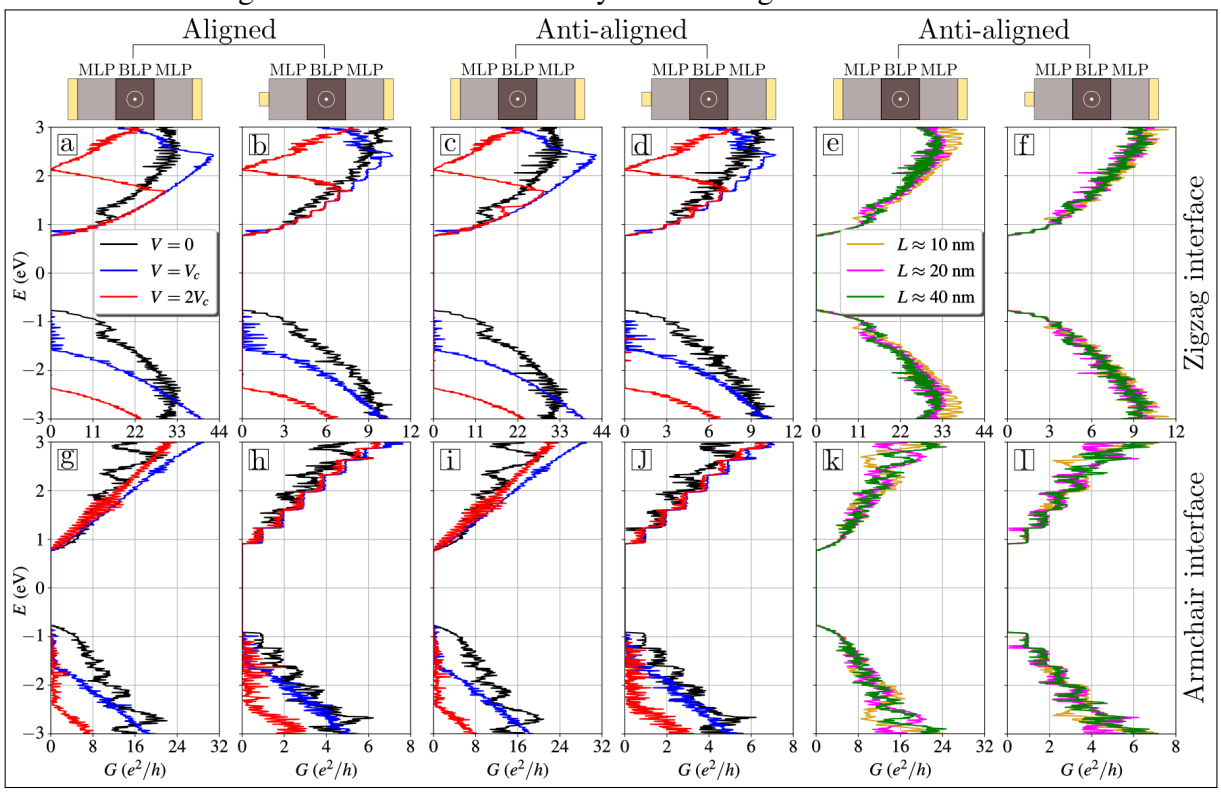

Source: Figure elaborated by the author (2023).

comparing, for example, panels (a, b) with panels (c, d) of Fig. 27, the alignment/anti-alignment weakly influences the transport of charge carriers and the effect of reducing the width of the input lead in MBM phosphorene junctions is qualitatively similar to that in MB phosphorene junctions discussed previously. Furthermore, as can be seen by comparing panels (e) and (f) or panels (k) and (l) of Fig. 27, varying the length of the domain wall weakly influences the transport of electrons and holes in the phosphorene junction considered. Finally, we investigate the BMB phosphorene junction shown in Fig. 22(f). As in the previous case, we take three values for the applied potential ($V = 0$, $V = V_c$, and $V = 2V_c$), three values for the domain wall length ($L \approx 10$ nm, $L \approx 20$ nm, and $L \approx 40$ nm), and we verified the effect of the interface alignment/anti-alignment as well as the influence of the interface type on the transport properties.

Figure 28 – (Color online) Conductances, in units of e^2/h, as a function of Fermi energy, in units of eV, of BMB phosphorene junctions. Three values for the applied potential were taken in panels from (a) to (d) and from (g) to (j), namely, $V = 0$ represented by the black curve, $V = V_c$ represented by the blue curve, and $V = 2V_c$ represented by the red curve, and three values for the domain wall length were taken in panels (e), (f), (k), and (l), namely, $L \approx 10$ nm represented by the yellow curve, $L \approx 20$ nm represented by the pink curve, and $L \approx 40$ nm represented by the green curve. Panels from (a) to (f) [from (g) to (l)] refer to zigzag [armchair] interfaces. In panels (b), (d), (f), (h), (j), and (l) we consider the input lead width to be smaller than the scattering region width. We consider both the case where the domain wall interfaces are aligned and the case where they are anti-aligned.

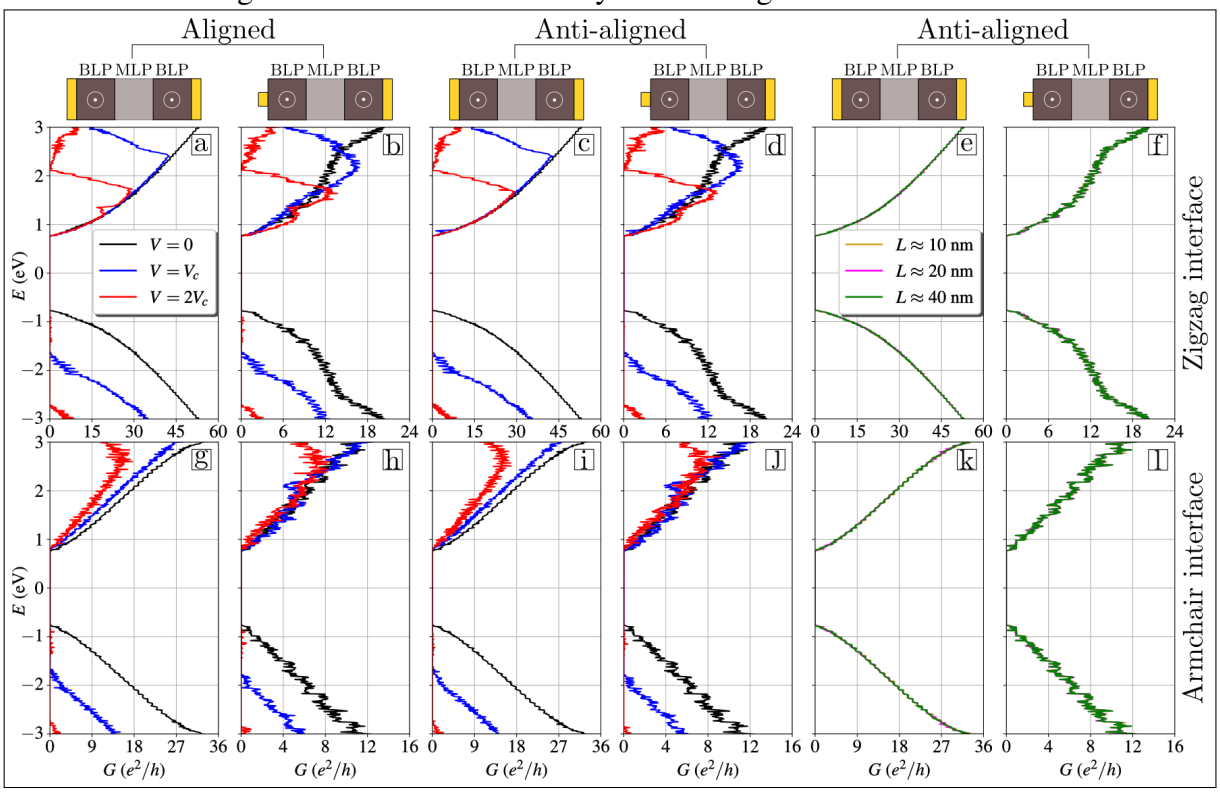

Source: Figure elaborated by the author (2023).

In addition, the reduction of the input lead width was considered in panels (b), (d), (f), (h), (j), and (l). As noted, a substantial reduction in conductance in relation to Fermi energy is present in the case of zigzag interface for the three phosphorene junctions studied. Furthermore, the fact that the domain wall interfaces in the MBM and BMB cases are aligned or anti-aligned will not considerably affect the transport properties as well as increasing the domain wall length. In the MBM and BMB cases, the reduction of the input lead width qualitatively maintains the functional dependence of G with E shown in the case where the lead width and the scattering region width are equal. However, for the case where the lead width is smaller, the value of G is reduced due to the fact that the number of occupied subbands is smaller. In view of the results presented in this work, it is noted that the phosphorene junctions studied here can act as

electronic devices capable of modulating the current between the input lead and the output lead in the case of zigzag interface, making it a candidate for use in nanoelectronic applications as a low power field effect transistor as it acts as a scattering region where the current is tuned by the application of a potential.

9 OPTICAL PROPERTIES OF MULTILAYER PHOSPHORENE

9.1 Motivation

In this work, we investigate semianalytical optic transitions of multilayer phosphorene close to the Fermi level. We combine a model based on the continuum approximation by the tight-binding method, which uses 15 hoppings parameters for the first neighbors, with the first-order light-matter interaction by many-body formalism. Rewritten the generalized Hamiltonian for phosphorene multilayer one can obtain the generalized wave function. From the point of view of the many-body theory, this makes it possible to calculate the first order of approximation of the interaction Hamiltonian and thereby obtain the two-dimensional dielectric function extracted through Fermi's golden rule. The transition peaks for a few layers agree well with experimental data and one possibility to make a clear distinction to each transition. The model provides a good forecast of transitions for a greater number of piles, where the nearby peaks of transition energy mix strongly due to the relationship of the delta function to the dielectric function, making it impossible to distinguish further. In addition, we could also observe a slight decrease in the lowest energy peaks when we consider the system with temperature T = 300K, which is characteristic of semiconductors. Our work indicates new theoretical possibilities for extracting electronic, transport and optoelectronic properties in phosphorene multilayers.

9.2 Results and discussions

The Hamiltonian $\mathscr{H}^n$ in section 2.4 provides the electronic band structure for multilayer phosphorene. At the Γ point, the values for the gap agree well with experimental results (Zhang *et al.*, 2017). For the wave function used in section 2.4, the Hamiltonian is rewritten as in Jr & Katsnelson (2015), and with that, we can find an expression analytically to interaction potential by Feynman-Helman approximation, as we can see below.

$$\mathbf{P}^{vc}(k) = \left(\frac{m}{\hbar}\right) \langle \psi_{v,k} | \nabla_k H(k) | \psi_{c,k} \rangle = \mathbf{P}_x^{vc}(k) + \mathbf{P}_y^{vc}(k), \tag{9.1}$$

where

$$\mathbf{P}_x^{vc}(k) = \left(\frac{i2m}{\hbar}\right) \gamma_x k_x \sin\theta_k \hat{\mathbf{x}} \tag{9.2}$$

and

$$\mathbf{P}_y^{vc}(k) = \left(\frac{im}{\hbar}\right)(2\gamma_y k_y \sin\theta_k + X\cos\theta_k)\hat{\mathbf{y}} \tag{9.3}$$

Thereby, the total polarizability $\mathbf{P}^{vc}(\mathbf{k})$, Eq. 9.1, was calculated using the wave function and Hamiltonian of the section 2.4 and plotted in Figure 29. **X**-part of $\mathbf{P}^{vc}(\mathbf{k})$ present symmetric regions in the Brillouin zone phase space. It is suggesting that the polarized light in x-direction can improve the electron transition in multilayer phosphorene. For **Y**-part of $\mathbf{P}^{vc}(\mathbf{k})$, the anisotropic characteristic of the phosphorene appears clearly. The total 2D dielectric function,

Figure 29 – Momentum matrix elements to four layers [arbitrary units]: **X**-part of $\mathbf{P}^{vc}(\mathbf{k})$ (bottom) presents symmetric regions in the Brillouin zone phase space. The polarized light in x-direction can improve the electron transition in multilayer phosphorene. **Y**-part of $\mathbf{P}^{vc}(\mathbf{k})$ (top), the anisotropic characteristic of the phosphorene around the Γ point in the y-dierection is evident.

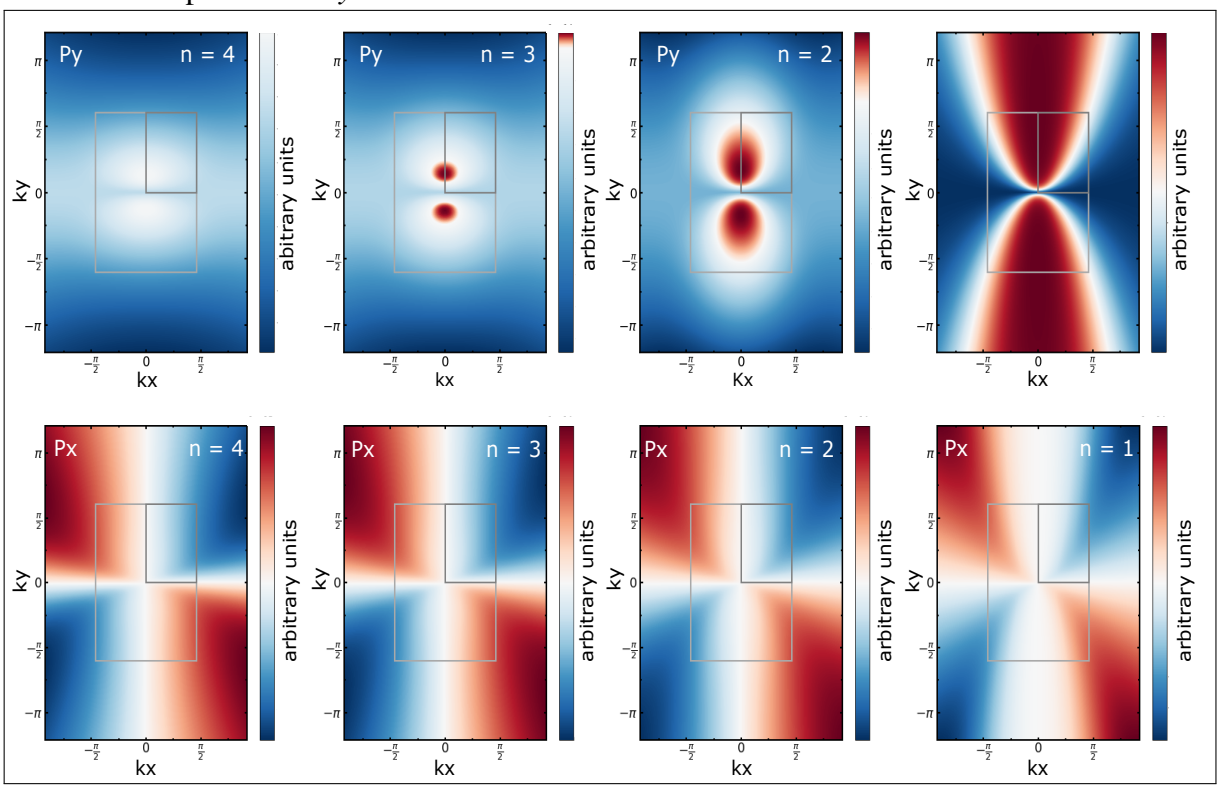

Source: Figure elaborated by the author (2023).

Eq. 9.2, was resolved semianalytical, where the delta function, $\delta(Ec - Ev)$, is responsible for the transition between intraband energy in the Γ point. The E_v represents the valence band energy and E_c is the conduction band energy. Figure 30 shows energies de transition between bands for a system with three layers. The orange line represents the total 2D dielectric function for T = 0,

which corresponds to the sum of all individual dielectric functions.

$$\varepsilon_2(\omega) = \frac{4\pi^2 e^2}{m^2\omega^2}\sum_{cv}\int_{BZ}\frac{d^2k}{(2\pi)^2}|\lambda\cdot\mathbf{P}^{vc}(\mathbf{k})|^2\delta[E_c(\mathbf{k}) - E_v(\mathbf{k}) - \hbar\omega], \tag{9.4}$$

The blue line indicates a peak corresponding to the E_{11} transition, i.e., the transition from the highest band in the valence band to the lowest band in the conduction band. Each line is a partial dielectric function with a transition peak characterized by the function $\delta(Ec - Ev)$. The other transitions are explained in the figure's caption. For two and three layers, this distinction is quite clear, and it is possible to identify each individual transition peak, as seen in Figure 9.2. However, for more than three layers, the transition peaks are very close to each other, and their mixture becomes indistinguishable when summed, making it difficult to precisely identify the transitions. Nevertheless, it is evident that there are transitions with certain energies determined by the presence of peaks. For a three-layer system, the E_{11} transition with an energy of around 0.85 eV and the E_{21} transition with an approximate energy of 1.30 eV agree well with experimental results [fingerprints]. It is worth mentioning that a more in-depth discussion is needed regarding the origin of the peaks intraband, since the Hamiltonian for n-layers is decoupled, the eigenstates for each layer are orthogonal functions.

Regarding temperature (Haug; Koch, 2009), the dielectric function takes form

$$\varepsilon_2(w) = \frac{4\pi^2 e^2}{m^2\omega^2}\sum_{cv}\int_{BZ}\frac{d^2k}{(2\pi)^2}|\lambda.\mathbf{P}^{vc}(k)|^2.(1 - f_c - f_v)\delta(E_c(k) - E_v(k) - \hbar\omega), \tag{9.5}$$

where f_c (f_v) is the Fermi-Dirac distribution for the conduction (valence) band. In Figure 30 (b), the orange line represents the dielectric function at T = 0K, while the green line shows the dielectric function at temperature T = 300K. The Fermi level was considered a good approximation at the center of the bandgap. For systems with more than one layer, transitions with lower energies clearly decrease with increasing temperature, exhibiting the characteristic temperature effect observed in semiconductors. For two layers, the temperature effect appears only in the E_{11} peak, which has the lowest energy, causing a slight decrease in its energy value. The subsequent peaks, E_{12}, E_{21}, and E_{22}, are not affected by temperature and complete the total number of transitions for the bilayer system. In the case of trilayers, the E_{11} and E_{21} peaks are affected by temperature, while the rest remain unaffected. Increasing the number of layers expands the energy range affected by temperature. In general, for a few layers of phosphorene, the transition peaks agree well with experimental and theoretical results (Zhang *et al.*, 2017; Watts *et al.*, 2019), and the

Figure 30 – (a) The total 2D dielectric function of multilayer phosphorene calculated for 3 layers at T = 0K. The orange line corresponds to the sum of all individual dielectric functions, where each line is a partial dielectric function with a transition peak characterized by the function $\delta(Ec - Ev)$. (b) The total 2D dielectric function of multilayer phosphorene was calculated for 3 layers at T = 300K. Increasing the number of layers expands the energy range affected by temperature.

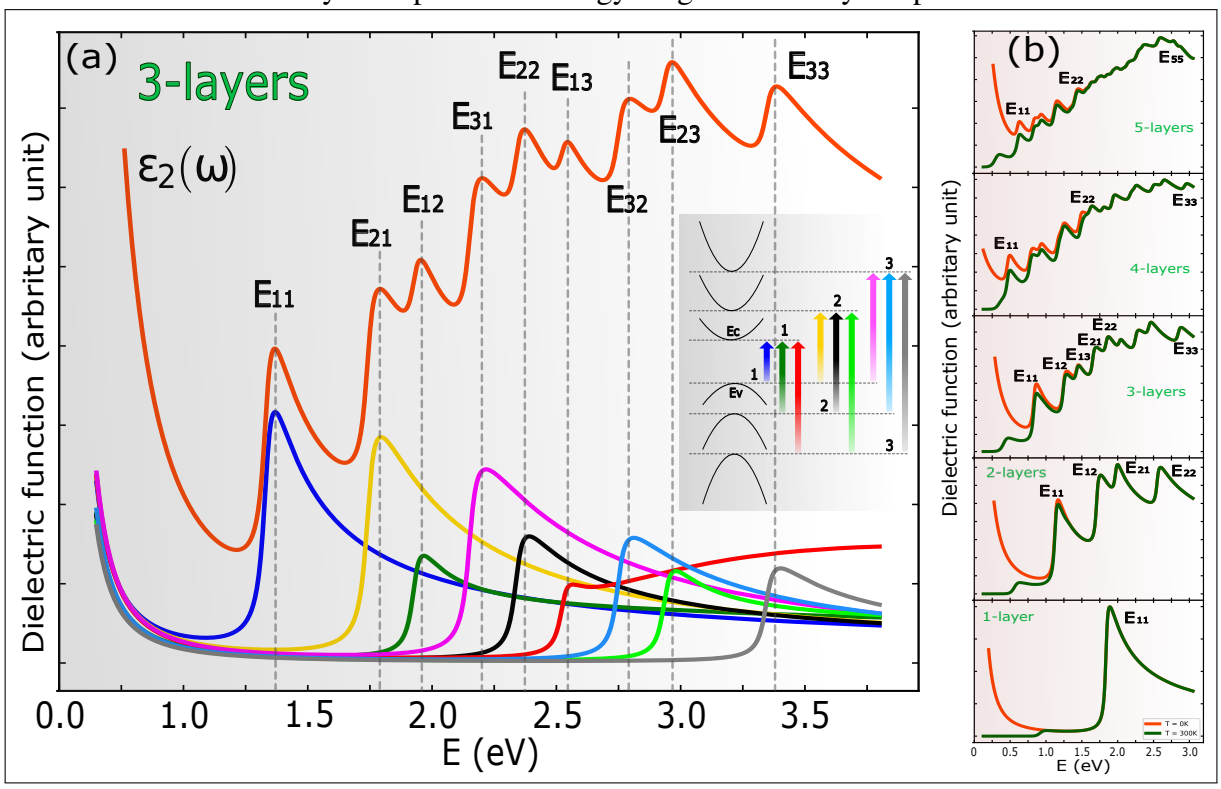

Source: Figure elaborated by the author (2023).

transitions affected by the temperature at T = 300K are mainly the lower-energy transitions in systems with two or more layers.

9.3 Conclusions

The total polarizability provides information despite the electron transition in multilayer phosphorene. **X**-part of $\mathbf{P}^{vc}(\mathbf{k})$ present symmetric regions in the Brillouin zone phase space, suggesting that the polarized light in x-direction can improve the electron transition. For **Y**-part of $\mathbf{P}^{vc}(\mathbf{k})$, the anisotropic characteristic known of the phosphorene appears clearly. For a three-layer system, the E_{11} transition with an energy of around 0.85 eV and the E_{21} transition with an approximate energy of 1.30 eV agree well with experimental results [fingerprints]. It is worth mentioning that a more in-depth discussion is needed regarding the origin of the peaks intraband, since the Hamiltonian for n-layers is decoupled, the eigenstates for each layer are orthogonal functions. Considering the temperature, increasing the number of layers expands the

energy range affected by temperature. In general, for a few layers of phosphorene, the transition peaks agree well with experimental and theoretical results (Zhang *et al.*, 2017; Watts *et al.*, 2019), and the transitions affected by the temperature at T = 300K are mainly the lower-energy transitions in systems with two or more layers.

10 CONCLUSIONS AND PERSPECTIVES

10.1 Final remarks on the band unfolding formalism

In view of possible future phosphorene-based electronic devices and the fact that the defects and lattice deformations are inherent and hard to be avoided in the isolation/fabrication of 2D materials, it is paramount to investigate the effects of point defects on the electronic properties of multilayer phosphorene. Despite the vast literature regarding different theoretical and experimental research on defective phosphorene, to our knowledge, there was a lack of a systematic, appropriate, and carefully taken study on the band unfolding process to deal with large supercells by considering multiple vacancies in multilayer phosphorene and the obtention of their non-duplicated band structures in the reciprocal space in the presence of point defects. In this context, in the first part of this thesis, we presented the usage of the theoretical framework based on the combination of the tight-binding model and the band unfolding formalism to investigate the vacancy-induced changes in the band structures of the monolayer, bilayer, and trilayer phosphorene. Different vacancy formations were assumed by removing phosphorous atoms keeping or not the sublattice symmetry of the equivalent sublattices (A/D and B/C associated with the D_{2h}-symmetry) in multilayer BP. Different layer locations inside the supercell were also considered, assuming them in the same or different layers to form single, double, and triple vacancies. Our findings demonstrated that: (i) the presence of an almost n-fold degenerate quasi-flat state in a system with n vacancies when the sublattice symmetry and/or sublayer (inversion) symmetry are broken; (ii) the occurrence of atomic vacancies in the supercell also affects the energetic position of the bulk states, especially the large is the vacancy concentration; (iii) the unfolding formalism is clearly able to exhibit the defective band structure of multilayer phosphorene and a 6×6-supercell is sufficient for electronic calculations with a low vacancy concentration.

Regarding the use of the unfolding technique for the case of BP nanoribbons, one verified by projecting the BP nanoribbon energy levels into the infinite-sheet bulk states that: (i) the unfolding technique can clearly describe the discretized energy levels along the confinement direction of the ribbon and the continuum of projected states associated with the translational symmetry direction; and (ii) additional modes were observed in the middle gap induced by defects in the nanoribbon-sized supercell for both zigzag and armchair nanoribbon cases.

10.2 Final remarks on the transport and optical properties

Taking advantage of the fact that in the fabrication of samples made out of 2D materials, it is very challenging to obtain perfectly crystalline structures over large areas, being difficult to avoid the appearance of defects and grain boundaries, as well as on the high control of the number of layers, then we investigated lateral junctions composed by monolayer and bilayer BP portions on the same sample. Our motivation arose from similar works on few-layered graphene samples with monolayer and bilayer patches aligned with the possibility of controlling the transport properties via anisotropy ingredients in anisotropic semiconductors, such as a few-layered BP sample.

For this part of the thesis, we systematically studied the electronic transport properties of monolayer-bilayer, monolayer-bilayer-monolayer, and bilayer-monolayer-bilayer phosphorene junctions based on a tight-binding approach utilizing five intralayer and one interlayer hopping parameters. Two different types of interfaces were considered: armchair and zigzag interfaces. By comparing the zigzag and armchair interface-type results of the conductance and probability current densities, one could demonstrate highly anisotropic transport features, *i.e.* an orientation-dependence on the propagating mode and equivalently to the interface type. By applying a perpendicular electric field in the bilayer portions, one allowed tuning the energetic propagating channel in the scattering region and even in some cases lead to the collimation of the injected modes. This control in the collimation of the incident modes and in the conductance was due to the energetic adjustment of the energy levels in the mono and bilayer BP ribbons patches achieved by the fact that the electric field close the gap in the bilayer BP portion and shift the bands in monolayer case.

In the last part of this thesis, by calculating the energy bands of multilayer phosphorene via a single-orbital multi-hopping tight-binding model, we discussed allowed optic transitions in the perspective of the dielectric function extracted from Fermi's golden rule and momentum matrix elements. We identified each transition peak in the dielectric function according to the energetic inter-subband difference. Such a study was done by assuming a different number of BP layers, and the results were compared to the ones previously reported in the literature, showing a good qualitative agreement.

10.3 Some very near-future perspectives

Below, it is enumerated some of my perspectives associated with this thesis in priority order in view of how close they are to being complete:

1 To continue the theoretical investigation via unfolding formalism on the defect effects in the electronic properties of phosphorene nanoribbons with zigzag and armchair edges and by considering different types of removing the P atoms.

2 To extend the investigation of point defects using the unfolding formalism for the case of twisted bilayer graphene. So far, we have not found any work in the literature that has systematically studied defects for different twist angles and for different types of point defects.

3 To conclude the work on optical properties of multilayer phosphorene, investigating in more detail the excitonic aspects.

REFERENCES

ABDULLAH, H. *et al.* Quantum transport across van der waals domain walls in bilayer graphene. **Journal of Physics:** Condensed Matter, [*s. l.*], v. 29, n. 42, p. 425303, 2017. Available at: https://iopscience.iop.org/article/10.1088/1361-648X/aa81a8. Access in: 16 nov. 2018.

ABDULLAH, H. *et al*. Electronic transport and klein tunneling in gapped aa-stacked bilayer graphene. **Journal of Applied Physics**, [*s. l.*], v. 124, n. 20, p. 204303, 2018. Available at: https://pubs.aip.org/aip/jap/article-abstract/124/20/204303/948688/Electronic-transport-and-Klein-tunneling-in-gapped?redirectedFrom=fulltext. Access in: 3 jun. 2019.

ABDULLAH, H. M. *et al*. Electron collimation at van der waals domain walls in bilayer graphene. **Physical Review B**, [s. l.], v. 100, n. 4, p. 045137, jul. 2019. Available at: https://doi.org/10.1103/PhysRevB.100.045137. Access in: 10 dez. 2019.

ABU, U. O. *et al*. Ultra-narrow phosphorene nanoribbons produced by facile electrochemical process. **Advanced Science**, [*s. l.*], v. 9, n. 31, p. 2203148, nov. 2022. Available at: https://www.bi.nlm.nih.gov/pmc/articles/PMC9631066/. Access in: 16 abr. 2022.

ADDOU, R.; COLOMBO, L. (ed.) **Defects in two-dimensional materials**. Amsterdam: Elsevier, 2022.

AGHAJANIAN, M.; MOSTOFI, A. A.; LISCHNER, J. Electronic structure of monolayer and bilayer black phosphorus with charged defects. **Physical Review Materials**, [*s. l.*], v. 6, n. 4, p. 044002, apr. 2022. Available at: https://doi.org/10.1103/PhysRevMaterials.6.044002. Access in: 01 out. 2022.

AHMAD, W. *et al.* Introduction, production, characterization and applications of defects in graphene. **Journal of Materials Science:** materials in electronics, [*s. l.*], v. 32, n. 15, p. 19991–20030, 2021. Available at: https://link.springer.com/article/10.1007/s10854-021-06575-1. Access in: 16 nov. 2022.

AHUJA, R. Calculated high pressure crystal structure transformations for phosphorus. **Physica Status Solidi (b)**, [*s. l.*], v. 235, n. 2, p. 282–287, fev. 2003. Available at: https://onlinelibrary.wiley.com/doi/abs/10.1002/pssb.200301569. Access in: 30 nov. 2019.

AKAHAMA, Y.; ENDO, S.; NARITA, S.- I. Electrical properties of black phosphorus single crystals. **Journal of the Physical Society of Japan**, Japan, v. 52, n. 6, p. 2148–2155, 1983. Available at: https://www.jstage.jst.go.jp/article/jpsj1946/52/6/52_6_2148/_article/-char/ja/. Access in: 30 nov. 2019.

AKHTAR, M. *et al*. Recent advances in synthesis, properties, and applications of phosphorene. **npj 2D Materials and Applications**, London, v. 1, n. 1, p. 5, 2017. Available at: https://www.nature.com/articles/s41699-017-0007-5. Access in: 30 nov. 2019.

ALDAVE, S. *et al.* Characterization and sonochemical synthesis of black phosphorus from red phosphorus. **2D Materials**, [*s. l.*], v. 3, n. 1, p. 014007, feb. 2016. Available at: https://iopscience.iop.org/article/10.1088/2053-1583/3/1/014007/meta. Access in: 30 nov. 2019.

ALLEN, P. *et al*. Recovering hidden bloch character: Unfolding electrons, phonons, and slabs. **Physical Review B**, [*s. l.*], v. 87, n. 8, p. 085322, 2013. Available at: https://journals.aps.org/prb/abstract/10.1103/PhysRevB.87.08532. Access in: 30 jun. 2019.

AMINI, M. *et al*. Quantum transport through the edge states of zigzag phosphorene nanoribbons in presence of a single point defect: analytic green's function method. **Journal of Physics**: condensed matter, [*s. l.*], v. 31, n. 21, p. 215301, 2019. Available at: https://iopscience.iop.org/article/10.1088/1361-648X/ab09b8/meta. Access in: 03 jul. 2022.

AMINI, M.; SOLTANI, M.; SHARBAFIUM, M. Vacancy-induced fano resonances in zigzag phosphorene nanoribbons. **Physical Review B**, [*s. l.*], v. 99, n. 8, p. 085403, feb. 2019. Available at: https://journals.aps.org/prb/abstract/10.1103/PhysRevB.99.-085403. Access in: 03 jul. 2022.

ARAÚJO, F. R. V. *et al*. Current modulation in graphene p–n junctions with external fields. **Journal of Physics**: condensed matter, [*s. l.*], v. 32, n. 42, p. 425501, 2020. Available at: https://iopscience.iop.org/article/10.1088/1361-648X/ab9cf1/meta. Access in: 03 jul. 2022

ARAÚJO, F. R. V. *et al*. Gate potential-controlled current switching in graphene y-junctions. **Journal of Physics:** condensed matter, [*s. l.*], v. 33, n. 37, p. 375501, jul. 2021. Available at: https://iopscience.iop.org/article/10.1088/1361648X/ac0f2b/meta Access in: 3 jul. 2022.

ARAÚJO, F. R. V. *et al*. Modulation of persistent current in graphene quantum rings. **Journal of Physics:** condensed matter, IOP Publishing, [s.l.], v. 34, n. 12, p. 125503, jan. 2022. Available at: https://iopscience.iop.org/artcle/10.1088/136164-8X-/ac452e/meta. Access in: 10 jul. 2022.

ARAUJO, P. T. *et al*. Defects and impurities in graphene-like materials. **Materials Today**, [*s. l.*], v. 15, n. 3, p. 98–109, mar. 2012. Available at: https://www.science-direct.com/science/article/pii/S1369702112700457. Access in: 16 jul. 2018.

ARRA, S.; BABAR, R.; KABIR, M. Exciton in phosphorene: strain, impurity, thickness, and heterostructure. **Physical Review B**, [*s. l.*], v. 99, n. 4, p. 045432, jan. 2019. Available at: https://journals.aps.org/prb/abstract/10.1103/PhysRevB.99.0454-32. Access in: 20 jul. 2019.

ASHCROFT, N. W.; MERMIN, N. D. **Solid state physics**. Australia: Cengage Learning, 2022.

ASHLEY, K.; CORDELL, D.; MAVINIC, D. A brief history of phosphorus: from the philosopher's stone to nutrient recovery and reuse. **Chemosphere**, [*s. l.*], v. 84, n. 6, p. 737–746, aug. 2011. Available at: https://www.sciencedirect.com/science/-artic-le/abs/pii/S004-5653511002499. Access in: 16 nov. 2019.

AVERBUCH-POUCHOT, M. T.; DURIF, A. **Topics in phosphate chemistry**. Singapure: World Scientific, 1996.

AVOURIS, P.; XIA, F. Graphene applications in electronics and photonics. **Mrs Bulletin**, Cambridge, v. 37, n. 12, p. 1225–1234, 2012. Available at: https://doi.org/10.1557/mrs20-12.206. Access in: 3 dez. 2020.

AVSAR, A. et al. Air-stable transport in graphene-contacted, fully encapsulated ultrathin black phosphorus-based field-effect transistors. **ACS nano**, [*s. l.*], v. 9, n. 4, p. 4138–4145, 2015. Available at: https://pubs.acs.org/doi/abs/10.1021/acsnano.5-b00289. Access in: 13 jul. 2019.

BABA, M. *et al*. Preparation of black phosphorus single crystals by a completely closed bismuth-flux method and their crystal morphology. **Japanese journal of applied physics**, Japan, v. 28, n. 6R, p. 1019, 1989. Available at: https://iopsci-ence.iop.org/article/10.1143/JJ-AP.28.1019/meta. Access in: 1 mar. 2020.

BABA, M. *et al*. Electrical properties of black phosphorus single crystals prepared by the bismuth-flux method. **Japanese journal of applied physics**, Japan, v. 30, n. 8, p. 1753 - 1758, aug. 1991. Available at: https://journals.aps.org/prb/abstract/10.1-103/PhysRevB.-97.045132. Access in: 15 mar. 2020.

BABAR, R.; KABIR, M. Engineering the kondo state in two-dimensional semiconducting phosphorene. **Physical Review B**, [*s.l.*], v. 97, n. 4, p. 045132, jan. 2018. Available at: https://journals.aps.org/prb/abstract/10.1103/PhysRevB.97.045-132. Access in: 15 jul. 2019.

BAIK, S. S. *et al*. Emergence of two-dimensional massless dirac fermions, chiral pseudospins, and berry's phase in potassium doped few-layer black phosphorus. **Nano letters**, [*s.l.*], v. 15, n. 12, p. 7788–7793, 2015. Available at: https://pubs.acs.org/doi/abs/10.102-1/acs.nanolett.5b04106. Access in: 15 jul 2019.

BAKER, I. **Fifty materials that make the world**. Switzerland: Springer, 2018.

BANHART, F.; KOTAKOSKI, J. KRASHENINNIKOU, A. V. Structural defects in graphene. **ACS nano**, [*s. l.*], v. 5, n. 1, p. 26–41, nov. 2011. Available at: https://pub-s.acs.org/doi/abs/10.1021/nn102598m. Access in: 9 dez 2020.

BASSANI, F. *et al*. Electronic states and optical transitions in solids. **Physics Today**, [*s. l.*], v. 29, n. 3, p. 58 - 59, 1976. Available at: https://doi.org/10.1063/1.30-23374. Access in: 13 may 2019.

BERKELBACH, T. C.; HYBERTSEN, M. S.; REICHMAN, D. R. Bright and dark singlet excitons via linear and two-photon spectroscopy in monolayer transition-metal dichal-cogenides. **Physical Review B**, [*s. l.*], v. 92, n. 8, p. 085413, aug. 2015. Available at: https://pubs.aip.org/physicstoday/article-abstract/29/3/58/43041-6/Electronic-States-and-Optical-Transitions-in. Access in: 23 jun. 2019.

BERTOLDO, F. *et al*. Quantum point defects in 2d materials-the qpod database. **npj Computational Materials**, London, v. 8, n. 1, p. 56, 2022. Available at: https://www.-nature.com/articles/s41524-022-00730-w. Access in: 02 dez. 2022.

BETANCUR-OCAMPO, Y.; LEYVRAZ, F.; STEGMANN, T. Electron optics in phos-phorene pn junctions: negative reflection and anti-super-klein tunneling. **Nano Letters**, [*s. l.*], v. 19, n. 11, p. 7760–7769, 2019. Available at: https://pubs.acs.org/doi/abs/10.1021/ac-s.nanolett.9b02720. Access in: 20 nov. 2020.

BOYKIN, T. B.; KLIMECK, G. Practical application of zone-folding concepts in tight-binding calculations. **Physical Review B**, [*s. l.*], v. 71, n. 11, p. 115215, mar. 2005. Available at: https://journals.aps.org/prb/abstract/10.1103/PhysRevB.71.115215. Access in: 15 jul. 2019.

BOYKIN, T. B. *et al.* Approximate bandstructures of semiconductor alloys from tight-binding supercell calculations. **Journal of Physics**: condensed matter, [*s. l.*], v. 19, n. 3, p. 036203, jan. 2007. Available at: https://iopscience.iop.org/article/10.1088/09538984/1-9/3/036203/meta. Access in: 15 jul. 2019.

BOYKIN, T. B. *et al*. Unfolding and effective bandstructure calculations as discrete real-and reciprocal-space operations. **Physica B:** condensed matter, [*s. l.*], v. 491, p. 22–30, 2016. Available at: https://www.sciencedirect.com/science/article/abs/pii/S-0921452616300801. Access in: 16 jul. 2019.

BRENT, J. R. *et al.* Production of few-layer phosphorene by liquid exfoliation of black phosphorus. **Chemical communications**, [*s. l.*], v. 50, n. 87, p. 13338–13341, 2014. Available at: https://pubs.rsc.org/en/content/articlehtml/2014/cc/c4cc05752j. Access in: 31 sep. 2020.

BREY, L.; FERTIG, H. A.; SARMA, S. das. Diluted graphene antiferromagnet. **Physical Review Letters**, [*s. l.*], v. 99, n. 11, p. 116802, sep. 2007. Available at: https://journals.aps.org/prl/abstract/10.1103/PhysRevLett.99.116802. Access in: 31 jul. 2019.

BRIDGMAN, P. Two new modifications of phosphorus. **Journal of the American Chemical Society**, [*s. l.*], v. 36, n. 7, p. 1344–1363, jul. 1914. Available at: https://pubs.acs.org/doi-/pdf/10.1021/ja02184a002. Access in: 25 jul. 2018.

BRIDGMAN, P. W. The compression of 39 substances to 100.000 kg/cm2. **American Academy of Sciences**, [*s. l.*], v. 76, p.55−70, mar. 1948. Available at: https://www.degruyter.com/document/doi/10.4159/harvard.9780674287-839.c39/html. Access in: 31 jul. 2019.

BROWN, A.; RUNDQVIST, S. Refinement of the crystal structure of black phosphorus. **Acta Crystallographica**, [*s. l.*], v. 19, n. 4, p. 684–685, 1965. Available at: https://journals.iucr.org/paper?pii=S0365110X65004140. Access in: 15 mar. 2018.

BURDETT, J. K.; LEE, S. The pressure-induced black phosphorus to a7 (arsenic) phase transformation: an analysis using the concept of orbital symmetry conservation. **Journal of Solid State Chemistry**, [*s. l.*], v. 44, n. 3, p. 415–424, oct. 1982. Available at: https://www.sciencedirect.com/science/article/abs/pii/00224596-82903905. Access in: 10 jun. 2019.

CAI, Y. *et al*. Highly itinerant atomic vacancies in phosphorene. **Journal of the American Chemical Society**, [*s. l.*], v. 138, n. 32, p. 10199–10206, jul. 2016. Available at: https://pubs.acs.org/doi/abs/10.1021/jacs.6b04926. Access in: 03 mar 2020.

CAI, Y. *et al.* Evolution of intrinsic vacancies and prolonged lifetimes of vacancy clusters in black phosphorene. **Nanoscale**, [*s. l.*], v. 11, n. 43, p. 20987–20995, 2019. Available at: https://pubs.acs.org/doi/abs/10.1021/jacs.6b04926. Access in: 03 mar 2020.

CAI, Z. *et al.* Chemical vapor deposition growth and applications of two-dimensional materials and their heterostructures. **Chemical reviews**, [*s. l.*], v. 118, n. 13, p. 6091–6133, 2018. Available at: https://pubs.acs.org/doi/abs/10.1021/acs.chem-rev.7b00536. Access in: 10 fev. 2019.

ÇAKIR, D.; SEVIK, C.; PEETRS, F. M. Significant effect of stacking on the electronic and optical properties of few-layer black phosphorus. **Physical Review B**, [*s. l.*], v. 92, n. 16, p. 165406, 2015. Available at: https://journals.aps.org/prb/abstract/-10.1103/PhysRevB.92.16-5406. Access in: 3 mar. 2020.

CAO, Y. *et al.* Quality heterostructures from two-dimensional crystals unstable in air by their assembly in inert atmosphere. **Nano letters**, [*s. l.*], v. 15, n. 8, p. 4914–4921, jul. 2015. Available at: https://pubs.acs.org/doi/abs/10.1021/acs.nanolett.5b00648. Access in: 6 fev. 2019.

CARTZ, L. *et al.* Effect of pressure on bonding in black phosphorus. **The Journal of Chemical Physics**, [*s. l.*], v. 71, n. 4, p. 1718–1721, aug. 1979. Available at: https://pubs.aip.org/aip/jcp/article-abstract/71/4/1718/463653/Effect-of-pressure-on-bonding-in-black-phosphorus?redirectedFrom=fulltext. Access in: 6 fev. 2019.

CARVALHO, A.; RODIN, A. S.; CASTRO NETO, A. H. Phosphorene nanoribbons. **Europhysics Letters**, [*s. l.*], v. 108, n. 4, p. 47005, nov. 2014. Available at: https://iopscience.iop.org/article/10.1209/0295-5075/108/47005/meta. Access in: 23 ago 2020.

CARVALHO, A. *et al.* Phosphorene: from theory to applications. **Nature Reviews Materials**, [*s. l.*], v. 1, n. 11, p. 1–16, aug. 2016. Available at: https://www.natu-re.com/articles/natrevmats201661. Access in: 22 jan. 2019.

CASTELLANOS-GOMEZ, A. Black phosphorus: narrow gap, wide applications. **The journal of physical chemistry letters**, [*s. l.*], v. 6, n. 21, p. 4280–4291, act. 2015. Available at: https://pubs.acs.org/doi/abs/10.1021/acs.jpclett.5b01686. Access in: 22 jan. 2019.

CASTELLANOS-GOMEZ, A. *et al*. Isolation and characterization of few-layer black phosphorus. **2D Materials**, [*s. l.*], v. 1, n. 2, p. 025001, jun. 2014. Available at: https://iopscience.iop.org/article/10.1088/2053-1583/1/2/025001/meta. Access in: 22 jan. 2019.

CASTRO, E. V. *et al.* Electronic properties of a biased graphene bilayer. **Journal of Physics**: condensed matter, [*s. l.*], v. 22, n. 17, p. 175503, 2010. Available at: https://iopscience.iop.org/article/10.1088/0953-8984/22/17/175503/meta. Access in: 30 jun. 2019.

CHANG, H. - M. *et al*. Germanium-doped metallic ohmic contacts in black phosphorus field-effect transistors with ultra-low contact resistance. **Scientific reports**, London, v. 7, n. 1, p. 16857, 2017. Available at: https://www.nature.com/articles/s41598-017-16845-w. Access in: 18 abr. 2021.

CHAUDHARY, V. *et al.* Phosphorene—an emerging two-dimensional material: recent advances in synthesis, functionalization, and applications. **2D Materials**, [s.l.], v. 9, n. 3, p. 032001, may 2022 Available at: https://iopscience.iop.org/article/10.1088/2053-1583/-ac6dc2/meta. Access in:19 jul. 2022.

CHAVES, A. *et al.* Signatures of subband excitons in few-layer black phosphorus. **Physical Review B**, [*s. l.*], v. 103, n. 16, p. 165428, apr. 2021. Available at: https://journals.aps.org/prb/abstract/10.1103/PhysRevB.103.165428. Access in: 1 mar. 2022.

CHEN, A. - B.; SHER, A. **Semiconductor alloys:** physics and materials engineering. New York: Plenum Press, 1995.

CHEN, J. - J. *et al*. Magnetic moments in graphene with vacancies. **Nanoscale**, [*s. l.*], v. 6, n. 15, p. 8814–8821, 2014. Available at: https://pubs.rsc.org/en/content/articlelanding/2014/nr/c3nr06892g/unauth. Access in: 15 jul. 2018.

CHEN, S. *et al*. Electron optics with pn junctions in ballistic graphene. **Science**, [*s. l.*], v. 353, n. 6307, p. 1522–1525, sep. 2016. Available at: https://www.science.org/doi/abs/10.1126/science.aaf5481. Access in: 15 jul. 2018.

CHICO, L. *et al*. Electron transmission through graphene bilayer flakes. **Acta Physica Polonica A**, [*s. l.*], v. 122, n. 2, 2012. Available at: http://przyrbwn.icm.edu.pl/APP/PDF/122/a122z2p12.pdf. Access in: 3 mar. 2020.

CHO, G. Y.; MOON, E. G. Novel quantum criticality in two-dimensional topological phase transitions. **Scientific Reports**, [*s. l.*], v. 6, n. 1, p. 1–7, 2016. Available at: https://www.nature.com/articles/srep19198. Access in: 10 mar. 2020.

KAI-LONG, C. *et al.* Transport properties in monolayer–bilayer–monolayer graphene planar junctions. **Chinese Physics B**, *[s. l.]*, v. 26, n. 6, p. 067202, 2017. Available at: https://iopscience.iop.org/article/10.1088/1674-1056/26/6/0672-02/meta. Access in: 18 ago. 2020.

CLARK, S. M.; ZAUG, J. M. Compressibility of cubic white, orthorhombic black, rhombohedral black, and simple cubic black phosphorus. **Physical Review B**, *[s. l.]*, v. 82, n. 13, p. 134111, oct. 2010. Available at: https://iopscience.iop.org/article/10.1088/1674-1056/26/6/067202/meta. Access in: 16 set. 2021.

COSTA, D. R. D. *et al.* Valley filtering in graphene due to substrate-induced mass potential. **Journal of Physics:** Condensed Matter, *[s. l.]*, v. 29, n. 21, p. 215 502, apr. 2017. Available at: https://iopscience.iop.org/article/10.1088/1361-648X/aa6-b24/meta. Access in: 21 abr. 2019.

CUI, S. *et al.* Ultrahigh sensitivity and layer-dependent sensing performance of phosphorenebased gas sensors. **Nature communications**, London, v. 6, n. 1, p. 8632, oct. 2015. Available at: https://www.nature.com/articles/ncomms9632. Access in: 30 set. 2021.

CUNHA, S. M. *et al.* Wave-packet dynamics in multilayer phosphorene. **Physical Review B**, *[s. l.]*, v. 99, n. 23, p. 235424, jun. 2019. Available at: https://journal-s.aps.org/prb/abstract/10.1103/PhysRevB.99.235424. Access in: 12 nov. 2021.

DAI, Z. *et al.* Surface buckling of black phosphorus: determination, origin, and influence on electronic structure. **Physical Review Materials**, *[s. l.]*, v. 1, n. 7, p. 074003, dec. 2017. Available at: https://journals.aps.org/prmaterials/abstract/-10.1103/PhysRevMaterials.1.074003. Access in: 15 fev. 2020.

DANA, S.; ZARE, M.; ZAMANI, P. Charge transport in nnn and npn phosphorene junctions: the use of phosphorene pn junctions as rectifiers. **Physica E**: Low-dimensional Systems and Nanostructures, *[s. l.]*, v. 124, p. 114239, 2020. Available at: https://www.sciencedirect.com/science/article/abs/pii/S1386947719319198. Access in: 14 jul. 2022.

DAS, P. M. *et al*. Controlled sculpture of black phosphorus nanoribbons. **ACS nano**, *[s. l.]*, v. 10, n. 6, p. 5687–5695, jun. 2016. Available at: https://pubs.acs.org/doi/-abs/1-0.1021/acsnano.6b02435. Access in: 26 mar. 2020.

DAS, S. *et al.* Tunable transport gap in phosphorene. **Nano letters**, *[s. l.]*, v. 14, n. 10, p. 5733–5739, oct. 2014. Available at: https://pubs.acs.org/doi/abs/10.1021/nl50-25535. Access in: 26 mar. 2020.

DE-BASHAN, L. E.; BASHAN, Y. Recent advances in removing phosphorus from wastewater and its future use as fertilizer (1997–2003). **Water research**, *[s. l.]*, v. 38, n. 19, p. 4222–4246, nov. 2004. Available at: https://www.sciencedirect.com/sci-ence/-article/abs/pii/S004313540400377X. Access in: 23 jun. 2019.

DEGL'INNOCENTI, R. *et al*. Low-bias terahertz amplitude modulator based on split-ring resonators and graphene. **ACS Nano**, *[s. l.]*, v. 8, n. 3, p. 2548–2554, 2014. Available at: https://pubs.acs.org/doi/abs/10.1021/nn406136c. Access in: 13 jul. 2019.

DIRETZIS, I. *et al*. Role of basis sets on the unfolding of supercell band structures: From tight-binding to density functional theory. **Europhysics Letters**, *[s. l.]*, v. 107, n. 2, p. 27006, apr. 2014. Available at: https://iopscience.iop.org/article/10.12-09/02955075/107/27006/meta. Access in: 21 jul. 2021.

DOGANOV, R. *et al.* Transport properties of ultrathin black phosphorus on hexagonal boron nitride. **Applied Physics Letters**, *[s. l.]*, v. 106, n. 8, p. 083505, feb. 2015. Available at: https://pubs.aip.org/aip/apl/article-abstract/106/8/083505/107-8208/Transport-properties-of-ultrathin-black-phosphorus?redirectedFrom=fulltext. Access in: 14 abr. 2022.

DOLUI, K.; QUEK, S. Y. Quantum-confinement and structural anisotropy result in electrically-tunable dirac cone in few-layer black phosphorous. **Scientific reports**, London, v. 5, n. 1, p. 11699, jul. 2015. Available at: https://www.nature.com/articles/sre-p11699. Access in: 21 jan. 2018.

EHLEN, N. *et al*. Direct observation of a surface resonance state and surface band inversion control in black phosphorus. **Physical Review B**, *[s. l.]*, v. 97, n. 4, p. 045143, jan. 2018. Available at: https://journals.aps.org/prb/abstract/10.1103/PhysRevB.-97.045143. Access in: 19 set. 2020.

EL-BARBARY, A. A. *et al*. Structure and energetics of the vacancy in graphite. **Physical Review B**, *[s. l.]*, v. 68, n. 14, p. 144107, oct. 2003. Available at: https://journals.aps.org/prb/abstract/10.1103/PhysRevB.68.144107. Access in: 23 ago. 2019.

EMSLEY, J.; HUXTABLE, J. R. **The shocking history of phosphorus:** a biography of the devil's element. London: Macmillan London, 2000.

ESQUINAZI, P. *et al*. Induced magnetic ordering by proton irradiation in graphite. **Physical Review Letters**, *[s. l.]*, v. 91, n. 22, p. 227201, nov. 2003. Available at: https://journals.aps.org/prl/abstract/10.1103/PhysRevLett.91.227201. Access in: 1 jul. 2018.

FANG, H. *et al*. Electronic self-passivation of single vacancy in black phosphorus via ionization. **Physical Review Letters**, *[s. l.]*, v. 128, n. 17, p. 176801, apr. 2022. Available at: https://journals.aps.org/prl/abstract/10.1103/PhysRevLett.128.1768-01. Access in: 5 jul. 2022.

FAROOQ, M. U.; HASHMI, A.; HONG, J. Anisotropic bias dependent transport property of defective phosphorene layer. **Scientific Reports**, *[s. l.]*, v. 5, n. 1, p. 1–11, jul. 2015. Available at: https://www.nature.com/articles/srep12482. Access in: 30 jun. 2020.

FAULKNER, J. S.; STOCKS, G. M. Calculating properties with the coherent-potential approximation. **Physical Review B**, *[s. l.]*, v. 21, n. 8, p. 3222, apr. 1980. Available at: https://journals.aps.org/prb/abstract/10.1103/PhysRevB.21.3222. Access in: 31 jul. 2019.

FAVRON, A. *et al.* Photooxidation and quantum confinement effects in exfoliated black phosphorus. **Nature materials**, London, v. 14, n. 8, p. 826–832, may 2015. Available at: https://www.nature.com/articles/nmat4299. Access in: 10 jan. 2022.

FEI, R. *et al*. Topologically protected dirac cones in compressed bulk black phosphorus. **Physical Review B**, *[s. l.]*, v. 91, n. 19, p. 195319, 2015. Available at: https://journals.aps.org/prb/abstract/10.1103/PhysRevB.91.195319. Access in: 14 mai. 2019.

FEI, R.; TRAN, V.; YANG, L. Topologically protected dirac cones in compressed bulk black phosphorus. **Physical Review B**, *[s. l.]*, v. 91, n. 19, p. 195319, may 2015. Available at: https://journals.aps.org/prb/abstract/10.1103/PhysRevB.91.195319. Access in: 3 fev. 2020.

FEI, R.; YANG, L. Strain-engineering the anisotropic electrical conductance of few-layer black phosphorus. **Nano letters**, *[s. l.]*, v. 14, n. 5, p. 2884–2889, may 2014. Available at: https://pubs.acs.org/doi/abs/10.1021/nl500935z. Access in: 3 fev. 2020.

FRANCIS, P.; MAJUMDER, C.; GHAISAS, S. V. The nonchalant magnetic ordering of vacancies in graphene. **Carbon**, *[s. l.]*, v. 91, p. 358–369, sep. 2015. Available at: https://www.sciencedirect.com/science/article/abs/pii/S00086223-15004066. Access in: 10 jan 2019.

FU, G.; CHENG, F. Anisotropic transport on monolayer and multilayer phosphorene in the presence of an electric field. **Chinese Physics Letters**, *[s. l.]*, v. 36, n. 5, p. 057302, 2019. Available at: https://iopscience.iop.org/article/10.1088/0256-307-X/3-6/5/057302/meta. Access in: 12 jan. 2020.

GABERLE, J.; SHLUGER, A. L. Structure and properties of intrinsic and extrinsic defects in black phosphorus. **Nanoscale**, *[s. l.]*, v. 10, n. 41, p. 19536–19546, 2018. Available at: https://pubs.rsc.org/en/content/articlehtml/2018/nr/c8nr06640j. Access in: 26 set. 2019.

GARRITY, K. F.; CHOUDHARY, K. Database of wannier tight-binding hamiltonians using high-throughput density functional theory. **Scientific data**, London, v. 8, n. 1, p. 106, apr.

2021. Available at: https://www.nature.com/articles/s41597-021-00885-z. Access in: 3 mar. 2022.

GEIM, A. K. Graphene: status and prospects. **Science**, *[s. l.]*, v. 324, n. 5934, p. 1530–1534, jun. 2009. Available at: https://www.science.org/doi/abs/10.1126/sc-ience.1158877. Access in: 3 mar. 2022.

GONG, J. ZHOU, B.; ZHOU, B. Electronic and transport properties of zigzag-edge monolayer/bilayer phosphorene nanoribbon junctions under a perpendicular electric field. **Physics Letters A**, *[s. l.]*, v. 383, n. 35, p. 125993, dec. 2019. Available at: https://www.sci-encedirect.com/science/article/abs/pii/S0375960119308606. Access in: 5 jun. 2020.

GOSWAMI, A.; GAWANDE, M. B. Phosphorene: Current status, challenges and opportunities. **Frontiers of Chemical Science and Engineering**, *[s. l.]*, v. 13, p. 296–309, aug. 2019. Available at: https://link.springer.com/article/10.1007/s1-1705-018-1783-y. Access in: 26 set. 2019.

GROTH, C. W. *et al.* Kwant: a software package for quantum transport. **New Journal of Physics**, *[s. l.]*, v. 16, n. 6, p. 063065, jun. 2014. Available at: https://iopscience.iop.org/a-rticle/10.1088/1367-2630/16/6/063065/meta. Access in: 6 abr. 2020.

GUAN, J.; ZHU, Z.; TOMÁNEK, D. Phase coexistence and metal-insulator transition in few-layer phosphorene: a computational study. **Physical review letters**, *[s. l.]*, v. 113, n. 4, p. 046804, jul. 2014. Available at: https://journals.aps.org/prl/abstract/10.1103/PhysRevLe-tt.113.046804. Access in: 30 ago. 2018.

GUO, H. *et al*. Phosphorene nanoribbons, phosphorus nanotubes, and van der waals multilayers. **The Journal of Physical Chemistry C**, *[s. l.]*, v. 118, n. 25, p. 14051–14059, jun. 2014. Available at: https://pubs.acs.org/doi/abs/10.1021/jp-505257g. Access in: 2 jan. 2021.

GUPTA, S.; PERIASAMY, P.; NARAYANAN, B. Defect dynamics in two-dimensional black phosphorus under argon ion irradiation. **Nanoscale**, *[s. l.]*, v. 13, n. 18, p. 8575–8590, 2021. Available at: https://pubs.rsc.org/en/content/articlelanding/2021/nr/d1nr00567g/unauth. Access in: 13 jun. 2022.

HABIB, K. M. M.; LAKE, R. K. Current modulation by voltage control of the quantum phase in crossed graphene nanoribbons. **Physical Review B**, *[s. l.]*, v. 86, n. 4, p. 045418, jul. 2012. Available at: https://journals.aps.org/prb/abstract/10.1103/Ph-ysRevB.86.045418. Access in: 31 jul. 2022.

HAHN, J. R.; KANG, H. Vacancy and interstitial defects at graphite surfaces: Scanning tunneling microscopic study of the structure, electronic property, and yield for ion-induced defect creation. **Physical Review B**, *[s.l.]*, v. 60, n. 8, p. 6007, aug. 1999. Available at: https://journals.aps.org/prb/abstract/10.1103/PhysRevB.60.6-007. Access in: 15 jan. 2019.

HANLON, D. *et al*. Liquid exfoliation of solvent-stabilized few-layer black phosphorus for applications beyond electronics. **Nature communications**, London, v. 6, n. 1, p. 8563, oct. 2015. Available at: https://www.nature.com/articles/ncomms9563. Access in: 10 jan. 2019.

HARSH, R. *et al.* Identification and manipulation of defects in black phosphorus. **The Journal of Physical Chemistry Letters**, *[s. l.]*, v. 13, n. 27, p. 6276–6282, nov. 2022. Available at: https://pubs.acs.org/doi/abs/10.1021/acs.jpclett.2c01370. Access in: 20 dez. 2022.

HART, R. R.; ROBIN, M. B.; KUEBLER, N. A. 3 p orbitals, bent bonds, and the electronic spectrum of the p4 molecule. **The Journal of Chemical Physics**, *[s. l.]*, v. 42, n. 10, p. 3631–3638, may 1965. Available at: https://pubs.aip.org/aip/jcp/article-abstract/42/10/3-631/81529/3p-Orbitals-Bent-Bonds-and-the-Electronic-Spectrum. Access in: 23 fev. 2019.

HAUG, H.; KOCH, S. W. **Quantum theory of the optical and electronic properties of semiconductors**. New Jersey: World Scientific Publishing Company, 2009.

HE, G. *et al.* Tuning 2d black phosphorus: defect tailoring and surface functionalization. **Chemistry of Materials**, *[s. l.]*, v. 31, n. 24, p. 9917–9938, nov. 2019. Available at: https://pubs.acs.org/doi/abs/10.1021/acs.chemmater.9b03639. Access in: 5 jun. 2018.

HU, T.; DONG, J. Structural phase transitions of phosphorene induced by applied strains. **Physical Review B**, *[s. l.]*, v. 92, n. 6, p. 064114, aug. 2015. Available at: https://journal-s.aps.org/prb/abstract/10.1103/PhysRevB.92.064114. Access in: 5 jun. 2018 9.

HU, W.; YANG, J. Defects in phosphorene. **The Journal of Physical Chemistry C**, *[s. l.]*, v. 119, n. 35, p. 20474–20480, 2015. Available at: https://pubs.acs.org/doi/-abs/10.1021/acs.j-pcc.5b06077. Access in: 23 fev. 2019.

HU, W. *et al*. Highly efficient photocatalytic water splitting over edge-modified phosphorene nanoribbons. **Journal of the American Chemical Society**, *[s. l.]*, v. 139, n. 43, p. 15429–15436, nov. 2017. Available at: https://pubs.acs.org/doi/abs/10.1021/jacs.7b08474. Access in: 8 mai. 2021.

HU, Z. X.; DING, W. Edge states at the interface between monolayer and bilayer graphene. **Physics Letters A**, *[s. l.]*, v. 376, n. 4, p. 610–615, 2012. Available at: https://www.sci-encedirect.com/science/article/abs/pii/S0375960111014319. Access in: 14 fev 2020.

HUANG, B.-L.; CHUU, C.-P.; LIN, M.-F. Asymmetry-enriched electronic and optical properties of bilayer graphene. **Scientific Reports**, *[s. l.]*, v. 9, n. 1, p. 1–12, 2019. Available at: https://www.nature.com/articles/s41598-018-37058-9. Access in: 14 fev 2020.

HUANG, H. *et al*. A general group theoretical method to unfold band structures and its application. **New Journal of Physics**, *[s. l.]*, v. 16, n. 3, p. 033034, mar. 2014. Available at: https://iopscience.iop.org/article/10.1088/1367-2630/16/3/033034/meta. Access in: 23 set. 2019.

HUANG, J. *et al*. Defect-induced different band alignment and transport of all-phosphorene devices from first principles. **ACS Applied Electronic Materials**, *[s. l.]*, v. 4, n. 4, p. 2070–2076, 2022. Available at: https://pubs.acs.org/doi/abs/10.1021/ac-saelm.2c00212. Access in: 8 mai. 2021.

MATHWORKS, Inc. “**Statistics and Machine Learning Toolbox Documentation**”. Massachusetts, 2022. Available at: https://www.mathworks.com/help/stats/index.ht-ml. Access in: 20 jun. 2023.

ISOBE, H. *et al*. Emergent non-fermi-liquid at the quantum critical point of a topological phase transition in two dimensions. **Physical review letters**, *[s. l.]*, v. 116, n. 7, p. 076803, feb. 2016. Available at: https://journals.aps.org/prl/abstract/10.-1103/PhysRevLett.116.0-76803. Access in: 2 jan. 2019.

JAIN, A.; MCGAUGHEY, A. J. H. Strongly anisotropic in-plane thermal transport in single-layer black phosphorene. **Scientific Reports**, *[s. l.]*, v. 5, n. 1, p. 1–5, feb. 2015. Available at: https://www.nature.com/articles/srep08501. Access in: 7 out. 2021.

JAMAATI, M.; NAMIRANIAN, A. Role of interlayer spacing in electrical transport of bilayer graphene nanoribbon: Perpendicular and armchair direction. **Superlattices and Microstructures**, *[s. l.]*, v. 101, p. 354–361, jan. 2017. Available at: https://www.scien-cedirect.com/science/article/abs/pii/S0749603616304190. Access in: Access in: 2 jan. 2020.

JASKÓLSKI, W. *et al*. Controlling the layer localization of gapless states in bilayer graphene with a gate voltage. **2D Materials**, *[s. l.]*, v. 5, n. 2, p. 025006, jan. 2018. Available at: https://iopscience.iop.org/article/10.1088/2053-1583/aaa490/meta. Access in: 2 jan. 2020.

JIANG, J. *et al*. Defect engineering in 2d materials: precise manipulation and improved functionalities. **Research**, *[s. l.]*, v. 2019, p. 1-14, jan. 2019. Available at: https://spj.scienc-e.org/doi/full/10.34133/2019/4641739. Access in: 2 jan. 2020.

JING, J. W.; PARK, H. S. Negative poisson’s ratio in single-layer black phosphorus. **Nature Communications**, London, v. 5, n. 4727, p. 1-7, aug. 2014. Available at: https://www.na-ture.com/articles/ncomms5727. Access in: 31 jul. 2019.

PEREIRA JÚNIOR, J. M.; KATSNELSON, M. L. Landau levels of single-layer and bilayer phosphorene. **Physical Review B**, *[s. l.]*, v. 92, n. 7, p. 075437, aug. 2015. Available at: https://journals.aps.org/prb/abstract/10.1103/PhysRevB.92.075437. Access in: 7 out. 2021.

JU, L. *et al*. Topological valley transport at bilayer graphene domain walls. **Nature**, *[s. l.]*, v. 520, n. 7549, p. 650–655, apr. 2015. Available at: https://www.nature.com/articles/nature-14364. Access in: 7 out. 2021.

KANG, J. **et al**. Solvent exfoliation of electronic-grade, two-dimensional black phosphorus. **ACS nano**, *[s. l.]*, v. 9, n. 4, p. 3596–3604, mar. 2015. Available at: https://pubs.acs.org/do-i/abs/10.1021/acsnano.5b01143. Access in: 17 jul. 2019.

KEYES, R. W. The electrical properties of black phosphorus. **Physical Review**, *[s. l.]*, v. 92, n. 3, p. 580, nov. 1953. Available at: https://journals.aps.org/pr/abstract/-10.1103/PhysRev.9-2.580. Access in: 17 jul. 2019.

KIKEGAWA, T.; IWASAKI, H. An x-ray diffraction study of lattice compression and phase transition of crystalline phosphorus. **Acta Crystallographica Section B:** Structural Science,

[s. l.], v. 39, n. 2, p. 158–164, 1983. Available at: https://jour-nals.iucr.org/paperbuy=yes&c-nor=a22093&showscheme=yes&sing=yes. Access in: 22 mar. 2018.

KIM, J. *et al*. Observation of tunable band gap and anisotropic dirac semimetal state in black phosphorus. **Science**, *[s. l.]*, v. 349, n. 6249, p. 723–726, aug. 2015. Available at: https://ww-w.science.org/doi/abs/10.1126/science.aaa6486. Access in: 18 abr. 2020.

KIM, J. *et al*. Two-dimensional dirac fermions protected by space-time inversion symmetry in black phosphorus. **Physical review letters**, *[s. l.]*, v. 119, n. 22, p. 226801, 2017. Available at: https://journals.aps.org/prl/abstract/10.1103/PhysRevLett.119.226801. Access in: 19 mar. 2020.

KIM, J. S. *et al*. Toward air-stable multilayer phosphorene thin-films and transistors. **Scientific reports**, London, v. 5, n. 1, p. 8989, mar. 2015. Available at: https://www.nat-ure.com/articles/srep08989. Access in: 26 mar. 2020.

KIRALY, B. *et al*. Probing single vacancies in black phosphorus at the atomic level. **Nano letters**, *[s. l.]*, v. 17, n. 6, p. 3607–3612, mar. 2017. Available at: https://pubs.acs.org/doi/fu-ll/10.1021/acs.nanolett.7b00766. Access in: 30 abr. 2019.

KISHIMOTO, K.; OKADA, S. Electron-state tuning of multilayer graphene by defects. **Japanese journal of applied physics**, *[s. l.]*, v. 55, n. 6S1, p. 06GF06, may 2016. Available at: https://iopscience.iop.org/article/10.7567/JJAP.55.06GF06/meta. Access in: 25 jun. 2020.

KISTANOV, A. A. *et al*. The role of h2o and o2 molecules and phosphorus vacancies in the structure instability of phosphorene. **2D Materials**, *[s. l.]*, v. 4, n. 1, p. 015010, nov. 2016. Available at: https://iopscience.iop.org/article/10.1088/20531583/4/1/015010/meta. Access in: 02 nov. 2021.

KÖPF, M. *et al*. Access and in situ growth of phosphorene-precursor black phosphorus. **Journal of crystal growth**, *[s. l.]*, v. 405, p. 6–10, nov. 2014. Available at: https://www.sci-encedirect.com/science/article/abs/pii/S0022024814005314. Access in: 25 jun. 2020.

KOSHINO, M.; NAKANISHI, T.; ANDO, T. Interface landau levels in graphene monolayer-bilayer junctions. **Physical Review B**, *[s. l.]*, v. 82, n. 20, p. 205436, nov. 2010. Available at: https://journals.aps.org/prb/abstract/10.1103/PhysRevB.82.205436. Access in: 5 mai. 2020.

KOTAKOSKI, J. *et al*. From point defects in graphene to two-dimensional amorphous carbon. **Physical Review Letters**, *[s. l.]*, v. 106, n. 10, p. 105505, mar. 2011. Available at: https://journals.aps.org/prl/abstract/10.1103/PhysRevLett.106.105505. Access in: 30 abr. 2019.

KOU, L.; CHEN, C.; SMITH, S. C. Phosphorene: fabrication, properties, and applications. **The Journal of Physical Chemistry Letters**, *[s. l.]*, v. 6, n. 14, p. 2794–2805, jun. 2015. Available at: https://pubs.acs.org/doi/abs/10.1021/acs.jpclett.5b01094. Access in: 3 jun. 2020.

KRIPALANI, D. *et al.* Metastable interlayer frenkel pair defects in black phosphorus. **Physical Review B**, *[s. l.]*, v. 100, n. 22, p. 224107, dec. 2019. Available at: https://journa-ls.aps.org/prb/abstract/10.1103/PhysRevB.100.224107. Access in: 30 jul. 2019.

KU, W.; BERLIJN, T.; LEE, C.-C. Unfolding first-principles band structures. **Physical review letters**, *[s. l.]*, v. 104, n. 21, p. 216401, may 2010. Available at: https://journals.aps.org/prl/abstract/10.1103/PhysRevLett.104.216401. Access in: 31 jul. 2019.

KUMAR, P. *et al*. Thickness and electric-field-dependent polarizability and dielectric constant in phosphorene. **Physical Review B**, *[s. l.]*, v. 93, n. 19, p. 195428, may 2016. Available at: https://journals.aps.org/prb/abstract/10.1103/PhysRevB.93.195428. Access in: 02 nov. 2021.

KUNDU, S.; NAIK, M. H.; JAIN, M. Native point defects in mono and bilayer phosphorene. **Physical Review Materials**, *[s. l.]*, v. 4, n. 5, p. 054004, may 2020. Available at: https://journals.aps.org/prmaterials/abstract/10.1103/PhysRevMaterials.4.054004. Access in: 31 jul. 2019.

LANE, T. L. M. *et al*. Ballistic electron channels including weakly protected topological states in delaminated bilayer graphene. **Physical Review B**, *[s. l.]*, v. 97, n. 4, p. 045301, jan. 2018. Available at: https://journals.aps.org/prb/abstract/10.1103/PhysRevB.97.045301. Access in: 31 jul. 2019.

LANGE, S.; SCHMIDT, P.; NILGES, T. Au3snp7@ black phosphorus: an easy access to black phosphorus. **Inorganic chemistry**, *[s. l.]*, v. 46, n. 10, p. 4028–4035, apr. 2007. Available at: https://pubs.acs.org/doi/abs/10.1021/ic062192q. Access in: 25 jun. 2020.

LEE, G. D. *et al*. Diffusion, coalescence, and reconstruction of vacancy defects in graphene layers. **Physical review letters**, *[s. l.]*, v. 95, n. 20, p. 205501, nov. 2005. Available at: https://journals.aps.org/prl/abstract/10.1103/PhysRevLett.95.205501. Access in: 02 nov. 2021.

LEE, G. H.; PARK, G.-H.; LEE, H.-J. Observation of negative refraction of dirac fermions in graphene. **Nature Physics**, *[s. l.]*, v. 11, n. 11, p. 925–929, sep. 2015. Available at: https://www.nature.com/articles/nphys3460. Access in: 5 mai. 2020.

LEE, S. *et al*. Anisotropic in-plane thermal conductivity of black phosphorus nanoribbons at temperatures higher than 100 k. **Nature communications**, *[s. l.]*, v. 6, n. 1, p. 1–7, oct. 2015. Available at: https://www.nature.com/articles/ncomms9573. Access in: 30 abr. 2019.

LEI, W. *et al.* Black phosphorus nanostructures: recent advances in hybridization, doping and functionalization. **Chemical Society Reviews**, *[s. l.]*, v. 46, n. 12, p. 3492–3509, apr. 2017. Available at: https://pubs.rsc.org/en/content/articlelanding/2009/cs/c7cs00021a/unauth. Access in: 6 mar. 2019.

LI, B. *et al*. Black phosphorus, a rising star 2d nanomaterial in the post-graphene era: synthesis, properties, modifications, and photocatalysis applications. **Small**, *[s. l.]*, v. 15, n. 8, p. 1804565, jan. 2019. Available at: https://onlinelibrary.wiley.com/doi/abs/10.1002/smll.201804565. Access in: 15 jul. 2019.

LI, H. *et al*. Fabrication of single-and multilayer mos2 film-based field-effect transistors for sensing no at room temperature. **Small**, *[s. l.]*, v. 8, n. 1, p. 63–67, oct. 2012. Available at: https://onlinelibrary.wiley.com/doi/abs/10.1002/smll.201101016. Access in: 02 nov. 2021.

LI, L. *et al*. Black phosphorus field-effect transistors. **Nature nanotechnology**, London, v. 9, n. 5, p. 372–377, mar. 2014. Available at: https://www.nature.com/articles/nnano.2014.35. Access in: 15 jul. 2019.

LI, L. L. *et al*. Electric-and magnetic-field dependence of the electronic and optical properties of phosphorene quantum dots. **Nanotechnology**, *[s. l.]*, v. 28, n. 8, p. 085702, jan. 2017. Available at: https://iopscience.iop.org/article/10.1088/1361-6528/aa55e8/meta. Access in: 15 jul. 2019.

LI, L. L. *et al.* Electronic properties of bilayer phosphorene quantum dots in the presence of perpendicular electric and magnetic fields. **Physical Review B**, *[s. l.]*, v. 96, n. 15, p. 155425, sep. 2017. Available at: https://journals.aps.org/prb/abstract/10.1103/PhysRevB.96.155425. Access in: 15 jul. 2019.

LI, L. L.; PEETERS, F. M. Quantum transport in defective phosphorene nanoribbons: Effects of atomic vacancies. **Physical Review B**, *[s. l.]*, v. 97, n. 7, p. 075414, feb. 2018. Available at: https://journals.aps.org/prb/abstract/10.1103/PhysRevB.97.075414. Access in: 25 jun. 2020.

LI, P. *et al*. Impurity properties in phosphorene: First-principles calculations and comparisons. **Materials Science in Semiconductor Processing**, *[s. l.]*, v. 151, p. 107006, nov. 2022. Available at: https://www.sciencedirect.com/science/article/abs/pii/S13698001-22005364. Access in: 15 jul. 2019.

LI, X. *et al*. Tunable anisotropic behaviors in phosphorene under periodic potentials in arbitrary directions. **Nanotechnology**, *[s. l.]*, v. 31, n. 10, p. 105205, nov. 2019. Available at: https://iopscience.iop.org/article/10.1088/1361-6528/ab5b51/meta. Access in: 5 mai. 2020.

LI, X.-B. *et al*. Structures, stabilities and electronic properties of defects in monolayer black phosphorus. **Scientific reports**, *[s. l.]*, v. 5, n. 1, p. 1–11, jun. 2015. Available at: https://w-ww.nature.com/articles/srep10848. Access in: 3 aug. 2020.

LI, X. J. *et al.* Tuning the electrical and optical anisotropy of a monolayer black phosphorus magnetic superlattice. **Nanotechnology**, *[s. l.]*, v. 29, n. 17, p. 174001, nov. 2018. Available at: https://iopscience.iop.org/article/10.1088/1361-6528/aaaf0f/meta. Access in: 5 dez. 2019.

LI, Y. *et al*. Modulation of the electronic properties of ultrathin black phosphorus by strain and electrical field. **The Journal of Physical Chemistry C**, *[s. l.]*, v. 118, n. 41, p. 23970–23976, 2014. Available at: https://pubs.acs.org/doi/abs/10.1021/jp506881v. Access in: 02 nov. 2021.

LI, Z. *et al*. Generation of anisotropic massless dirac fermions and asymmetric klein tunneling in few-layer black phosphorus superlattices. **Nano Letters**, *[s. l.]*, v. 17, n. 4, p. 2280–2286, 2017. Available at: https://pubs.acs.org/doi/abs/10.1021/acs.nanolett.6b04942. Access in: 9 jul. 2019.

LIBISCH, F. *et al.* Veselago lens and klein collimator in disordered graphene. **Journal of Physics:** Condensed Matter, *[s. l.]*, v. 29, n. 11, p. 114002, feb. 2017. Available at: https://iopscience.iop.org/article/10.1088/1361-648X/aa565e/meta. Access in: 25 jun. 2020.

LIMA, W. P. *et al.* Tight-binding model in first and second quantization for band structure calculations. **Brazilian Journal of Physics**, *[s. l.]*, v. 52, n. 2, p. 1-17, 2022. Available at: https://link.springer.com/article/10.1007/s13538-021-01027-x. Access in: 10 dez. 2022.

LIN, H. F.; LIU, L.-M.; ZHAO, J. 2d lateral heterostructures of monolayer and bilayer phosphorene. **Journal of Materials Chemistry C**, *[s. l.]*, v. 5, n. 9, p. 2291–2300, 2017. Available at: https://pubs.rsc.org/en/content/articlelanding/2017/tc/c7tc00013h/unauth. Access in: 10 jan. 2020.

LINO, M. *et al.* Charging energy spectrum of black phosphorus quantum dots. **Journal of Physics D**: Applied Physics, *[s. l.]*, v. 50, n. 30, p. 305103, jul. 2017. Available at: https://iopscience.iop.org/article/10.1088/1361-6463/aa75e4/meta. Access in: 31 jul. 2019.

LIU, H. *et al.* Phosphorene: an unexplored 2d semiconductor with a high hole mobility. **ACS nano**, *[s. l.]*, v. 8, n. 4, p. 4033–4041, mar. 2014. Available at: https://pubs.acs.org/doi/abs/1-0.1021/nn501226z. Access in: 5 mai. 2020.

LIU, H. *et al.* Semiconducting black phosphorus: synthesis, transport properties and electronic applications. **Chemical Society Reviews**, *[s. l.]*, v. 44, n. 9, p. 2732–2743, 2015. Available at: https://pubs.rsc.org/en/content/articlelanding/2015/cs/c4cs00257a/unauth. Access in: 30 set. 2019.

LIU, Q. *et al*. Switching a normal insulator into a topological insulator via electric field with application to phosphorene. **Nano letters**, *[s. l.]*, v. 15, n. 2, p. 1222–1228, feb. 2015. Available at: https://pubs.acs.org/doi/abs/10.1021/nl5043769. Access in: 30 abr. 2019.

LONG, G. *et al.* Achieving ultrahigh carrier mobility in two-dimensional hole gas of black phosphorus. **Nano Letters**, *[s. l.]*, v. 16, n. 12, p. 7768–7773, nov. 2016. Available at: https://pubs.acs.org/doi/abs/10.1021/acs.nanolett.6b03951. Access in: 02 nov. 2021.

LOPEZ-BEZANILLA, A. Effect of atomic-scale defects and dopants on phosphorene electronic structure and quantum transport properties. **Physical Review B**, *[s. l.]*, v. 93, n. 3, p. 035433, jan. 2016. Available at: https://journals.aps.org/prb/abstract/10.1103/PhysRev-B.93.035433. Access in: 15 jul. 2020.

LOW, T. *et al.* Tunable optical properties of multilayer black phosphorus thin films. **Physical Review B**, *[s. l.]*, v. 90, n. 7, p. 075434, aug. 2014. Available at: https://journals.aps.org/prb/-abstract/10.1103/PhysRevB.90.075434. Access in: 15 jul. 2020.

LU, W. *et al.* Plasma-assisted fabrication of monolayer phosphorene and its raman characterization. **Nano Research**, *[s. l.]*, v. 7, p. 853–859, may 2014. Available at: https://link.springer.com/article/10.1007/s12274-014-0446-7. Access in: 5 mai. 2020.

MA, Y. *et al*. Magnetic properties of vacancies in graphene and single-walled carbon nanotubes. **New Journal of Physics**, *[s. l.]*, v. 6, n. 1, p. 68, jun. 2004. Available at: https://iopscience.iop.org/article/10.1088/1367-2630/6/1/068/meta. Access in: 19 jan. 2021.

MACIÁ, E. The role of phosphorus in chemical evolution. **Chemical Society Reviews**, *[s. l.]*, v. 34, n. 8, p. 691–701, 2005. Available at: https://pubs.rsc.org/en/content/articlelanding/2005/cs/b416855k/unauth. Access in: 23 fev. 2020.

MASPERO, R.; SWEENEY, S. J.; FLORESCU, M. Unfolding the band structure of gaasbi. **Journal of Physics:** Condensed Matter, *[s. l.]*, v. 29, n. 7, p. 075001, dec. 2016. Available at: https://iopscience.iop.org/article/10.1088/1361-648X/aa50d7/meta. Access in: 23 fev. 2020.

MCCREARY, K. M. *et al.* Effect of cluster formation on graphene mobility. **Physical Review B**, *[s. l.]*, v. 81, n. 11, p. 115453, mar. 2010. Available at: https://journals.aps.org/prb/abstract/10.1103/PhysRevB.81.115453. Access in: 30 abr. 2019.

MEDEIROS, P. *et al.* Unfolding spinor wave functions and expectation values of general operators: introducing the unfolding-density operator. **Physical Review B**, *[s. l.]*, v. 91, n. 4, p. 041116, jan. 2015. Available at: https://journals.aps.org/prb/abstract/10.1103/PhysRevB.91.041116. Access in: 22 abr. 2022.

MEDEIROS, P. V. C.; STAFSTRÖM, S. BJÖRK, J. Effects of extrinsic and intrinsic perturbations on the electronic structure of graphene: retaining an effective primitive cell band structure by band unfolding. **Physical Review B**, *[s. l.]*, v. 89, n. 4, p. 041407, jan. 2014. Available at: https://journals.aps.org/prb/abstract/10.1103/PhysRevB.89.041407. Access in: 25 jun. 2020.

MELO, H. *et al.* Conditions for the occurrence of coulomb blockade in phosphorene quantum dots at room temperature. **Physical Review B**, *[s. l.]*, v. 98, n. 11, p. 115438, sep. 2018. Available at: https://journals.aps.org/prb/abstract/10.1103/PhysRevB.98.115438. Access in: 02 nov. 2021.

MIAO, J. *et al*. Ultrashort channel length black phosphorus field-effect transistors. **ACS nano**, *[s. l.]*, v. 9, n. 9, p. 9236–9243, aug. 2015. Available at: https://pubs.acs.org/doi/abs/10.1021/acsnano.5b04036. Access in: 3 mai. 2018.

MILOVANOVIC, S. P.; MOLDOVAN, D.; PEETERS, F. M. Veselago lensing in graphene with a pn junction: classical versus quantum effects. **Journal of Applied Physics**, *[s. l.]*, v. 118, n. 15, p. 154308, oct. 2015. Available at: https://pubs.aip.org/aip/jap/article-abstract/118/15/154308/140319/Veselago-lensing-in-graphene-with-a-p-n-junction?redirectedFrom=fulltext. Access in: 17 fev. 2023.

MIRANDA, L. P. *et al.* Vacancy clustering effect on the electronic and transport properties of bilayer graphene nanoribbons. **Nanotechnology**, *[s. l.]*, v. 34, n. 5, p. 1- 11, 2022. Available at: https://iopscience.iop.org/article/10.1088/1361-6528/ac9f50/meta. Access in: 10 jan. 2019.

MIRZAKHANI, M. *et al.* Landau levels in biased graphene structures with monolayer-bilayer interfaces. **Physical Review B**, *[s. l.]*, v. 96, n. 12, p. 125430, sep. 2017. Available at: https://journals.aps.org/prb/abstract/10.1103/PhysRevB.96.125430. Access in: 11 jan. 2019.

MIRZAKHANI, M.; ZARENIA, M.; PEETERS, F. M. Edge states in gated bilayer-monolayer graphene ribbons and bilayer domain walls. **Journal of Applied Physics**, *[s. l.]*, v. 123, n. 20, p. 204301, may 2018. Available at: https://pubs.aip.org/aip/jap/articleabstract/-

123/20/204301/155692/Edge-states-in-gated-bilayer-monolayer-graphene?redirectedFrom=fulltext. Access in: 15 jul. 2020.

MIRZAKHANI, M. *et al.* Electronic mach-zehnder interference in a bipolar hybrid monolayer-bilayer graphene junction. **Carbon**, *[s. l.]*, v. 201, p. 734-744, jan. 2023. Available at: https://www.sciencedirect.com/science/article/abs/pii/S0008622322007825. Access in: 15 jul. 2020.

MITTAL, V. **Encapsulation nanotechnologies**. Nova Jersey: John Wiley & Sons, 2013.

MOLDOVAN, D.; ANDELKOVIC, M.; PEETERS, F. Pybinding v0. 9.5: a python package for tight-binding calculations. **Zenodo**, *[s. l.]*, v. 826942, 2017. Available at: https://docs.pybinding.site/en/stable/. Access in: 29 ago. 2019.

NA, J. *et al.* Few-layer black phosphorus field-effect transistors with reduced current fluctuation. **ACS nano**, *[s. l.]*, v. 8, n. 11, p. 11753–11762, nov. 2014. Available at: https://pubs.acs.org/doi/abs/10.1021/nn5052376. Access in: 5 mai. 2020.

NAKAHARAI, S. *et al.* Conduction tuning of graphene based on defect-induced localization. ACS Nano, *[s. l.]*, v. 7, n. 7, p. 5694–5700, jul. 2013. Available at: https://pubs.acs.org/doi/abs/10.1021/nn401992q. Access in: 29 ago. 2019.

NAKANISHI, T.; KOSHINO, M.; ANDO, T. Transmission through a boundary between monolayer and bilayer graphene. **Physical Review B**, *[s. l.]*, v. 82, n. 12, p. 125428, sep. 2010. Available at: https://journals.aps.org/prb/abstract/10.1103/PhysRevB.82.125428. Access in: 29 ago. 2019.

NAKANISHI, T.; KOSHINO, M.; ANDO, T. Role of evanescent wave in valley polarization through junction of mono-and bi-layer graphenes. **Journal of Physics:** conference series, *[s. l.]*, v. 302, n. 1, p. 26-28, jan. 2011. Available at: https://iopscience.iop.org/article/10.1088/1742-6596/302/1/012021/meta. Access in: 29 ago. 2019.

NAKHMEDOV, E. *et al.* Vacancy mediated magnetization and healing of a graphene monolayer. **Physical Review B**, *[s. l.]*, v. 99, n. 12, p. 125125, mar. 2019. Available at: https://journals.aps.org/prb/abstract/10.1103/PhysRevB.99.125125. Access in: 29 ago. 2019.

NILGES, T.; KERSTING, M.; PFEIFER, T. A fast low-pressure transport route to large black phosphorus single crystals. **Journal of solid state chemistry**, *[s. l.]*, v. 181, n. 8, p. 1707–1711, aug. 2008. Available at: https://www.sciencedirect.com/science/article/abs/pii/S0022459608001394. Access in: 4 nov. 2021.

NISHI, H.; MATSUSHITA, Y.; OSHIYAMA, A. Band-unfolding approach to moiré-induced band-gap opening and fermi level velocity reduction in twisted bilayer graphene. **Physical Review B**, *[s. l.]*, v. 95, n. 8, p. 085420, feb. 2017. Available at: https://journals.aps.org/prb/abstract/10.1103/PhysRevB.95.085420. Access in: 31 jul. 2019.

NITSCHKE, J. R. The two faces of phosphorus. **Nature Chemistry**, London, v. 3, n. 1, p. 90–90, 2011. Available at: https://www.nature.com/articles/nchem.944. Access in: 30 jul. 2019.

NOURBAKHSH, Z.; ASGARI, R. Excitons and optical spectra of phosphorene nanoribbons. **Physical Review B**, *[s. l.]*, v. 94, n. 3, p. 035437, jul. 2016. Available at: https://journals.aps.org/prb/abstract/10.1103/PhysRevB.94.035437. Access in: 4 nov. 2021.

NOVOSELOV, K. *et al.* Two-dimensional atomic crystals. Proceedings of the **National Academy of Sciences**, *[s. l.]*, v. 102, n. 30, p. 10451–10453, jul. 2005. Available at: https://www.pnas.org/doi/abs/10.1073/pnas.0502848102. Access in: 12 abr. 2019.

NOVOSELOV, K. S. *et al*. Room-temperature electric field effect and carrier-type inversion in graphene films. **Nature**, *[s. l.]*, 2004. Available at: https://arxiv.org/abs/cond-mat/04106-31. Access in: 12 abr. 2019.

OHTA, T. *et al.* Controlling the electronic structure of bilayer graphene. **Science**, *[s. l.]*, v. 313, n. 5789, p. 951–954, aug. 2006. Available at: https://www.science.org/doi/abs/10.1126/science.1130681. Access in: 5 mai. 2020.

OVDAT, O.; DON, Y.; AKKERMANS, E. Vacancies in graphene: dirac physics and fractional vacuum charges. **Physical Review B**, *[s. l.]*, v. 102, n. 7, p. 075109, aug. 2020. Available at: https://journals.aps.org/prb/abstract/10.1103/PhysRevB.102.075109. Access in: 23 jan. 2020.

PACCHIONI, G. Cutting phosphorene nanoribbons. **Nature Reviews Materials**, London, v. 4, n. 5, p. 291–291, apr. 2019. Available at: https://www.nature.com/articles/s415780190114-3. Access in: 16 abr. 2023.

PALACIOS, J. J.; FERNÀNDEZ-ROSSIER, J.; BREY, L. Vacancy-induced magnetism in graphene and graphene ribbons. **Physical Review B**, *[s.l.]*, v. 77, n. 19, p. 195428, may 2008. Available at: https://journals.aps.org/prb/abstract/10.1103/PhysRevB.77.195428. Access in: 22 fev. 2021.

PALACIOS, J. J.; YNDURÁIN, F. Critical analysis of vacancy-induced magnetism in monolayer and bilayer graphene. **Physical Review B**, *[s. l.]*, v. 85, n. 24, p. 245443, jun. 2012. Available at: https://journals.aps.org/prb/abstract/10.1103/PhysRevB.77.195428. Access in: 22 fev. 2021.

PAPASIMAKIS, N. *et al*. The magnetic response of graphene split-ring metamaterials. **Light:** science & applications, *[s. l.]*, v. 2, n. 7, p. 1-4, jul. 2013. Available at: https://www.nature.com/articles/lsa201334. Access in: 16 fev. 2021.

PAULING, L.; SIMONETTA, M. Bond orbitals and bond energy in elementary phosphorus. **The Journal of Chemical Physics**, *[s. l.]*, v. 20, n. 1, p. 29–34, jan. 1952. Available at: https://pubs.aip.org/aip/jcp/article-abstract/20/1/29/202699/Bond-Orbitals-and-Bond-Energy-in-Elementary. Access in: 6 set. 2019.

PEI, J. *et al*. Producing air-stable monolayers of phosphorene and their defect engineering. **Nature communications**, London, v. 7, n. 1, p. 10450, jan. 2016. Available at: https://www.nature.com/articles/ncomms10450. Access in: 02 nov. 2021.

PEI, W. *et al.* Optimization of photocarrier dynamics and activity in phosphorene with intrinsic defects for nitrogen fixation. **Journal of Materials Chemistry A**, *[s. l.]*, v. 8, n. 39,

p. 20570–20580, sep. 2020. Available at: https://pubs.rsc.org/en/content/articlelanding/2-020/ta/d0ta08553g/unauth. Access in: 02 nov. 2021.

PERELLO, D. J. *et al.* High-performance n-type black phosphorus transistors with type control via thickness and contact-metal engineering. **Nature Communication**, *[s. l.]*, v. 6, n. 7809, jul. 2015. Available at: https://www.nature.com/articles/ncomms8809. Access in: 6 set. 2021.

POLJAK, M.; SULIGOJ, T. Immunity of electronic and transport properties of phosphorene nanoribbons to edge defects. **Nano Research**, *[s. l.]*, v. 9, p. 1723–1734, abr. 2016. Available at: https://link.springer.com/article/10.1007/s12274-016-1066-1. Access in: 30 ago. 2019.

POPESCU, V.; ZUNGER, A. Effective band structure of random alloys. **Physical review letters**, *[s. l.]*, v. 104, n. 23, p. 236403, jun. 2010. Available at: https://link.springer.com/a-rticle/10.1007/s12274-016-1066-1. Access in: 02 nov. 2021.

POPESCU, V.; ZUNGER, A. Extracting e versus k effective band structure from supercell calculations on alloys and impurities. **Physical Review B**, *[s. l.]*, v. 85, n. 8, p. 085201, 2012. Available at: https://journals.aps.org/prb/abstract/10.1103/PhysRevB.85.085201. Access in: 02 nov. 2021.

QIAO, J. *et al.* High-mobility transport anisotropy and linear dichroism in few-layer black phosphorus. **Nature communications**, London, [s.l.], v. 5, n. 1, p. 4475, jul. 2014. Available at: https://www.nature.com/articles/ncomms5475. Access in: 15 jan. 2019.

QIN, G. *et al*. Anisotropic intrinsic lattice thermal conductivity of phosphorene from first principles. **Physical Chemistry Chemical Physics**, *[s. l.]*, v. 17, n. 7, p. 4854–4858, oct. 2015. Available at: https://pubs.rsc.org/en/content/articlelanding/2015/cp/c4cp04858j/unauth. Access in: 31 jan. 2020.

REN, Y.; ZHOU, X.; ZHOU, G. Edge and sublayer degrees of freedom for phosphorene nanoribbons with twofold-degenerate edge bands via electric field. **Physical Review B**, *[s. l.]*, v. 103, n. 4, p. 045405, jan. 2021. Available at: https://journals.aps.org/prb/abstract/10.11-03/PhysRevB.103.045405. Access in: 25 jan. 2022.

REZAEI, M. *et al.* Thermoelectric properties of armchair phosphorene nanoribbons in the presence of vacancy-induced impurity band. **Nanotechnology**, *[s. l.]*, v. 32, n. 37, p. 375704, jun. 2021. Available at: https://iopscience.iop.org/article/10.1088/13616528/ac08ba/meta. Access in: 15 jan. 2023.

RIFFLE, J. V. *et al.* Impact of vacancies on electronic properties of black phosphorus probed by stm. **Journal of Applied Physics**, *[s. l.]*, v. 123, n. 4, p. 044301, jan. 2018. Available at: https://pubs.aip.org/aip/jap/article-abstract/123/4/044301/346985/Impact-of-vacancies-on-electronic-properties-of?redirectedFrom=fulltext. Access in: 31 jan. 2020.

RIJAL, B. *et al*. Charged vacancy defects in monolayer phosphorene. **Physical Review Materials**, *[s. l.]*, v. 5, n. 12, p. 124004, dec. 2021. Available at: https://journals.aps.org/pr-materials/abstract/10.1103/PhysRevMaterials.5.124004. Access in: 12 mar. 2019.

RODIN, A.; CARVALHO, A.; NETO, A. C. Strain-induced gap modification in black phosphorus. **Physical review letters**, *[s. l.]*, v. 112, n. 17, p. 176801, may 2014. Available at: https://journals.aps.org/prl/abstract/10.1103/PhysRevLett.112.176801. Access in: 12 mar. 2019.

RUDENKO, A.; YUAN, S.; KATSNELSON, M. Toward a realistic description of multilayer black phosphorus: from g w approximation to large-scale tight-binding simulations. **Physical Review B**, *[s. l.]*, v. 92, n. 8, p. 085419, aug. 2015. Available at: https://journals.aps.org/prb/abstract/10.1103/PhysRevB.92.085419. Access in: 15 jan. 2019.

RUDENKO, A. N.; KATSNELSON, M. I. Quasiparticle band structure and tight-binding model for single-and bilayer black phosphorus. **Physical Review B**, *[s. l.],* v. 89, n. 20, p. 201408, may 2014. Available at: https://journals.aps.org/prb/abstract/10.1103/PhysRevB.-89.201408. Access in: 02 nov. 2021.

RUSEKAS, J. *et al*. Electron transmission through graphene monolayer-bilayer junction: an analytical approach. **Lithuanian Journal of Physics**, *[s. l.]*, v. 52, n. 1, 2012. Available at: https://www.lmaleidykla.lt/ojs/index.php/physics/article/view/2271. Access in: 10 jul. 2019.

RYDER, C. *et al.* Covalent functionalization and passivation of exfoliated black phosphorus via aryl diazonium chemistry. **Nature chemistry**, London, v. 8, n. 6, p. 597–602, jun. 2016. Available at: https://www.nature.com/articles/nchem.2505. Access in:10 jul. 2019.

RYZHII, M.; RYZHII, V. Injection and population inversion in electrically induced p–n junction in graphene with split gates. Japanese Journal of Applied Physics, *[s. l.]*, v. 46, n. 3L, p. L151, feb. 2007. Available at: https://iopscience.iop.org/article/10.1143/JJAP.46.L1-51/meta. Access in: 2 mar. 2019.

SARKAR, S. D. *et al*. Anisotropic transport of normal metal-barrier-normal metal junctions in monolayer phosphorene. **Journal of Physics:** condensed matter, *[s. l.]*, v. 29, n. 28, p. 285601, 2017. Available at: https://iopscience.iop.org/article/10.1088/1361-648X/aa7497/meta. Access in: 30 jul. 2019.

SERVICE, R. F. Is silicon's reign nearing its end? **Science**, *[s. l.]*, v. 323, n. 5917, p. 1000–1002, feb. 2009. Available at: https://www.science.org/doi/abs/10.1126/science.323.5917.1-000. Accessed on: 28 nov. 2022.

SHAH, N. *et al.* Transport characteristics of multi-terminal pristine and defective phosphorene systems. **Nanotechnology**, *[s. l.]*, v. 30, n. 45, p. 455705, aug. 2019. Available at: https://iopscience.iop.org/article/10.1088/1361-6528/ab3961/meta. Access in: 16 abr. 2021.

SHAN, W. *et al.* Band anticrossing in gainnas alloys. **Physical Review Letters**, *[s. l.]*, v. 82, n. 6, p. 1221, feb. 1999. Available at: https://journals.aps.org/prl/abstract/10.1103/PhysRev-Lett.82.1221. Access in: 16 abr. 2021.

SHIROTANI, I. J. M. C. Growth of large single crystals of black phosphorus at high pressures and temperatures, and its electrical properties. **Molecular Crystals and Liquid Crystals**, *[s. l.]*, v. 86, n. 1, p. 203–211, 1982. Available at: https://www.tandfonline.com/-doi/abs/10.1080/00268948208073686. Access in: 16 jun. 2018.

SHRIBER, P. *et al.* First-principles investigation of black phosphorus synthesis. **The Journal of Physical Chemistry Letters**, *[s. l.]*, v. 9, n. 7, p. 1759–1764, mar. 2018. Available at: https://pubs.acs.org/doi/abs/10.1021/acs.jpclett.8b00055. Access in: 16 jun. 2018.

SHUKLA, V. *et al*. Electronic and transport properties of bilayer phosphorene nanojunction: effect of paired substitution doping. **ACS Applied Electronic Materials**, *[s. l.]*, v. 3, n. 2, p. 733–742, feb. 2021. Available at: https://pubs.acs.org/doi/full/10.1021/acsaelm.0c00897. Access in: 13 mar. 2022.

SISAKHT, E. *et al*. Strain-induced topological phase transition in phosphorene and in phosphorene nanoribbons. **Physical Review B**, *[s. l.]*, v. 94, n. 8, p. 085417, aug. 2016. Available at: https://journals.aps.org/prb/abstract/10.1103/PhysRevB.94.085417. Access in: 15 jan. 2019.

SISAKHT, E. T.; ZARE, M. H.; FAZILEH, F. Scaling laws of band gaps of phosphorene nanoribbons: A tight-binding calculation. **Physical Review B**, *[s. l.]*, v. 91, n. 8, p. 085409, feb. 2015. Available at: https://journals.aps.org/prb/abstract/10.1103/PhysRevB.91.085409. Access in: 10 jan. 2019.

SMITH, J. B.; HAGAMAN, D.; JI, H.-F. Growth of 2d black phosphorus film from chemical vapor deposition. **Nanotechnology**, *[s. l.]*, v. 27, n. 21, p. 1-8, apr. 2016. Available at: http-s://iopscience.iop.org/article/10.1088/0957-4484/27/21/215602/meta. Access in: 25 fev. 2020.

SMOTLACHA, J.; PINCAK, R. Electronic properties of phosphorene and graphene nanoribbons with edge vacancies in magnetic field. **Physics Letters A**, *[s. l.]*, v. 382, n. 12, p. 846–854, mar. 2018. Available at: https://www.sciencedirect.com/science/article/abs/pii/S-0375960118300768. Access in: 13 mar. 2019.

SORKIN, V. *et al*. Recent advances in the study of phosphorene and its nanostructures. **Critical Reviews in Solid State and Materials Sciences**, *[s. l.]*, v. 42, n. 1, p. 1–82, 2017. Available at: https://www.tandfonline.com/doi/abs/10.1080/10408436.2016.1182469. Access in: 18 mai. 2019.

SOTOR, J. *et al.* Ultrafast thulium-doped fiber laser mode locked with black phosphorus. **Optics letters**, *[s. l.]*, v. 40, n. 16, p. 3885–3888, 2015. Available at: https://opg.optica.org/-ol/abstract.cfm?uri=ol-40-16-3885. Access in: 22 abr. 2019.

SOUSA, D. D. *et al*. Boundary conditions for phosphorene nanoribbons in the continuum approach. **Physical Review B**, *[s. l.]*, v. 94, n. 23, p. 235415, dec. 2016. Available at: https://journals.aps.org/prb/abstract/10.1103/PhysRevB.94.235415. Access in: 25 jul. 2019.

SOUSA, D. J. P. de *et al*. Multilayered black phosphorus: From a tight-binding to a continuum description. **Physical Review B**, *[s. l.]*, v. 96, n. 15, p. 155427, oct. 2017. Available at: https://journals.aps.org/prb/abstract/10.1103/PhysRevB.96.155427. Access in: 25 jul. 2019.

SOUSA, J. D. *et al*. Substrate effects on the exciton fine structure of black phosphorus quantum dots. **Physical Review B**, *[s. l.]*, v. 96, n. 3, p. 035122, jul. 2017. Available

at: https://journals.aps.org/prb/abstract/10.1103/PhysRevB.96.035122. Access in: 25 jul. 2019.

SUN, L. *et al*. Electronic properties of phosphorene nanoribbons with nanoholes. **RSC advances**, *[s. l.]*, v. 8, n. 14, p. 7486–7493, feb. 2018. Available at: https://pubs.rsc.org/en/-content/articlehtml/2018/ra/c7ra12351e. Access in: 17 abr. 2022.

TAKAO, Y.; ASAHINA, H.; MORITA, A. Electronic structure of black phosphorus in tight binding approach. **Journal of the Physical Society of Japan**, Japan, v. 50, n. 10, p. 3362–3369, oct. 1981. Available at: https://www.jstage.jst.go.jp/article/jpsj1946/50/10/50_10_336-2/_article/-char/ja/. Access in: 15 jul. 2019.

TAN, S. J. *et al*. Quasi-monolayer black phosphorus with high mobility and air stability. **Advanced Materials**, *[s. l.]*, v. 30, n. 6, p. 1704619, feb. 2018. Available at: https://online-library.wiley.com/doi/abs/10.1002/adma.201704619. Access in: 10 mar. 2019.

THOMAS, S. J.; PIERZYNSKI, G. M. Chemistry of phosphorus in soils. **Chemical processes in soils**, *[s. l.]*, v. 8, p. 151–192, jan. 2005. Available at: https://acsess.onlinelib-rary.wiley.com/doi/abs/10.2136/sssabookser8.c2. Access in: 1 mai. 2018.

TORBATIAN, Z.; ASGARI, R. Optical absorption properties of few-layer phosphorene. **Physical Review B**, *[s. l.]*, v. 98, n. 20, p. 205407, nov. 2018. Available at: https://journal-s.aps.org/prb/abstract/10.1103/PhysRevB.98.205407. Access in: 1 mai. 2018.

TRAN, V. *et al*. Layer-controlled band gap and anisotropic excitons in few-layer black phosphorus. **Physical Review B**, *[s. l.]*, v. 89, n. 23, p. 235319, jun. 2014. Available at: https://journals.aps.org/prb/abstract/10.1103/PhysRevB.89.235319. Access in: 19 fev. 2019.

VASIC, B. *et al*. Tunable metamaterials based on split ring resonators and doped graphene. **Applied Physics Letters**, *[s. l.]*, v. 103, n. 1, p. 011102, 2013. Available at: https://pubs.aip.-org/aip/apl/article-abstract/103/1/011102/235965/Tunable-metamaterials-based-on-split-ring?redirectedFrom=fulltext. Access in: 19 fev. 2019.

WANG, H. *et al*. Black phosphorus radio-frequency transistors. **Nano letters**, *[s. l.]*, v. 14, n. 11, p. 6424–6429, oct. 2014. Available at: https://pubs.acs.org/doi/abs/10.1021/nl5029717. Access in: 10 mar. 2020.

WANG, K. *et al.* Graphene transistor based on tunable dirac fermion optics. **Proceedings of the National Academy of Sciences**, *[s. l.]*, v. 116, n. 14, p. 6575–6579, mar. 2019. Available at: https://www.pnas.org/doi/abs/10.1073/pnas.1816119116. Access in: 20 jun. 2020.

WANG, M. *et al*. van der waals heterostructures of germanene, stanene, and silicene with hexagonal boron nitride and their topological domain walls. **Physical Review B**, *[s. l.]*, v. 93, n. 15, p. 155412, apr. 2016. Available at: https://journals.aps.org/prb/abstract/10.1103/Phys-RevB.93.155412. Access in: 4 jan. 2020.

WANG, V.; KAWAZOE, Y.; GENG, W. T. Native point defects in few-layer phosphorene. **Physical Review B**, *[s. l.]*, v. 91, n. 4, p. 045433, jan. 2015. Available at: https://journals.ap-s.org/prb/abstract/10.1103/PhysRevB.91.045433. Access in: 3 jan. 2020.

WANG, X.; LAN, S. Optical properties of black phosphorus. **Advances in Optics and photonics**, *[s. l.]*, v. 8, n. 4, p. 618–655, 2016. Available at: https://opg.optica.org/aop/abstract.cfm?uri=aop-8-4-618. Access in: 12 fev. 2021.

WARSCHAUER, D. Electrical and optical properties of crystalline black phosphorus. **Journal of Applied Physics**, *[s. l.]*, v. 34, n. 7, p. 1853–1860, jul. 1963. Available at: https://pubs.aip.org/aip/jap/article-abstract/34/7/1853/164645/Electrical-and-OpticalProperties-of-Crystalline. Access in: 10 jul. 2019.

WATTS, M. C. *et al.* Production of phosphorene nanoribbons. **Nature**, London, v. 568, n. 7751, p. 216–220, apr. 2019. Available at: https://www.nature.com/articles/s41586-0191074-x. Access in: 30 jan. 2019.

WEI, Q.; PENG, X. Superior mechanical flexibility of phosphorene and few-layer black phosphorus. **Applied Physics Letters**, *[s. l.]*, v. 104, n. 25, p. 251915, jun. 2014. Available at: https://pubs.aip.org/aip/apl/article-abstract/104/25/251915/891676/Superior-mechanical-flexibility-of-phosphorene-and?redirectedFrom=fulltext. Access in: 31 jul. 2020.

WOOD, J. *et al*. Effective passivation of exfoliated black phosphorus transistors against ambient degradation. **Nano letters**, *[s. l.]*, v. 14, n. 12, p. 6964–6970, nov. 2014. Available at: https://pubs.acs.org/doi/abs/10.1021/nl5032293. Access in: 31 jul. 2020.

WU, Q. *et al*. Electronic and transport properties of phosphorene nanoribbons. **Physical Review B**, *[s. l.]*, v. 92, n. 3, p. 035436, jul. 2015. Available at: https://journals.aps.org/prb/abstract/10.1103/PhysRevB.92.035436. Access in: 12 jul. 2019.

WU, X. *et al*. Spin density waves predicted in zigzag puckered phosphorene, arsenene and antimonene nanoribbons. **AIP Advances**, *[s. l.]*, v. 6, n. 4, p. 045318, apr. 2016. Available at: https://pubs.aip.org/aip/adv/article/6/4/045318/22031. Access in: 22 nov. 2020.

WU, Z.; NI, Z. Spectroscopic investigation of defects in two-dimensional materials. **Nanophotonics**, *[s. l.]*, v. 6, n. 6, p. 1219–1237, mar. 2017. Available at: https://www.degruyter.com/document/doi/10.1515/nanoph-2016-0151/html. Access in: 26 jan. 2021.

WU, Z. *et al*. Large-scale growth of few-layer two-dimensional black phosphorus. **Nature materials**, London, v. 20, n. 9, p. 1203–1209, may 2021. Available at: https://www.nature.com/articles/s41563-021-01001-7. Access in: 25 fev. 2020.

XIA, F.; WANG, H.; JIA, Y. Rediscovering black phosphorus as an anisotropic layered material for optoelectronics and electronics. **Nature Communications**, *[s. l.]*, v. 5, n. 1, p. 1–6, jul. 2014. Available at: https://www.nature.com/articles/ncomms5458. Access in: 5 jan. 2019.

XIA, F. *et al.* Black phosphorus and its isoelectronic materials. **Nature Reviews Physics**, *[s. l.]*, v. 1, n. 5, p. 306–317, apr. 2019. Available at: https://www.nature.com/articles/ncomms-5458. Access in: 3 mar. 2019.

XIANG, Z. J. *et al.* Pressure-induced electronic transition in black phosphorus. **Physical review letters**, *[s. l.]*, v. 115, n. 18, p. 186403, oct. 2015. Available at: https://journals.aps.org/prl/abstract/10.1103/PhysRevLett.115.186403. Access in: 7 mar. 2019.

XU, Y. *et al.* Epitaxial nucleation and lateral growth of high-crystalline black phosphorus films on silicon. **Nature communications**, London, v. 11, n. 1, p. 1330, mar. 2020. Available at: https://www.nature.com/articles/s41467-020-14902-z. Access in: 5 fev. 2021.

YANG, G. *et al*. Room-temperature magnetism on the zigzag edges of phosphorene nanoribbons. **Physical Review B**, *[s. l.]*, v. 94, n. 7, p. 075106, aug. 2016. Available at: https://journals.aps.org/prb/abstract/10.1103/PhysRevB.94.075106. Access in: 21 fev. 2020.

YANG, S. *et al.* A delamination strategy for thinly layered defect-free high-mobility black phosphorus flakes. **Angewandte Chemie**, *[s. l.]*, v. 130, n. 17, p. 4767–4771, apr. 2018. Available at: https://onlinelibrary.wiley.com/doi/abs/10.1002/ange.201801265. Access in: 12 jul. 2019.

YANG, Y. R. *et al*. Spin-dependent seebeck effect in zigzag black phosphorene nanoribbons. **RSC advances**, *[s. l.]*, v. 6, n. 50, p. 44019–44023, 2016. Available at: https://pubs.rsc.org/en/content/articlelanding/2016/ra/c6ra04069a/unauth. Access in: 12 jul. 2019.

YAO, F. *et al*. In situ transmission electron microscopy study of the formation and migration of vacancy defects in atomically thin black phosphorus. **2D Materials**, *[s. l.]*, v. 8, n. 2, p. 025004, dec. 2020. Available at: https://iopscience.iop.org/article/10.1088/2053-1583/abce09/meta. Access in: 13 mar. 2019.

YAO, Q. *et al*. Theoretical prediction of phosphorene and nanoribbons as fast-charging li ion battery anode materials. **The Journal of Physical Chemistry C**, *[s. l.]*, v. 119, n. 12, p. 6923–6928, 2015. Available at: https://pubs.acs.org/doi/abs/10.1021/acs.jpcc.5b02130. Access in: 24 jun. 2021.

YASAEI, P. *et al*. High-quality black phosphorus atomic layers by liquid-phase exfoliation. **Advanced Materials**, *[s. l.]*, v. 27, n. 11, p. 1887–1892, feb. 2015. Available at: https://onlinelibrary.wiley.com/doi/abs/10.1002/adma.201405150. Access in: 15 jan. 2022.

YAZYEV, O. V.; HELM, L. Defect-induced magnetism in graphene. **Physical Review B**, *[s. l.]*, v. 75, n. 12, p. 125408, mar. 2007. Available at: https://journals.aps.org/prb/abstract/10.1103/PhysRevB.75.125408. Access in: 23 jan. 2022.

YIN, L. J. *et al.* Direct imaging of topological edge states at a bilayer graphene domain wall. **Nature Communications**, *[s. l.]*, v. 7, n. 1, p. 1–6, jun. 2016. Available at: https://www.nature.com/articles/ncomms11760. Access in: 20 fev. 2018.

YU, W. *et al.* Facile production of phosphorene nanoribbons towards application in lithium metal battery. **Advanced Materials**, *[s. l.]*, v. 33, n. 35, p. 2102083, jul. 2021. Available at: https://onlinelibrary.wiley.com/doi/abs/10.1002/adma.202102083. Access in: 19 nov. 2021.

YUAN, S. *et al.* Quantum hall effect and semiconductor-to-semimetal transition in biased black phosphorus. **Physical Review B**, *[s. l.],* v. 93, n. 24, p. 245433, jun. 2016. Available at: https://journals.aps.org/prb/abstract/10.1103/PhysRevB.93.245433. Access in: 23 abr. 2021.

ZANG, Y.; WANG, L. W. Global electronic structure of semiconductor alloys through direct large-scale computations for iii-v alloys ga x in 1- x p. **Physical Review B**, *[s. l.]*, v. 83, n. 16, p. 165208, apr. 2011. Available at: https://journals.aps.org/prb/abstract/10.1103/PhysRevB.83.165208. Access in: 15 mar. 2020.

ZHAN, F. *et al*. Interplay of charged states and oxygen dissociation induced by vacancies in phosphorene. **The Journal of Physical Chemistry C**, *[s. l.]*, v. 123, n. 44, p. 27080–27087, 2019. Available at: https://pubs.acs.org/doi/abs/10.1021/acs.jpcc.9b08518. Access in: 18 jun. 2021.

ZHANG, G. *et al.* Infrared fingerprints of few-layer black phosphorus. **Nature communications**, London, v. 8, n. 1, p. 14071, jan. 2017. Available at: https://www.nature.com/articles/ncomms14071. Access in: 12 jul. 2019.

ZHANG, J. *et al.* Phosphorene nanoribbon as a promising candidate for thermoelectric applications. **Scientific reports**, *[s. l.]*, v. 4, n. 1, p. 1–8, 2014. Available at: https://www.nature.com/articles/srep06452. Access in: 15 mar. 2020.

ZHANG, R.; WU, X.; YANG, J. Blockage of ultrafast and directional diffusion of li atoms on phosphorene with intrinsic defects. **Nanoscale**, *[s. l.]*, v. 8, n. 7, p. 4001–4006, 2016. Available at: https://pubs.rsc.org/en/content/articlelanding/2016/nr/c5nr06856h/unauth. Access in: 15 jun. 2021.

ZHANG, S. *et al*. Extraordinary photoluminescence and strong temperature/angle-dependent raman responses in few-layer phosphorene. ACS nano, *[s. l.]*, v. 8, n. 9, p. 9590–9596, sep. 2014. Available at: https://pubs.acs.org/doi/abs/10.1021/nn503893j. Access in: 5 jan. 2019.

ZHANG, Y. *et al.* Direct observation of a widely tunable bandgap in bilayer graphene. **Nature**, London, v. 459, n. 7248, p. 820–823, 2009. Available at: https://www.nature.com/articles/nature08105. Access in: 1 fev. 2020.

ZHU, W. *et al*. Flexible black phosphorus ambipolar transistors, circuits and AM demodulator. **Nano letters**, *[s. l.]*, v. 15, n. 3, p. 1883–1890, feb. 2015. Available at: https://pubs.acs.org/doi/abs/10.1021/nl5047329. Access in: 2 fev. 2020.

ZHU, W. *et al.* Black phosphorus flexible thin film transistors at gighertz frequencies. **Nano letters**, *[s. l.]*, v. 16, n. 4, p. 2301–2306, mar. 2016. Available at: https://pubs.acs.org/doi/abs/10.1021/nl5047329. Access in: 13 jul. 2022.